

THE AUTOMATION AND OPTIMIZATION OF THE AUTOMATED PROSTATE
POSITIONING SYSTEM

AN ABSTRACT

SUBMITTED ON THE FIFTH DAY OF MAY 2020

TO THE DEPARTMENT OF BIOMEDICAL ENGINEERING

IN PARTIAL FULFILLMENT OF THE REQUIREMENTS

OF THE SCHOOL OF SCIENCE AND ENGINEERING

OF TULANE UNIVERSITY

FOR THE DEGREE

OF

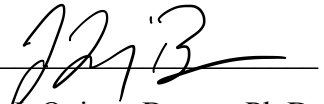
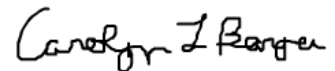
BACHELOR OF SCIENCE IN ENGINEERING & MASTER OF SCIENCE

BY



MAX SEBASTIAN COOPER

APPROVED:


J. Quincy Brown, Ph.D.

Carolyn Bayer, Ph.D.



Damir Khismatullin, Ph.D.

Abstract

Prostate cancer is the second leading cause of death due to cancer for men in the United States. A common form of treatment for prostate cancer is a surgical procedure known as a radical prostatectomy, the full resection of the prostate from the patient. The success of this procedure is quantified by the presence of diseased tissue at the surface of the resected specimen. The ideal outcome of this procedure is known as a negative surgical margin (NSM), indicating that there is no diseased tissue along the margin of the specimen, however positive surgical margins (PSM) occur regularly. Currently, the method for intra-operative detection is Frozen Section Analysis (FSA) but it suffers from a high false negative rate due to a small sampling size.

Our group is developing a new method of *ex vivo* imaging of the entire radical prostatectomy surgical margins using video-rate structured illumination microscopy (VR-SIM) paired with a custom-built sample position system. The goal of this method is to rapidly image the entire circumference of the resected specimen in order to correct surgical margins intraoperatively. Currently, the custom-built apparatus used for manipulating the specimen, known as the Automated Prostate Positioning System (APPS), faces several challenges in order for the machine to be considered adoptable in a point-of-care environment.

The goal of this work is to further refine the APPS with the intent of implementing this system for point-of-care applications. This will be achieved through three specific aims: (1) identify the existing challenges faced in clinical applications of the current APPS configuration, (2) use the challenges identified with the current configuration of the APPS to implement structural and software changes to better suit clinical applications, and (3)

verify that the new APPS configuration is an improvement of the prior iteration through bench experiments.

THE AUTOMATION AND OPTIMIZATION OF THE AUTOMATED PROSTATE
POSITIONING SYSTEM

A THESIS

SUBMITTED ON THE FIFTH DAY OF MAY 2020

TO THE DEPARTMENT OF BIOMEDICAL ENGINEERING

IN PARTIAL FULFILLMENT OF THE REQUIREMENTS

OF THE SCHOOL OF SCIENCE AND ENGINEERING

OF TULANE UNIVERSITY

FOR THE DEGREE

OF

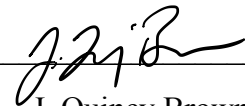
BACHELOR OF SCIENCE IN ENGINEERING & MASTER OF SCIENCE

BY

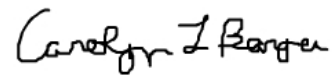


MAX SEBASTIAN COOPER

APPROVED:



J. Quincy Brown, Ph.D.



Carolyn Bayer, Ph.D.



Damir Khismatullin, Ph.D.

Acknowledgements

First and foremost, I would like to thank my advisor and personal mentor Dr. J. Quincy Brown whom without his support I would not have been able to complete this work. Thank you for continuing to push me to think outside of the box and to continue forward in the face of failure.

I would then like to express my gratitude to my colleagues in the Translational Biophotonics Laboratory whose work helped me during this process.

I would also like to thank my committee members Dr. Carolyn Bayer and Dr. Damir Khismatullin whose insight benefited this work greatly.

In addition, I would like to thank the entirety of the faculty of the Tulane Biomedical Engineering Department who foster an environment of hard work and support unlike any other.

Finally, I would like to thank my family and friends for their continued support and guidance.

Table of Contents:

Acknowledgements	ii
Table of Figures:.....	v
List of Tables:.....	x
1. Background.....	1
2. Introduction	20
3. Clinical Evaluation of the Generation 1 APPS system for automated imaging of Radical Prostatectomy specimens.	22
3.1 Introduction.....	22
3.2 Materials and Methods.....	24
3.2.1 Sample Acquisition.....	24
3.2.2 Experimental methodology.....	24
3.2.3 Sample preparation	26
3.2.4 Operation of the APPS System.....	27
3.3 Results and Discussion	31
4. Experimental Testing and Results of the Device Design of the Generation 2 APPS....	35
4.1. Introduction and Functional Requirements for Generation 2	35
4.2 Experimental Approach to Design.....	36
4.2.1. Infrared Sensor.....	36
4.2.2. Evaluation of other sensing mechanisms.....	39
4.3 The Servo Motor	39
4.4. Integration of the servo motor into the APPS.....	43
4.4 Second and Third Hardware Updates	44
4.6 Integration into LabVIEW and Pivot to MATLAB.....	49
5. Bench Validation Experiments for the APPS Generation 2	54
5.1 Experiment 1 Speed Testing of the APPS Generation 2	54
5.1.1 Materials and Methods.....	54
5.1.2 Results.....	55
5.2 Experiment 2 Ten Panel Rotation without imaging.....	57
5.2.1. Materials and Methods.....	57
5.2.2 Results.....	57
5.2.3 Discussion.....	60

5.3 Experiment 3 Test of Repeatability with Imaging.....	63
5.3.1 Materials and Methods.....	63
5.3.2 Results.....	65
5.3.3 Discussion.....	68
6. Conclusion.....	71
7. Bibliography.....	77
8. Appendix.....	81

Table of Figures:

<i>Figure 1.1:</i> Diagram of positive versus negative surgical margins [6].....	3
<i>Figure 1.2:</i> Method of prostatectomy specimen sectioning for traditional pathology [39]..	4
<i>Figure 1.3 A, B, C, D:</i> Images depicting the process of NeuroSAFE intraoperative surgical margin analysis [11,39].....	5,6
<i>Figure 1.4:</i> Block diagram of the process of Optical Coherence Tomography [29].....	8
<i>Figure 1.5:</i> Illustration of difference of light pathways in widefield microscopy versus confocal microscopy [33].....	9
<i>Figure 1.6:</i> The process of calculated SIM Frames. The light source is masked by a regular grid, which casts a pattern of stripes on the in-focus object plane. Three images of the thick object are acquired, shifting the grid by one-third repeat between each acquisition. Each image is the sum of contributions from the in-focus plane, which is shadowed by sharply defined stripes, plus blurred out-of-focus planes without distinct stripes. The square root of the sum of the squared difference images removes the out-of-focus blurred light, giving the in-focus plane [35].....	11
<i>Figure 1.7:</i> A) schematic and B) Photograph of VR-SIM system. LDI – laser engine; BE – beam expander; CL – collimator; SLM – spatial light modulator; PBS – polarizing beamsplitter; P – polarizer; L – achromat lens; F – multiband filter; DBS – multiband dichroic beamsplitter; OL – objective lens; sCMOS – camera. Figure adapted from Wang et al 2015.....	12
<i>Figure 1.8:</i> VR-SIM images and subsequent H&E slide images of prostate biopsy confirmed as malignant. (A) Wide-field (i.e., without SIM) image of the entire biopsy, (B) VR-SIM mosaic image of the entire biopsy. (C) Digital image of the corresponding H&E section. (D) VR-SIM and (E) H&E zoom images of the regions of interest marked by the correspondingly labeled boxes in B and C, depicting an area of normal skeletal muscle and fibrous stroma. (F) VR-SIM and (G) H&E zoom images of the regions of interest marked by the correspondingly labeled boxes in B and C, depicting an area of malignant glands. Figure adapted from Wang et al., 2015 [37].....	14
<i>Figure 1.9:</i> (a) The VR-SIM system is mounted on a movable cart. (b) Close-up of the VR-SIM imaging system with a prostate on the microscope stage. The imaging objective is below the prostate in an epi-illumination configuration. (c) Close-up (side view) of the posterior imaging position of the prostate. The posterior surface is contacting the slide; the imaging objective is seen below the prostate. The prostate is rotated about the urethral axis (yellow dashed line) to enable imaging of the prostate circumference. The prostate and the seminal vesicles/ductus deferens are indicated in the photograph. (d–g) Top views of the circumferential imaging positions (posterior, left lateral, anterior, right lateral). A wooden dowel rod is inserted through the urethra to demonstrate the rotation axis between imaging positions. In (d), the plane between the prostate and the attached seminal vesicles (s.v.) and	

ductus deferens (d.d.) is indicated by a dashed yellow line. Figure adapted from Wang et al., 2016..... 15

Equation 1: An equation representing the surface area of a compressed sphere, r represents the radius of the prostate, c represents the degree to which the sphere is compressed, usually denoted by a percentage. Equation adapted from Luethy et al. [38]..... 16

Figure 1.10: A side-by-side comparison of the original method of manual rotation versus the new method of automated rotation.....17

Figure 1.11: Open-top light-sheet microscope for clinical pathology developed by Liu et al. **a**, An illumination light sheet enters the bottom surface of a tissue sample at an oblique 45-deg angle (purple). The specimen(s) is placed on a modular glass-plate sample holder, which is inserted into a two-axis translation stage and scanned in a serpentine pattern of volumetric image strips to enable 3D imaging over a large lateral extent. Fluorescence emission (cyan), which is generated along the light sheet, is collected in the orthogonal direction by an objective lens. The fluorescence signal is then transmitted through an emission filter (green) and a dual-channel image splitter (for 2 color imaging) before being imaged onto a high-speed sCMOS camera. **b**, To provide aberration-free imaging, a solid immersion lens (SIL) and oil layer are used for refractive-index matching of both the illumination and collection beams into and out of the glass plate and tissue sample. **c**, As the sample is translated in the primary scanning direction, x , oblique 2D light-sheet images with a width, w , and adjustable height, h , are captured in succession to form a 3D imaging volume. **d**, In contrast to conventional microscopy methods that have a shallow fixed depth of focus and slow 3D imaging rates, the deep depth of focus and adjustable vertical field of view of the open-top light-sheet microscope makes it optimal for both rapid microscopy of irregular/tilted tissue surfaces, and deep volumetric microscopy of clinical specimens. The imaging speeds shown correspond to acquiring single-channel images with height, h . Figure adapted from Liu et al 2017. 18

Figure 1.12: Design of the automated 3D margin scanner prototype (Marginbot). (A) Schematic of the system, (B) Photograph depicting arrangement of the various components used to scan specimen surface in 3D. The number coding in Fig. 1B is explained as follows. Motor A (1) rotates the specimen in the horizontal axis, while motor B (2) moves the optical probe (3) along the specimen surface. Servomotor A (4) enables contact mode and non-contact mode of the optical probe (1) with the specimen placed on the specimen holder (7). Servomotors B (5, 6) move the specimen holder (7) upwards pushing the specimen towards the probe during the contact mode and downwards in the non-contact mode. The compact camera (8) enables image reconstruction of the specimen being assessed for margin analysis. Figure adapted from Nguyen et al 2017..... 19

Figure 3.3: Fourth and prior design iteration. Before imaging begins, a wooden dowel rod (a) ($d = 3\text{mm}$) is placed through the prostatic urethra. The prostate (b) is held in place on the dowel rod with 3D printed clamps (c) that are press-fit onto the rod. The ends of the dowel rod are secured in gimbal joints (d) with set screws. Stepper motor 1 (e) lowers the prostate tissue onto a 50x75 mm glass slide (f) which is secured in stage clamps (not pictured). To lower the prostate onto the slide, stepper motor 1 turns a threaded rod (g) which engages a nut that is prevented from spinning by a 3D printed housing (h). By

preventing the screw from spinning, axial motion is produced as the ‘fixed-nut’ component moves up and down in the z-direction as the threaded rod rotates about the z-axis. On top of the fixed-nut housing rests the free-floating bearing housing (i) which the threaded rod does not engage. The bearing (j) inner diameter engages the gimbal joint with a press fit. The threaded rod, fixed-nut housing, and bearing housing all reside in the 3D printed tower (k) which is fastened to stepper motor 1 via screws. The tower and internal components are attached to the tower via the mounting plate (l) which is attached to the stage (m) with screws. A second gimbal joint connects stepper motor 2 (n) to the other end of the dowel rod. Stepper motor 2 is responsible for the rotation of the dowel rod and therefore the prostate. Changing heights of the bearing housing result in a changing distance from stepper motor 2 to the base of the tower. This is compensated for by allowing stepper motor 2 to slide in its 3D printed housing (o) as the prostate is raised and lowered. The stepper motor 2 housing is attached to the stage via the 3D printed stepper motor 2 housing base plate (p). During image acquisition, the stage moves in the xy-plane in a serpentine pattern above the objective (q) to cover the desired surface area. When the imaging is complete, stepper motor 1 activates, raising the tissue, followed by stepper motor 2, rotating the tissue, followed by stepper motor 1 in the opposite direction, lowering the tissue back onto the slide for the next image acquisition. Prior to the first image being taken, a thumb-screw (r) is adjusted such that a microswitch (s), which is attached to the floating bearing housing, is triggered as the prostate contacts the slide and rests under its own weight. The microswitch interrupts the lowering of the prostate and begins a new image acquisition. The microscope slide booster is not pictured in this case. Figure adapted from Luethy et al. [38]. 23

Figure 3.1: A prostate specimen submerged in DRAQ5, the nucleic acid stain. On the left is deionized water used to rinse the specimen of excess blood. The right shows the beaker holding the cytoplasmic stain Eosin 515..... 25

Figure 3.2: A full image of the prostate mounted on the APPS VR-SIM system..... 26

Figure 3.3: A flow chart of the order of operations of image acquisition using the manual APPS Generation 1..... 28

Equation 2: I_{sim} is the optically-sectioned SIM image and x_1, x_2, x_3 are the raw images taken sequentially during image acquisition..... 29

Figure 3.4: The method of column-by-column collection of images for stitching. Figure adapted from Grid/Collection Stitching Plugin.....30

Figure 3.5: A representative panel of a removed prostate specimen, imaging stained Eosin excited with a 528 nm laser. From Case1071, Panel 1.....30

Figure 3.6: The accompanying image of the cell nuclei marked by the fluorescent TOPRO3 excited at 640 nm from case 1071, Panel 1.....31

Figure 4.1: A conceptual design of the Infrared Transmitter/Receiver sensor. The black arrow represents the infrared beam passing through the prostate.....37

Figure 4.2: A conceptual design of the Photo-Interrupter sensor. The yellow arrow represents the infrared beam which is transmitted from the transmitter to the receiver. As the dowel placed through the prostate lowers into the beam, the connection is interrupted, and the APPS stops.....38

Figure 4.3: A wiring schematic of the Parallax 360 Feedback Continuous Servo [31]. V_{servo} is between 6 and 9 V and must be obtained from an outside source as the Arduino is not capable of providing more than 5 V. The white control wire is attached to digital pin 9 on the Arduino.....42

Figure 4.4: A flow chart of the order of operations of using the digital trigger for the raise function in Arduino.....44

Figure 4.5: The image on the right shows the full assembly of the propeller adapter to turn the bore, the propeller being the top piece. The image on the left shows an exploded view of the assembly with the pieces not glued together.....46

Figure 4.6: A SolidWorks rendering of the tower utilizing the two hex nut system.....48

Figure 4.7: The updated tower of the APPS, with Servo adapter, dual hex nut system, tower height of 4 inches, and the Parallax Feedback 360 Continuous Servo at the top.49

Figure 4.8: A flow chart of the order of operations for image acquisition using the automatic APPS Generation 2.....53

Figure 4.9: Final wiring schematic of APPS Generation 2. Wall Power varies from 6-9 V..... 53

Figure 5.1: Graphical representation of the average voltage threshold and floor for each function per trial.....60

Figure 5.2: A collection of the four outlier functions in which the APPS failed. Figure A depicts the servo motor stalling after only two samples were taken and reaching one of the two trigger values (0V). Figure B shows the servo attempting to work its way out of the locked position but not managing to in the allotted 400 sample time. Figure C shows a similar attempt to figure A and B however after the initial 0.25 V voltage draw the servo “zeroed out.” The term “zeroed out” refers to when the Servo motor has reached its stalling current and can turn no longer, causing it to pulse and wait, giving a zero voltage reading.

Figure D shows a large initial voltage draw which resulted in the triggering of the other stopping value, the voltage threshold of 0.3 V.....62

Figure 5.3: The experiment setup of the repetition experiment, Experiment 3. The stained tissue is wrapped in nylon string and raised and lowered ten times, acquiring an 8x8 panel of images in order to test the precision and accuracy of the raising and lowering functions.....64

Figure 5.4: Numerical Data collected from Panel 1. There was an average voltage during the raise function of 0.1146 V with a minimum voltage of 0.01955 and a maximum voltage of 0.3177 V. As soon as the voltage peaked above 0.3 volts, the servo motor stops rotating and imaging began. There was an average voltage of 0.1156 V for the lowering function with a maximum voltage draw of 0.3372 V and a minimum voltage draw of 0.06354 V...65

Figure 5.5: Line graph representing the maximum voltage and minimum voltage collected for each panel.....67

Figure 5.6: Panel 1 and Panel 2 processed for the uniform image of the SIM frame. Panel 1 is pictured on the left and the nylon string can be clearly seen crossing through the third and fourth column of images taken. Panel 2 is pictured on the right, the nylon string is more in focus and can be seen traversing columns 3 and 4.....67

Figure 5.7: Panel 3 and Panel 4 excited at 470 nm processed for the uniform image of the SIM frame..... 68

Figure 5.8: The process by which the autofocus causes the microscope objective to travel outside of its working distance..... 70

List of Tables:

<i>Table 1.1:</i> Results of the receiver operative curve (ROC) analysis for VR-SIM against standard histopathology, adapted from Wang et al., 2015 [37].....	13
<i>Table 5.1:</i> Table of descriptive statistics of each of the raising and lowering functions of Trial 1 detailing: Maximum Voltage (V), Minimum Voltage (V), Mean Operating Voltage (V), Standard Deviation of the operating voltages (V), the number of samples taken, and the Time taken for each function to complete (s).....	58
<i>Table 5.2:</i> Table of descriptive statistics of each of the raising and lowering functions of Trial 2 detailing: Maximum Voltage (V), Minimum Voltage (V), Mean Operating Voltage (V), Standard Deviation of the operating voltages (V), the number of samples taken, and the Time taken for each function to complete (s).....	58
<i>Table 5.3:</i> Table of descriptive statistics of each of the raising and lowering functions of Trial 3 detailing: Maximum Voltage (V), Minimum Voltage (V), Mean Operating Voltage (V), Standard Deviation of the operating voltages (V), the number of samples taken, and the Time taken for each function to complete (s).....	59
<i>Table 5.4:</i> Table of descriptive statistics of each of the raising and lowering functions of Experiment 3 detailing: Maximum Voltage (V), Minimum Voltage (V), Mean Operating Voltage (V), Standard Deviation of the operating voltages (V), the number of samples taken, and the Time taken for each function to complete (s).	

1. Background

In 2020, the American Cancer society estimates that there will be 1.8 million new cases of cancer in the United States, approximately 4,950 new cases per day [1]. Of these 1.8 million, it is estimated that 606,520 will die from their cancer, approximately 1,662 people per day. That puts cancer as the second leading cause of death for the average US citizen behind heart disease [2]. The National Cancer Institute (NCI) defines cancer as a term for diseases in which abnormal cells divide without control and can invade nearby tissues, known as metastasis [3]. Cancer is a blanket term for these abnormal cell growths and can occur, divide, and grow in any area of the body for a vast variety of reasons. There are several more common manifestations of cancer which include lung cancer (228,820 cases expected in 2020), breast cancer (279,100 cases expected in 2020), and prostate cancer (191,930 expected cases in 2020) [1].

Prostate cancer is expected to be fatal in 33,330 cases in 2020, that is a mortality rate of 17.36%. 33,330 deaths this year means that prostate cancer is the second leading cause of death for men in the US only behind lung cancer. It is estimated that 1 in 9 men will develop prostate cancer in their lifetime, with 66 being the average age of diagnosis and 6 in 10 men above the age of 65 are diagnosed with prostate cancer. Although these numbers are large and the outcome seems negative, it is also estimated that there are currently more than 3.1 million men in the US who have been previously diagnosed with prostate cancer and are still alive [4]. This is due to the fact that unlike some other forms of cancer, there are a variety of treatment options available for men who are diagnosed with prostate cancer.

Treatment and therapy options for prostate cancer include external beam radiation (x ray or proton therapy), chemotherapy, cryotherapy, brachytherapy, hormonal therapy, and surgery. If the prostate cancer is believed to have not metastasized, surgery is often used to attempt to treat and remove the localized cancerous tissue [5]. The main surgical operation for this form of treatment is known as a radical prostatectomy, where the surgeon removes the entire prostate gland with the seminal vesicles as well as minimal surrounding tissue to keep the tumor contained within the gland [5]. Two methods exist for radical prostatectomy surgeries, open and laparoscopic. Open surgery as a method for radical prostatectomy is considered an older method while laparoscopic is more contemporary and typically employs the help of robotic surgery devices [5]. The method for determining the success level of this surgery is performing a margin analysis of the resected tissue. There are two categories of margin status: positive surgical margin and negative surgical margin. A positive surgical margin occurs when a pathologist locates tumor cells at the surgical margin (the edge of the specimen) while a negative surgical margin means that there are no tumor cells present at the border of the removed tissue as shown by figure 1.1.

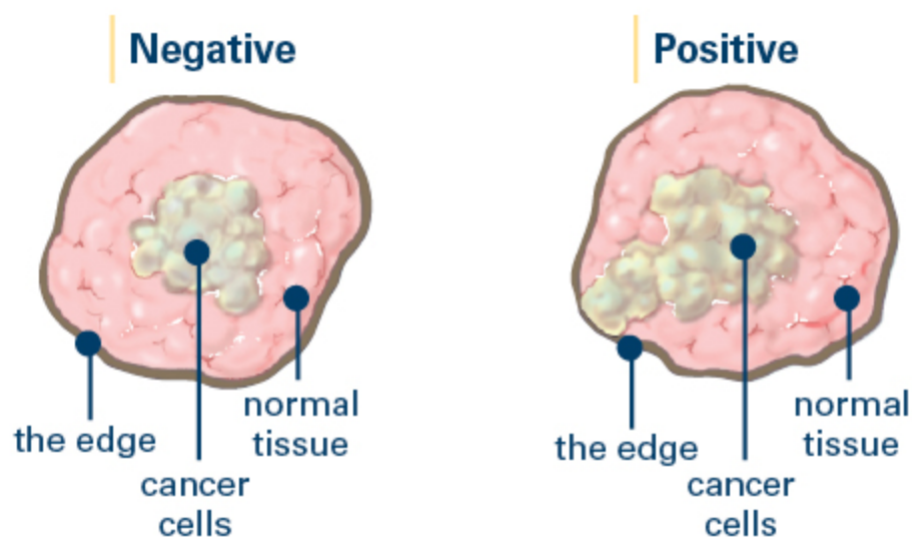


Figure 2.1: Diagram of positive versus negative surgical margins [6].

Positive Surgical Margins (PSMs) are an adverse prognostic factor and are associated with an increased hazard of biochemical recurrence (BCR) and local disease recurrence and often require secondary therapies and treatments [7,8]. It is estimated that somewhere between 11-38% of radical prostatectomy surgeries report PSMs.

The main method and gold standard for margin analysis currently is post-operative formalin fixed paraffin embedded (FFPE) histology. After the tissue is removed from the patient, the external tissue margin is marked with ink for evaluation of the surgical margin and the resected tissue is then fixed in formalin for 24 hours. After the tissue has sat in formalin for 24 hours, cutting begins. The apex of the prostate is removed and radially sectioned, while the rest of the prostate is cut into four quadrants: left anterior, right anterior, left posterior, and right posterior. These quadrants are then individually sliced from apex to base into 3 mm thick pieces which are placed in cassettes to be put through a second round of FFPE. From each slice, a 4 micron section is cut and stained with

Hematoxylin and Eosin (H&E), placed onto a microscope slide, and analyzed by a pathologist to determine the status of the surgical margins. The drawback to this method of margin analysis is that there is a significant time delay between the original surgical procedure and the time when the patient and surgeon know if there needs to be a secondary form of treatment. Secondary treatments for PSMs can be both painful and expensive for the patient as well as the hospital providing care. Currently, there is a method aimed to solve this problem and that is intra-operative correction of PSMs, a method of rapid histology known as targeted Frozen Section Analysis (FSA).

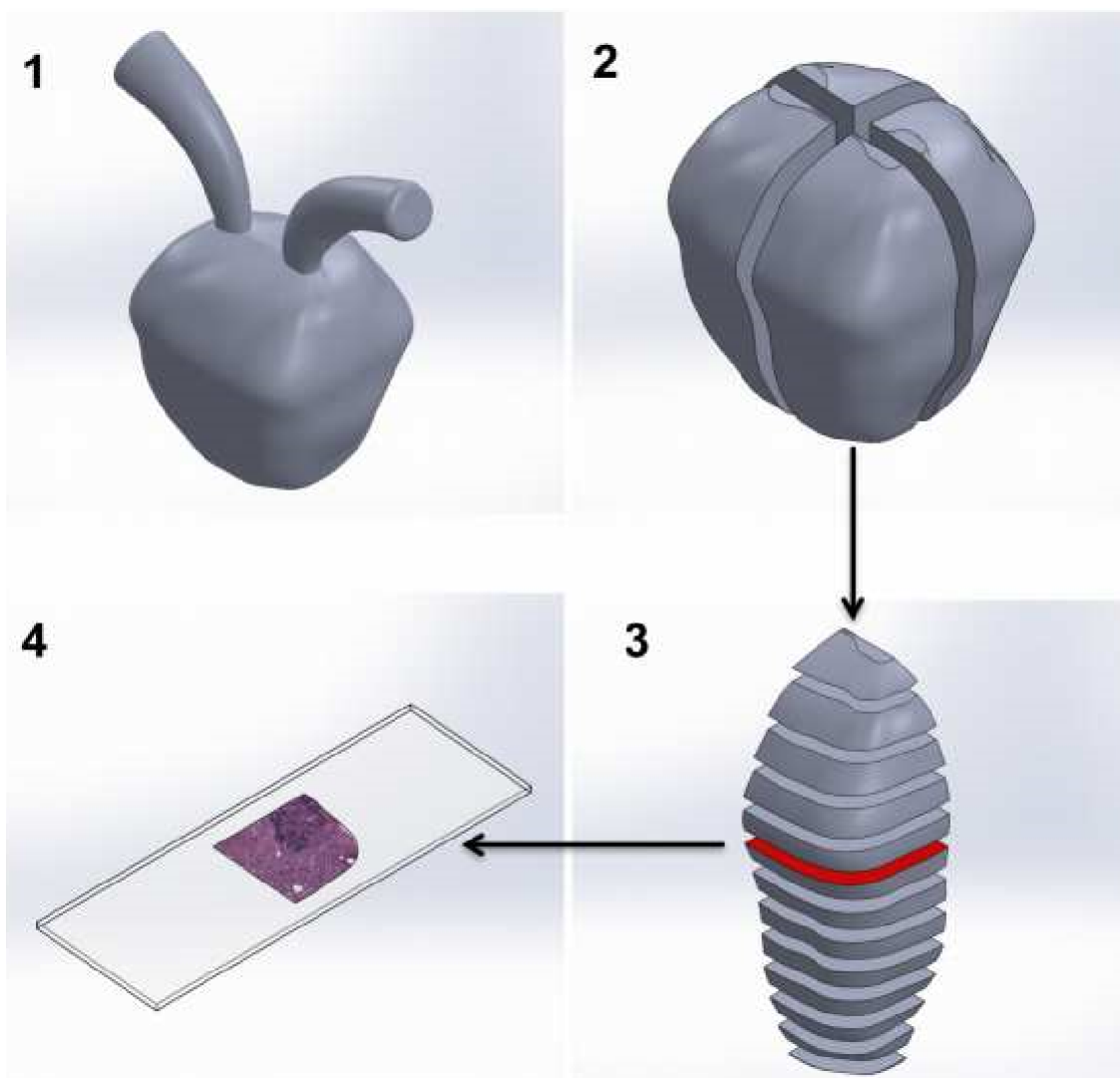
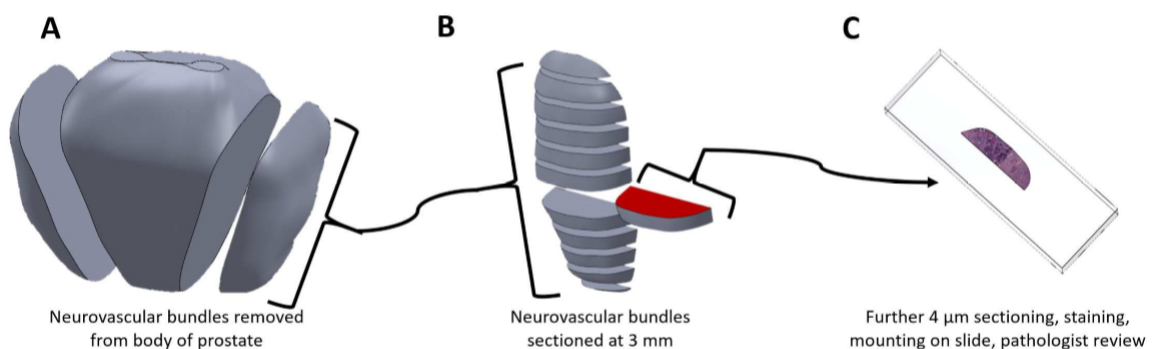


Figure 1.2: Method of prostatectomy specimen sectioning for traditional pathology [39].

For FSA, small shavings of the tissue surface which are deemed suspicious by the surgeon are removed and analyzed by a pathologist in a short period of time intraoperatively to correct a PSM. This targeted approach has low sensitivity due to insufficient sampling. One procedure that has been proposed for intensive or systemic FSA to avoid the sampling problem is known as neurovascular structure-adjacent frozen-section examination (NeuroSAFE), which aims to spare nervous structures around the prostate to improve post-operative quality-of-life [9]. After the tissue is resected, the margin nearest to the tumor of the tissue is inked to maintain anatomical orientation of the tissue and then a large section removes the entire margin. This section is serially sectioned further into 3-4 mm slices and then frozen with liquid CO₂. After freezing, the smaller sections are once again cut into smaller sections with 3-4 micron thickness and are stained with hematoxylin and eosin for pathological review [10]. The process for NeuroSAFE analysis is shown in figure 1.3.



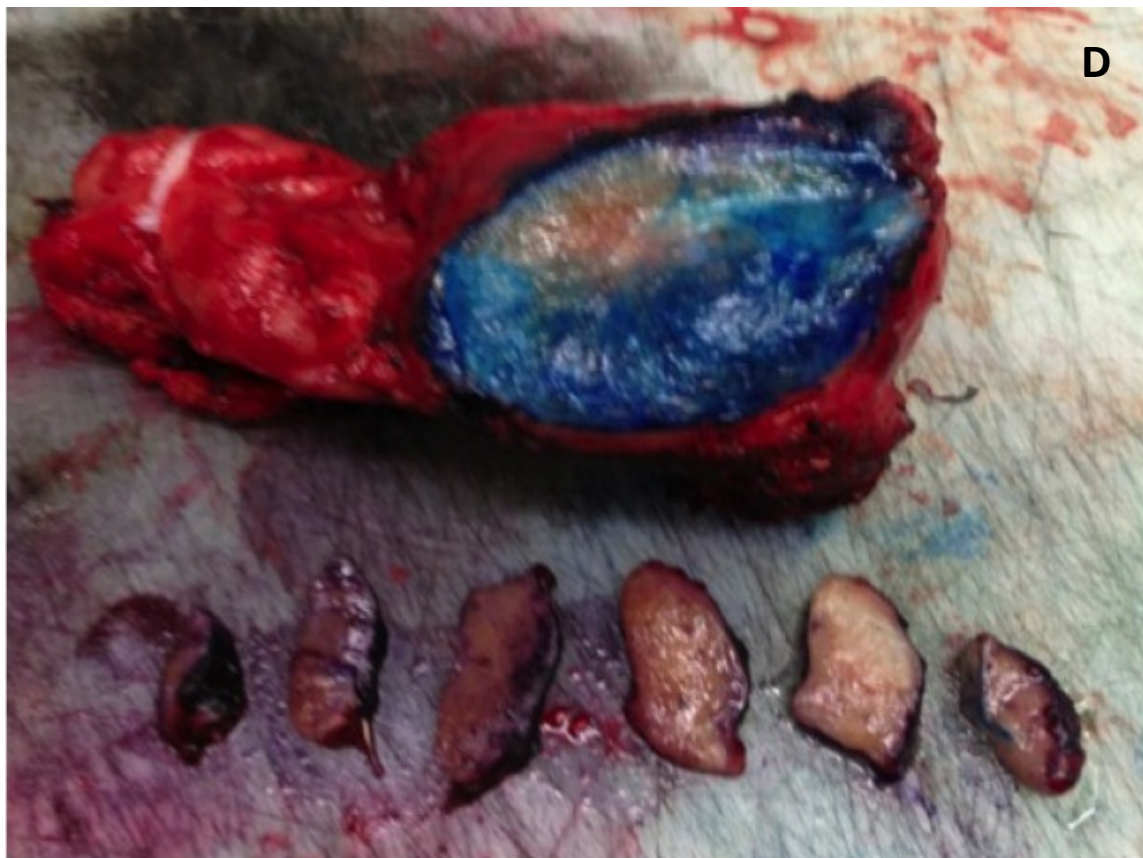


Figure 1.3 A, B, C, D: Images depicting the process of NeuroSAFE intraoperative surgical margin analysis [11,39].

The limitations of targeted FSA are caused by the necessary time and labor involved in the process which makes it difficult to analyze a large portion of the prostate. Other limitations include poor sampling and difficulty cutting the frozen tissue, tissue damage from frozen artifacts, and a lack of comparable data to compare suspicious findings with due to the relatively new nature of frozen section analysis [10,11]. The combination of all these factors leads to a low sensitivity among FSA analyses [12].

A new approach to surgical margin analysis changes the focus of histological image acquisitions from a microscope slide to the resected tissue itself, either in whole or a larger section, known as *Ex Vivo* microscopy. *Ex Vivo* microscopy uses advanced optical techniques to optically-cut rather than physically-cut the tissue, in order to eliminate the

time and labor-intensive cutting steps required for FSA. The current *ex vivo* microscopy techniques used for intraoperative margin analysis and PSM correction include depth-sensitive techniques known as optical coherence tomography and photoacoustic tomography, and optical sectioning techniques such as reflectance and fluorescence scanning confocal microscopy and label-free nonlinear microscopies [13-23].

Optical Coherence Tomography (OCT) is similar to ultrasound, where singly scattered light waves are reflected instead of the typical mechanical waves used in ultrasound. The use of OCT allows the user to create micron-scale cross sections which can be stacked together to make 3D reconstructions of tissue *in situ* in real time with sub-micron resolution and penetration depths of approximately 1-2 mm [24]. OCT has been used for the *ex vivo* detection of cancer in human breast, brain, and prostate tissue [25-28]. The drawback to OCT is that it is unable to achieve the sub-cellular resolution required for surgical margin analysis to evaluate cell morphology. Higher resolution OCT is possible however it requires sometimes damaging tissue penetration. Despite the ability for higher resolution, OCT's reliance on scattering/reflectance contrast may cause it to fall short in its ability to differentiate tissue features in a comparable manner to standard histological approaches.

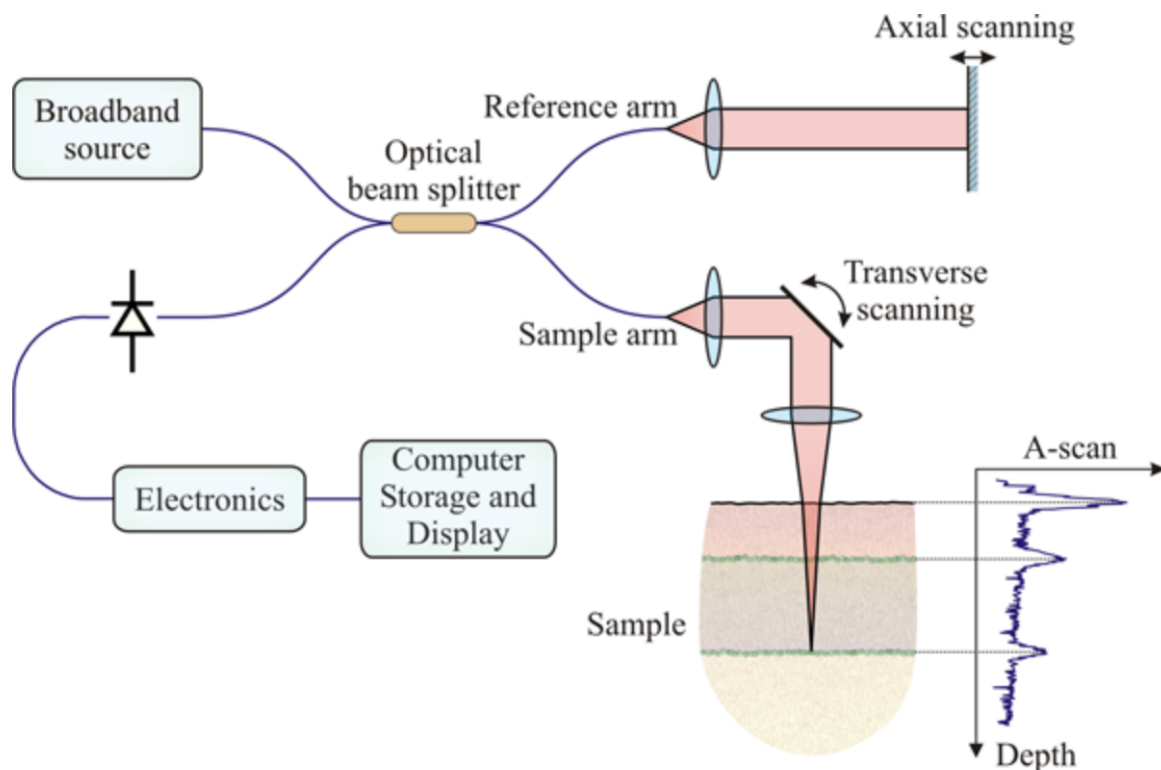


Figure 1.4: Block diagram of the process of Optical Coherence Tomography [29].

Confocal Microscopy or Laser Confocal Scanning Microscopy is an imaging technique which uses a focused laser at the sample conjugate to a pinhole in front of the detector, which allows illumination of a specific area of tissue while reducing the amount of out-of-focus light depending on the size of the pinhole aperture used. This method has the advantage of providing images which are similar to the tissue architecture which is analyzed on traditional histology slides without having to section the tissue [32]. As shown in figure 1.5, the pin hole blocks out-of-focus light by only allowing in focus light from one plane through the detector. While seemingly effective, confocal microscopy has several drawbacks. Primarily, the cost of a commercial confocal microscope is high, approximately \$300,000, which means that it would be difficult for hospitals to adopt this method outside of the research setting. Another challenge confocal microscopy faces is

image acquisition time. Confocal microscopes acquire images one single pixel at a time, making it likely too slow for imaging large tissue areas intraoperatively.

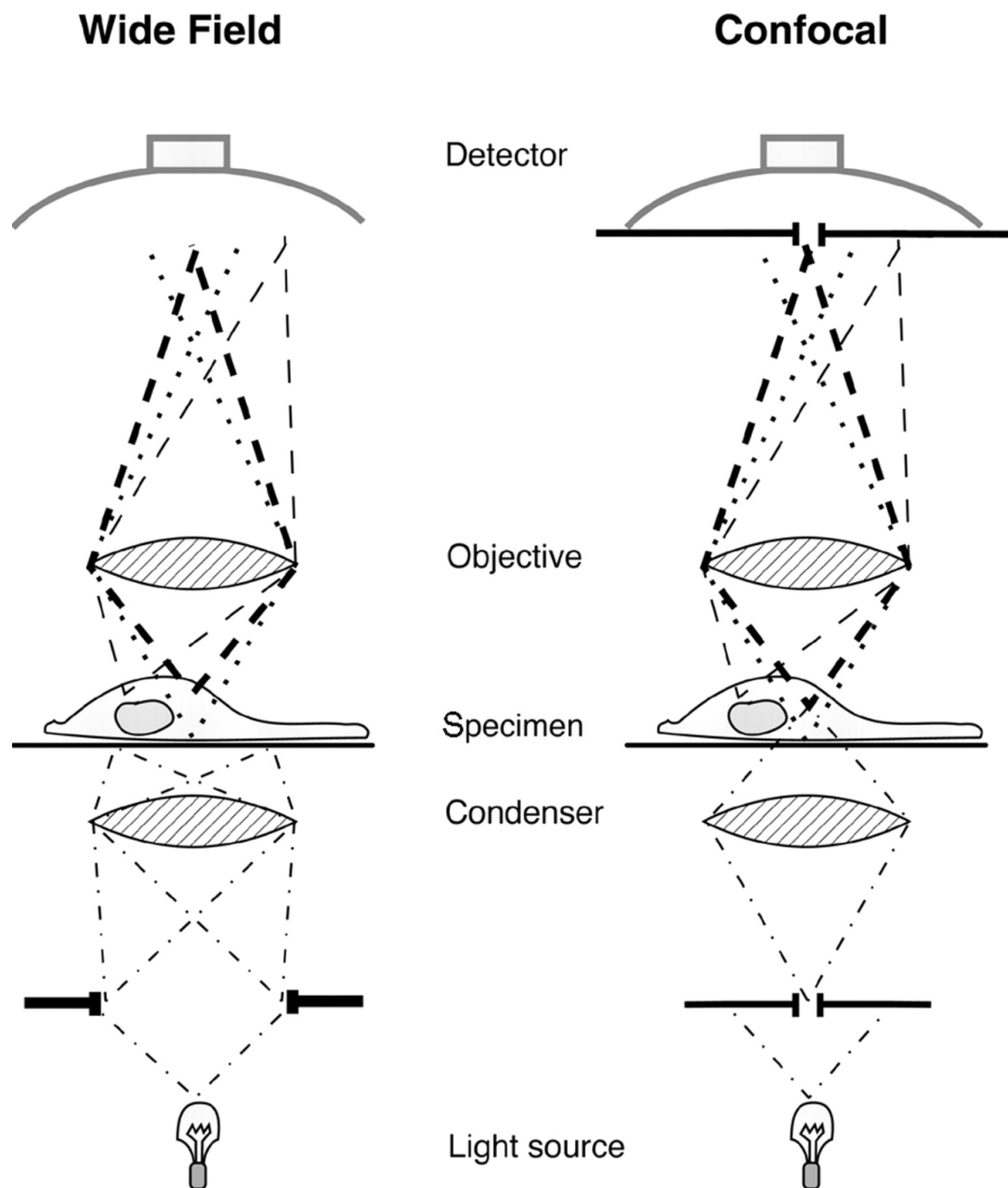


Figure 1.5: Illustration of difference of light pathways in widefield microscopy versus confocal microscopy [33].

Each of these techniques are promising for the imaging of small specimens, ranging from skin cancer resections, core needle biopsies, and gross pathology sections of larger

resected specimens. Despite this, research has not yet been able to provide sub-cellular resolution images of fully intact tumor resection surfaces. This challenge is likely caused by the throughput limitation for sequential beam-scanning approaches. The time it takes for each pixel to fluoresce in order to maintain acceptable signal-to-noise ratios, known as pixel dwell time, is microseconds per pixel. This becomes an issue when imaging large tumor resection specimens at high resolution during the time available intra-operatively. The measurements (pixels) during this time must be maximized in order to achieve high spatial resolution in conjunction with high area coverage, meaning that a very high throughput method is necessary which these methods are not. There is another separate *ex vivo* microscopy method, known as optical-sectioning fluorescence structured illumination microscopy [35,36] may be able to address these limitations. Structured Illumination Microscopy (SIM) is an optical sectioning technique which boasts the attribute of parallel pixel acquisition, meaning the overall pixel-sampling frequency scales to the pixel count of the detector instead of the single pixel exposure time or dwell time.

Our group has developed a microscope which is capable of video-rate (33 frames per second) SIM, VR SIM, at 2048x2048 pixels per frame, corresponding to an image pixel sampling rate of 134.8 million pixels per second. The configuration currently features a single-frame field-of-view of 1.3 mm x 1.3 mm, at a pixel resolution of 4.2 megapixels per frame. The 0.45 NA objective lens used gives a diffraction-limited optical resolution of 0.75 μm at 475, 550, and 640 nm. At 10X magnification the sampling resolution of the scientific complementary metal-oxide semiconductor (sCMOS) camera is 0.65 $\mu\text{m}/\text{pixel}$. Therefore, corresponding to the Nyquist criterion, the lateral resolution image is $2(0.65) = 1.3 \mu\text{m}$, which means the resolution is not limited by diffraction, rather by the sCMOS

pixel size. In order to achieve the same frame rate and pixel density of this system with current sequential beam-scanning techniques, a dwell time of 7 ns would be required, showing a significant increase in speed for an *ex vivo* fluorescence microscopy method. VR-SIM provides a marked speed advantage over other *ex vivo* microscopy methods, while also offering reduced background signal and increased contrast and effective resolution. For this method, the sample is illuminated with a “mask” of light periodically, typically a sinusoidal pattern of light. The “mask” is most efficiently formed by the illuminating optical system onto the in-focus portion of the sample, while the portion of the sample which is out-of-focus is not efficiently modulated with the light mask. Three images are acquired with the pattern phase shifted at 120° in order to cover the entire sample ($3 \times 120 = 360$). The in-focus portion of the sample is recovered by using the RMS square law detection algorithm [35] shown in figure 1.6.

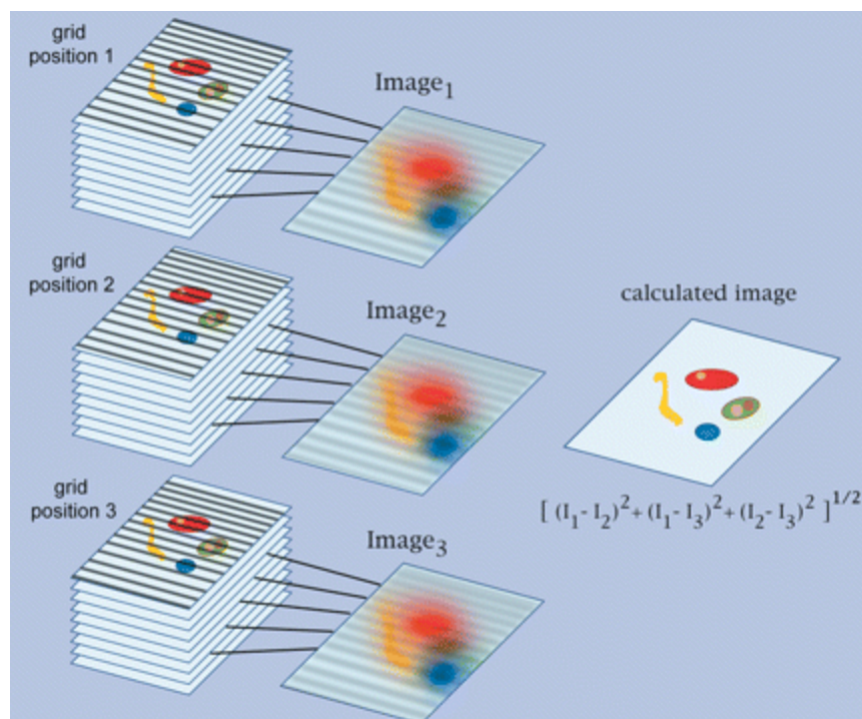


Figure 1.6: The process of calculated SIM Frames. The light source is masked by a regular grid, which casts a pattern of stripes on the in-focus object plane. Three images of the thick object are acquired, shifting the grid by one-third repeat between each acquisition. Each image is the sum of contributions from the in-focus plane, which is shadowed by sharply defined stripes, plus blurred out-of-focus planes without distinct stripes. The square root of the sum of the squared difference images removes the out-of-focus blurred light, giving the in-focus plane [35].

VR-SIM as a method of *ex vivo* imaging is relatively simple compared to its other fluorescent imaging counterparts. For example, the only moving parts of the system are the objective and sample stages. The light efficiency of VR-SIM allows for the use of a non-immersion, long-working-distance 10x objective to image tissue through a standard thickness microscope slide with high throughput and 1.3 μm lateral resolution. Therefore, this method reduces the need for more expensive immersion and short-working distance objectives while also being non-destructive, allowing the entire tissue volume to remain intact. The custom system is shown in figure 1.7.

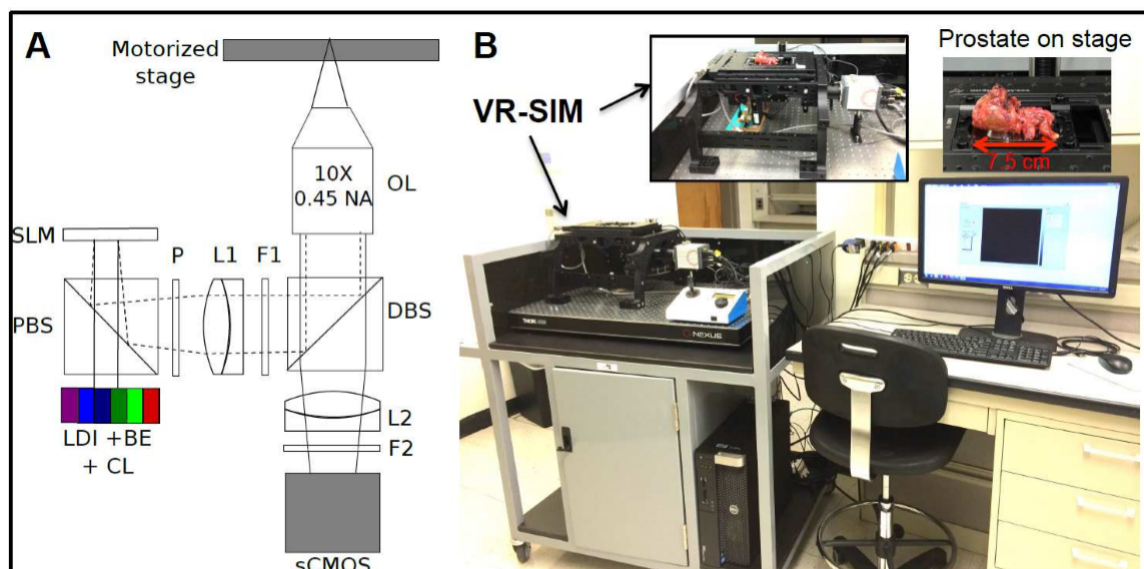


Figure 1.7: A) schematic and B) Photograph of VR-SIM system. LDI – laser engine; BE – beam expander; CL – collimator; SLM – spatial light modulator; PBS – polarizing beamsplitter; P – polarizer; L – achromat lens; F – multiband filter; DBS – multiband

dichroic beamsplitter; OL – objective lens; sCMOS – camera. Figure adapted from Wang et al 2015.

Our lab has previously completed a validation study of VR-SIM using large core prostate biopsies compared to gold-standard H&E, where the diagnostic accuracy on pathologist review resulted in an area under the receiver operative curve (ROC curve) of 0.82-0.88, even in the presence of limited prostate adenocarcinoma content (average 13.7% tumor content per malignant biopsy) (Table 1) [37]. Figure 1.8 depicts VR-SIM images of a biopsy confirmed to contain prostate adenocarcinoma and demonstrates that VR-SIM increases the useful contrast of thick tissue compared to standard widefield microscopy techniques and is comparable to H&E pathology.

	False Positives	False Negatives	Sensitivity (95% CI)	Specificity (95% CI)	PPV	NPV	Accuracy	AUC (95% CI)
Pathologist A (16 M, 18 NM)	4	2	87.5% (60.4%, 97.8%)	77.8% (51.9%, 92.6%)	77.8%	87.5%	82.4%	0.88 (0.75, 1)
Pathologist B (16 M, 18 NM)	2	6	62.5% (35.9%, 83.7%)	88.9% (63.9%, 98.1%)	83.3%	72.7%	76.5%	0.82 (0.69, 0.95)

M = malignant, NM = non-malignant.

Table 1.1: Results of the receiver operative curve (ROC) analysis for VR-SIM against standard histopathology, adapted from Wang et al., 2015 [37].

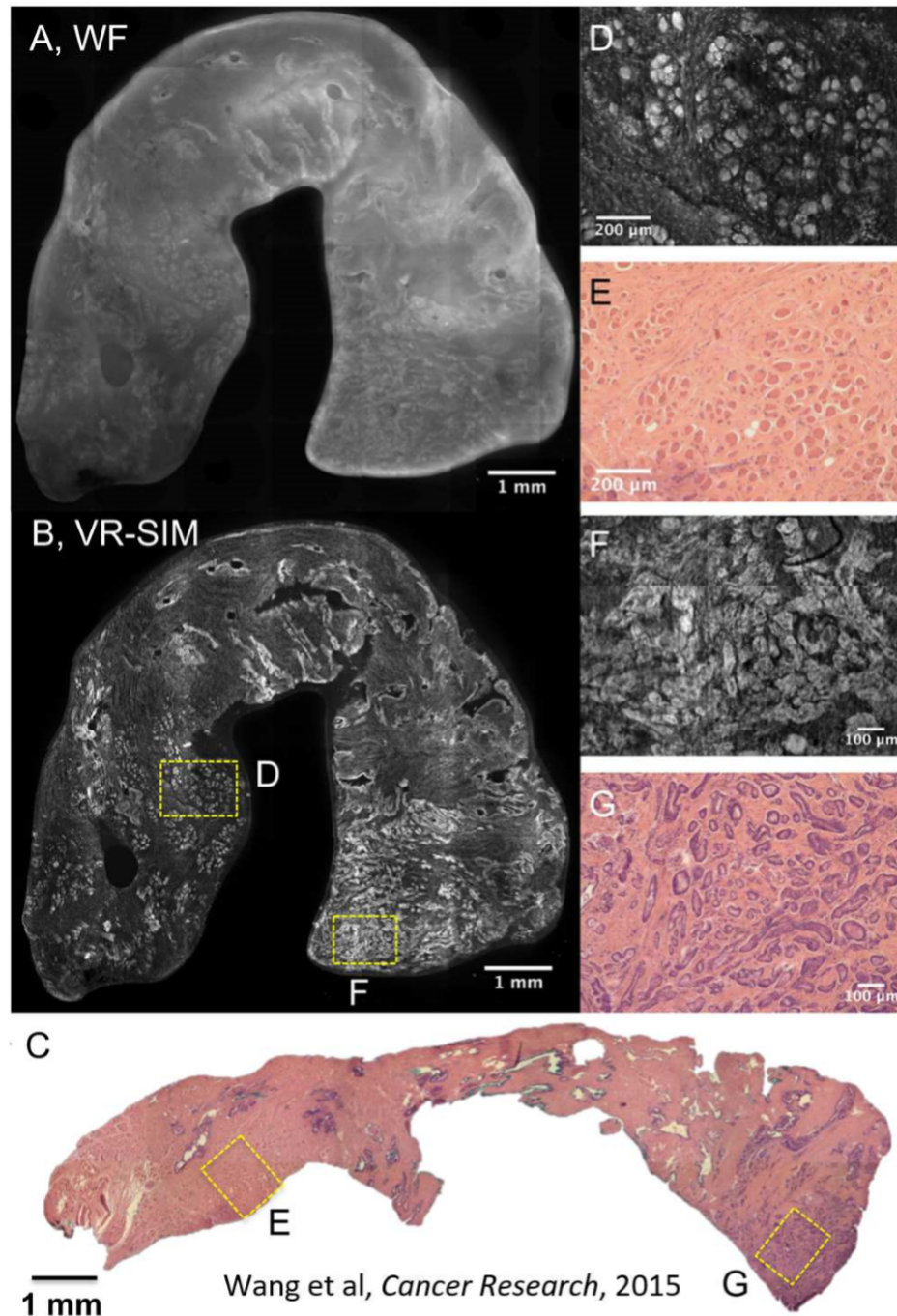


Figure 1.8: VR-SIM images and subsequent H&E slide images of prostate biopsy confirmed as malignant. (A) Wide-field (i.e., without SIM) image of the entire biopsy, (B) VR-SIM mosaic image of the entire biopsy. (C) Digital image of the corresponding H&E section. (D) VR-SIM and (E) H&E zoom images of the regions of interest marked by the correspondingly labeled boxes in B and C, depicting an area of normal skeletal muscle and fibrous stroma. (F) VR-SIM and (G) H&E zoom images of the regions of interest marked

by the correspondingly labeled boxes in B and C, depicting an area of malignant glands. Figure adapted from Wang et al., 2015 [37].

As reported later by Wang et al., 2016, the VR-SIM system was used in order to complete full gigapixel surface imaging of radical prostatectomy specimens to analyze surgical margins for the presence of tumors. The process of this involved placing a wooden dowel through the urethral lumen from apex to base and rotating the prostate manually about the urethra. This allowed for the full surface imaging of the anterior, posterior, right lateral, and left lateral margins of the resected specimens as show by figure 1.9[32].

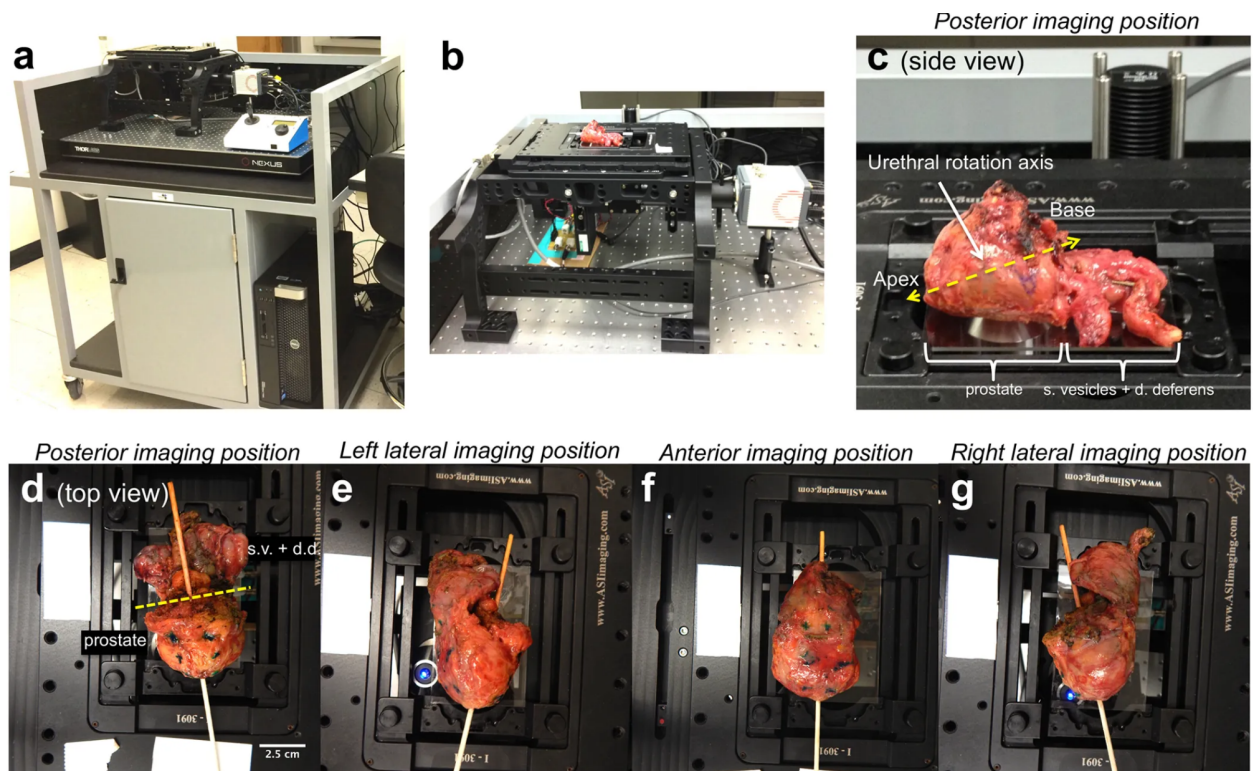


Figure 1.9: (a) The VR-SIM system is mounted on a movable cart. (b) Close-up of the VR-SIM imaging system with a prostate on the microscope stage. The imaging objective is below the prostate in an epi-illumination configuration. (c) Close-up (side view) of the posterior imaging position of the prostate. The posterior surface is contacting the slide; the imaging objective is seen below the prostate. The prostate is rotated about the urethral axis (yellow dashed line) to enable imaging of the prostate circumference. The prostate and the seminal vesicles/ductus deferens are indicated in the photograph. (d–g) Top views of the circumferential imaging positions (posterior, left lateral, anterior, right lateral). A wooden dowel rod is inserted through the urethra to demonstrate the rotation axis between imaging

positions. In **(d)**, the plane between the prostate and the attached seminal vesicles (s.v.) and ductus deferens (d.d.) is indicated by a dashed yellow line. Figure adapted from Wang et al., 2016.

An automated device was built in order to address the challenges posed by manual rotation of the prostate specimen. Luethy et al. found a way to optimize the surface coverage which was possible by treating the prostate specimen as a deforming sphere [40]. By calculating the deformation using an equation (equation 1) for the surface area of a compressed sphere, it was found that it was most optimal to treat the surface of the prostate as a decagon to achieve maximum surface coverage.

$$S_I = 4\left(\frac{\pi(2r^2c - r^2c^2)}{4\pi r^2}\right) = 2c - c^2$$

Equation 1: An equation representing the surface area of a compressed sphere, r represents the radius of the prostate, c represents the degree to which the sphere is compressed, usually denoted by a percentage. Equation adapted from Luethy et al. [38].

By finding the upper limit of the surface compressibility (approximately 20%) it was then possible to find the method for optimized surface coverage. This method was found to be imaging the prostate specimen considering it as a three dimensional decagon, imaging each side of the decagon and rotating the specimen about its central axis (the urethral lumen) 36° in between each round of image acquisition, which will herein be referred to as a “Panel”. The current methods and design of the machine used for the analysis of surgical margins will be discussed and evaluated in chapter 3 and revised in chapter 4.

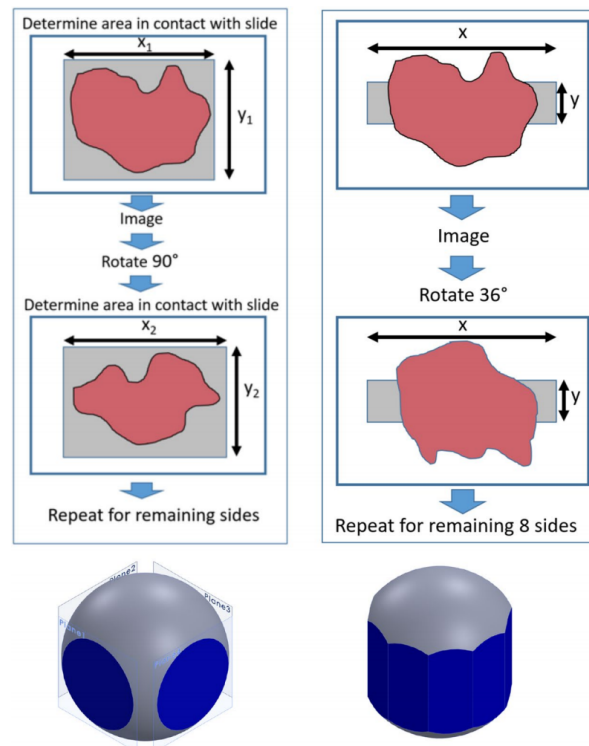


Figure 1.10: A side-by-side comparison of the original method of manual rotation versus the new method of automated rotation.

Other groups around the country are attempting to solve the issue of non-destructive slide-free pathology, whether it is post-operative or intra-operative. Jonathan Liu's group has employed an open-top light sheet microscope which is capable of imaging larger samples of breast and prostate tissue [41]. Their light-sheet microscope is a good solution as it images tissue in 3D by providing deep penetration depths and wide lateral resolution. This method captures the irregularly shaped surfaces of these samples, however the samples imaged with this technology are still sectioned from the original intact specimen and therefore do not truly provide non-destructive pathology of the tissue since the full specimen is no longer fully intact.

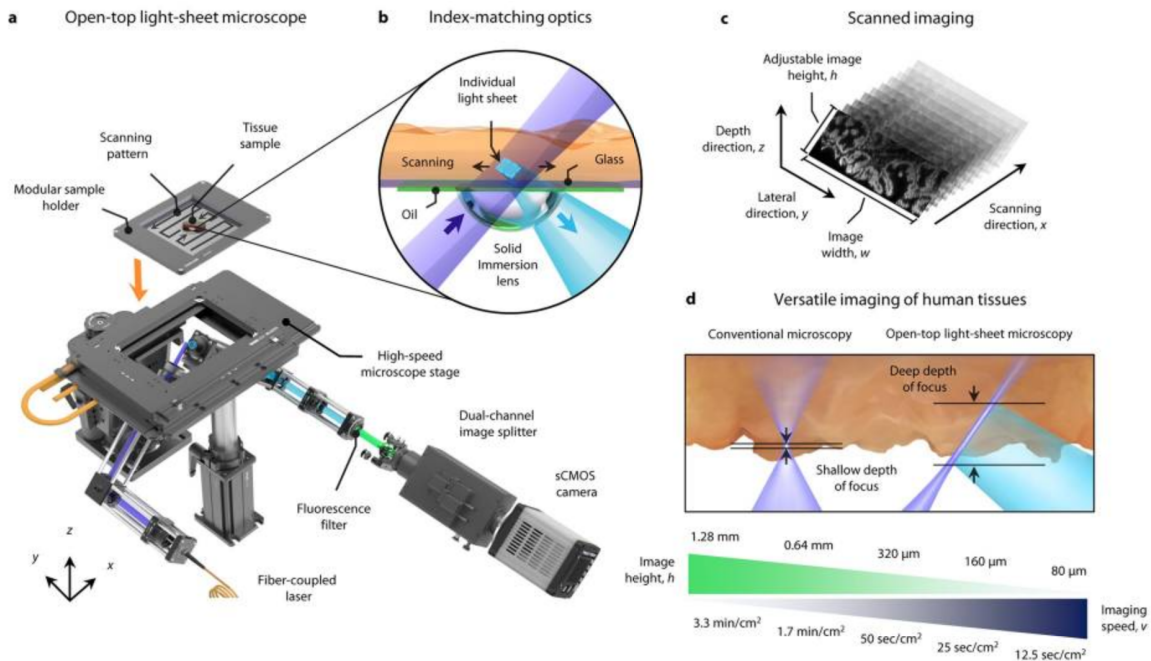


Figure 1.11: Open-top light-sheet microscope for clinical pathology developed by Liu et al. **a**, An illumination light sheet enters the bottom surface of a tissue sample at an oblique 45-deg angle (purple). The specimen(s) is placed on a modular glass-plate sample holder, which is inserted into a two-axis translation stage and scanned in a serpentine pattern of volumetric image strips to enable 3D imaging over a large lateral extent. Fluorescence emission (cyan), which is generated along the light sheet, is collected in the orthogonal direction by an objective lens. The fluorescence signal is then transmitted through an emission filter (green) and a dual-channel image splitter (for 2 color imaging) before being imaged onto a high-speed sCMOS camera. **b**, To provide aberration-free imaging, a solid immersion lens (SIL) and oil layer are used for refractive-index matching of both the illumination and collection beams into and out of the glass plate and tissue sample. **c**, As the sample is translated in the primary scanning direction, x , oblique 2D light-sheet images with a width, w , and adjustable height, h , are captured in succession to form a 3D imaging volume. **d**, In contrast to conventional microscopy methods that have a shallow fixed depth of focus and slow 3D imaging rates, the deep depth of focus and adjustable vertical field of view of the open-top light-sheet microscope makes it optimal for both rapid microscopy of irregular/tilted tissue surfaces, and deep volumetric microscopy of clinical specimens. The imaging speeds shown correspond to acquiring single-channel images with height, h . Figure adapted from Liu et al 2017.

Another group, Anita Mahadevan-Jansen's group, has used Raman spectroscopy paired with an automated margin analysis machine in order to perform 3D margin analysis of intact specimens. The system consists of several angular stepper motors to control the positioning of an optical Raman probe as well as the stage which the specimen is mounted

on as well as stepper motors which control the axial movement of the stage as well. Raman spectroscopy using an optical probe is a high-speed method of margin analysis, however the resolution is not sub-cellular (sub-millimeter) and the system is not automatic [40].

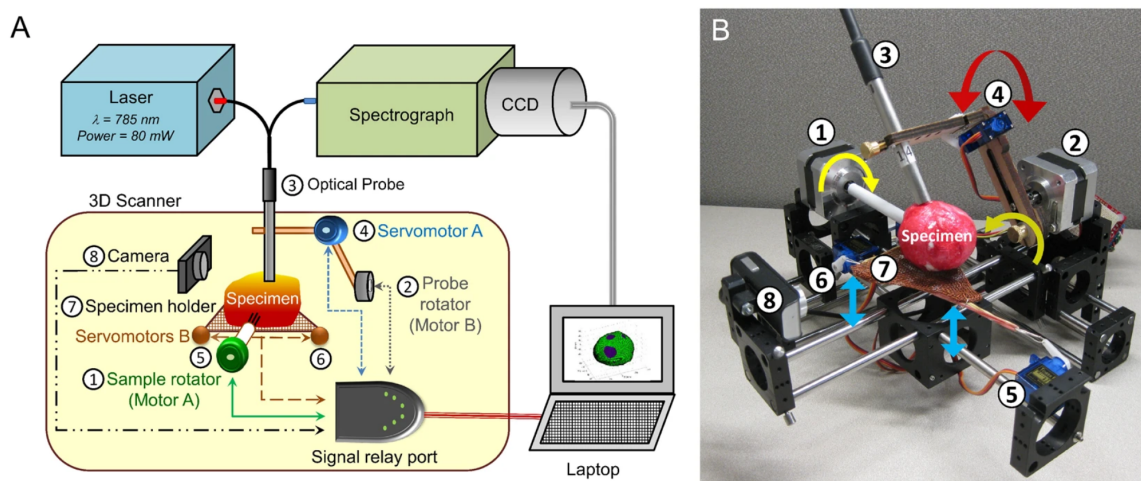


Figure 1.12: Design of the automated 3D margin scanner prototype (Marginbot). (A) Schematic of the system, (B) Photograph depicting arrangement of the various components used to scan specimen surface in 3D. The number coding in Fig. 1B is explained as follows. Motor A (1) rotates the specimen in the horizontal axis, while motor B (2) moves the optical probe (3) along the specimen surface. Servomotor A (4) enables contact mode and non-contact mode of the optical probe (1) with the specimen placed on the specimen holder (7). Servomotors B (5, 6) move the specimen holder (7) upwards pushing the specimen towards the probe during the contact mode and downwards in the non-contact mode. The compact camera (8) enables image reconstruction of the specimen being assessed for margin analysis. Figure adapted from Nguyen et al 2017.

These methods of margin analysis are promising; however, they do not optimally meet standards for usability, tissue-coverage, speed, and resolution to ensure total coverage of an entire resection specimen in intra-operative timeframes for detection of positive tumor margins. In order for intra-operative pathology to be a viable method of margin of margin analysis and replace post-operative pathology, the systems implemented must be high-throughput, sub-cellular resolution, and require non-expert users.

2. Introduction

The Translational Biophotonics Lab has previously reported the utilization of VR-SIM for the capture of gigapixel “histological landscape” *ex vivo* microscopy images of entire radical prostatectomy resection margin surfaces taken immediately after surgical excision, without cutting or physical manipulation of the surgical margin [32]. The advantage of using the VR-SIM method of analysis is that it provides entire coverage of the plane of interest at the surface. This gives an increased chance of capturing tumor cells which are present, reduces the amount of non-surface-related tissue which in turn reduces the amount of time it takes for the pathologist to perform a margin analysis; and does not damage the prostate specimen which allows for proper historical analyses. These characteristics have been proven previously [31] to show that VR-SIM has the capability of competing with and exceeding the standards of current intra-operative methods using the VR-SIM system in conjunction with the Automated Prostate Positioning System. Despite this, several challenges must still be overcome in order to apply the APPS to point-of-care environments. This work aims to address and quantify these challenges based on clinical applications (chapter 3), improve device design by taking the flaws of the current configuration into account (chapter 4), and verify that the improvements made to the current system are sound through bench experiments (chapter 5).

The challenge which limits the APPS from being a viable method for point-of-care margin analysis of resected radical prostatectomy specimens in conjunction with the VR-SIM system is full automation of the device. The fundamental reason for intra-operative analysis is to reduce the amount of time a patient must wait for the results of their surgery.

One of the challenges of NeuroSAFE as stated above, is that there must be a team of several people present in order to complete the intensive work necessary to perform a frozen section analysis of the specimen. The need to have a team of people at the ready for NeuroSAFE is extra coordination pre-operation and is an additional cost for the hospital and patient delivering and receiving treatment respectively. Luethy et al. proved the APPS can perform a comparable analysis in approximately 36 minutes. However, the APPS requires manual control to operate the machine, the stage which the specimen is mounted on, as well as the capturing of the images. The challenges that hinder the APPS from being used in a point-of-care environment will be reviewed in chapter 3. In order to be used in point-of-care environments, the APPS must operate in a manner which is automatic, accurate, and repeatable.

These functional design requirements will be addressed in chapter 4 through a series of experimental tests to find a sensor which is capable of raising and lowering a tissue specimen without additional operator input besides starting the system. This fundamental step will allow the APPS to greatly increase the scope of its ability as a method for point-of-care analysis by making it single-user-operated. The device designed will then be tested in chapter 5 to ensure that the method of sensing utilized follows the functional design requirements set forth by chapter 4.

3. Clinical Evaluation of the Generation 1 APPS system for automated imaging of Radical Prostatectomy specimens.

3.1 Introduction

The Automated Prostate Positioning System (APPS) has gone through several design iterations. The fundamental idea has remained the same, a function for lifting and lowering the prostate onto a microscope slide for imaging and a method for rotating the prostate precisely and accurately to cover the entire circumference. The original functional requirements for the device design of the Generation 1 APPS set by Luethy et al. were:

1. The device must reduce the time required to image the entire circumferential surgical margin to under 20 minutes, the amount of time required to perform one frozen section analysis.
2. The device must cover a larger surface area of the prostate than the previous manual rotation method.
3. The device must fit within the footprint of, and attach to, the 28x16cm VR-SIM microscope stage and must not interfere with stage movement.
4. The device must be made of inexpensive materials to allow for multiple rounds of Prototyping.
5. The device must not damage the surface of the prostate gland.

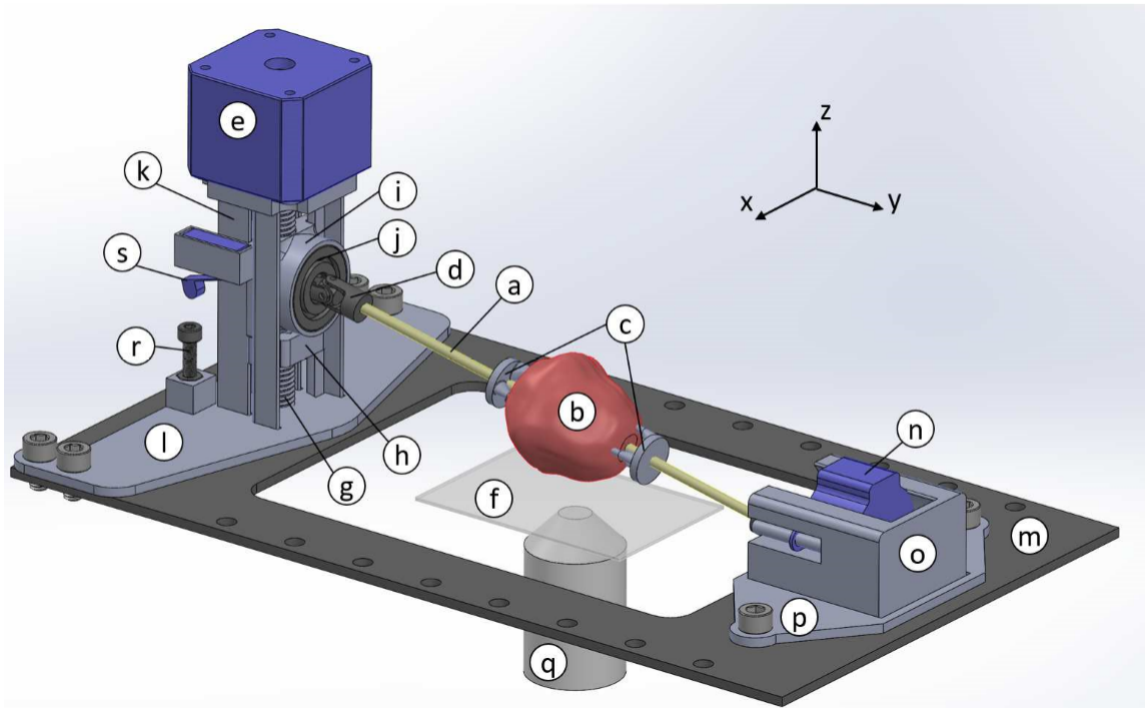


Figure 3.3: Fourth and prior design iteration. Before imaging begins, a wooden dowel rod (a) ($d = 3\text{mm}$) is placed through the prostatic urethra. The prostate (b) is held in place on the dowel rod with 3D printed clamps (c) that are press-fit onto the rod. The ends of the dowel rod are secured in gimbal joints (d) with set screws. Stepper motor 1 (e) lowers the prostate tissue onto a $50 \times 75\text{ mm}$ glass slide (f) which is secured in stage clamps (not pictured). To lower the prostate onto the slide, stepper motor 1 turns a threaded rod (g) which engages a nut that is prevented from spinning by a 3D printed housing (h). By preventing the screw from spinning, axial motion is produced as the ‘fixed-nut’ component moves up and down in the z-direction as the threaded rod rotates about the z-axis. On top of the fixed-nut housing rests the free-floating bearing housing (i) which the threaded rod does not engaged. The bearing (j) inner diameter engages the gimbal joint with a press fit. The threaded rod, fixed-nut housing, and bearing housing all reside in the 3D printed tower (k) which is fastened to stepper motor 1 via screws. The tower and internal components are attached to the tower via the mounting plate (l) which is attached to the stage (m) with screws. A second gimbal joint connects stepper motor 2 (n) to the other end of the dowel rod. Stepper motor 2 is responsible for the rotation of the dowel rod and therefore the prostate. Changing heights of the bearing housing result in a changing distance from stepper motor 2 to the base of the tower. This is compensated for by allowing stepper motor 2 to slide in its 3D printed housing (o) as the prostate is raised and lowered. The stepper motor 2 housing is attached to the stage via the 3D printed stepper motor 2 housing base plate (p). During image acquisition, the stage moves in the xy-plane in a serpentine pattern above the objective (q) to cover the desired surface area. When the imaging is complete, stepper motor 1 activates, raising the tissue, followed by stepper motor 2, rotating the tissue, followed by stepper motor 1 in the opposite direction, lowering the tissue back onto the slide for the next image acquisition. Prior to the first image being taken, a thumb-screw (r) is adjusted such that a microswitch (s), which is attached to the floating bearing housing,

is triggered as the prostate contacts the slide and rests under its own weight. The microswitch interrupts the lowering of the prostate and begins a new image acquisition. The microscope slide booster is not pictured in this case. Figure adapted from Luethy et al. [38].

3.2 Materials and Methods

3.2.1 Sample Acquisition

To date, there have been 15 clinical prostatectomy surgical margin analysis cases using the semi-automated iteration of the APPS shown in figure 3.3. These cases, using a dual stain method of either DRAQ5 or TOPRO3 as nuclear stains and Eosin 515 as a cytoplasmic stain allow for the processing of images which are similar to those analyzed by pathologists using gold standard H&E FFPE through digital pseudo-coloring. These cases take approximately 2 hours to complete.

3.2.2 Experimental methodology

The process of a typical clinical imaging experiment is broken into several steps. The first step is a consenting process where the clinical research coordinator meets with potential participants to receive their consent in using the resected specimen for our study. This occurs several days prior to the surgery. Once the operation is under way, the prostate specimen is resected and then will possibly undergo different routes before reaching our lab. Depending on the operating surgeon, the specimen may sit in the abdomen until the operation has been completed or be handed to the clinical coordinator immediately after excision. Depending on when the prostate is received, it is possible for this handling method to cause experimental results to vary.

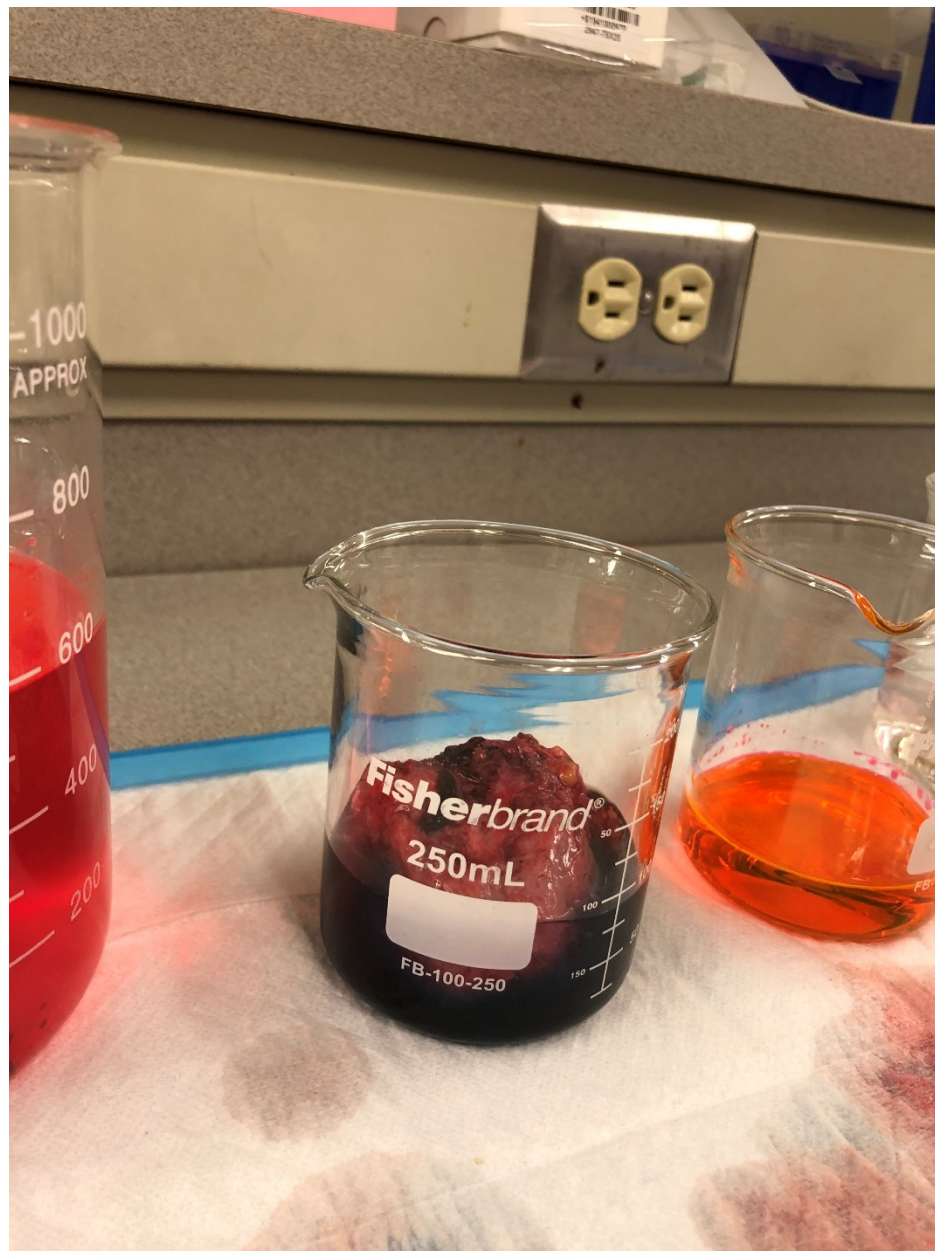


Figure 3.1: A prostate specimen submerged in DRAQ5, the nucleic acid stain. On the left is deionized water used to rinse the specimen of excess blood. The right shows the beaker holding the cytoplasmic stain Eosin 515.

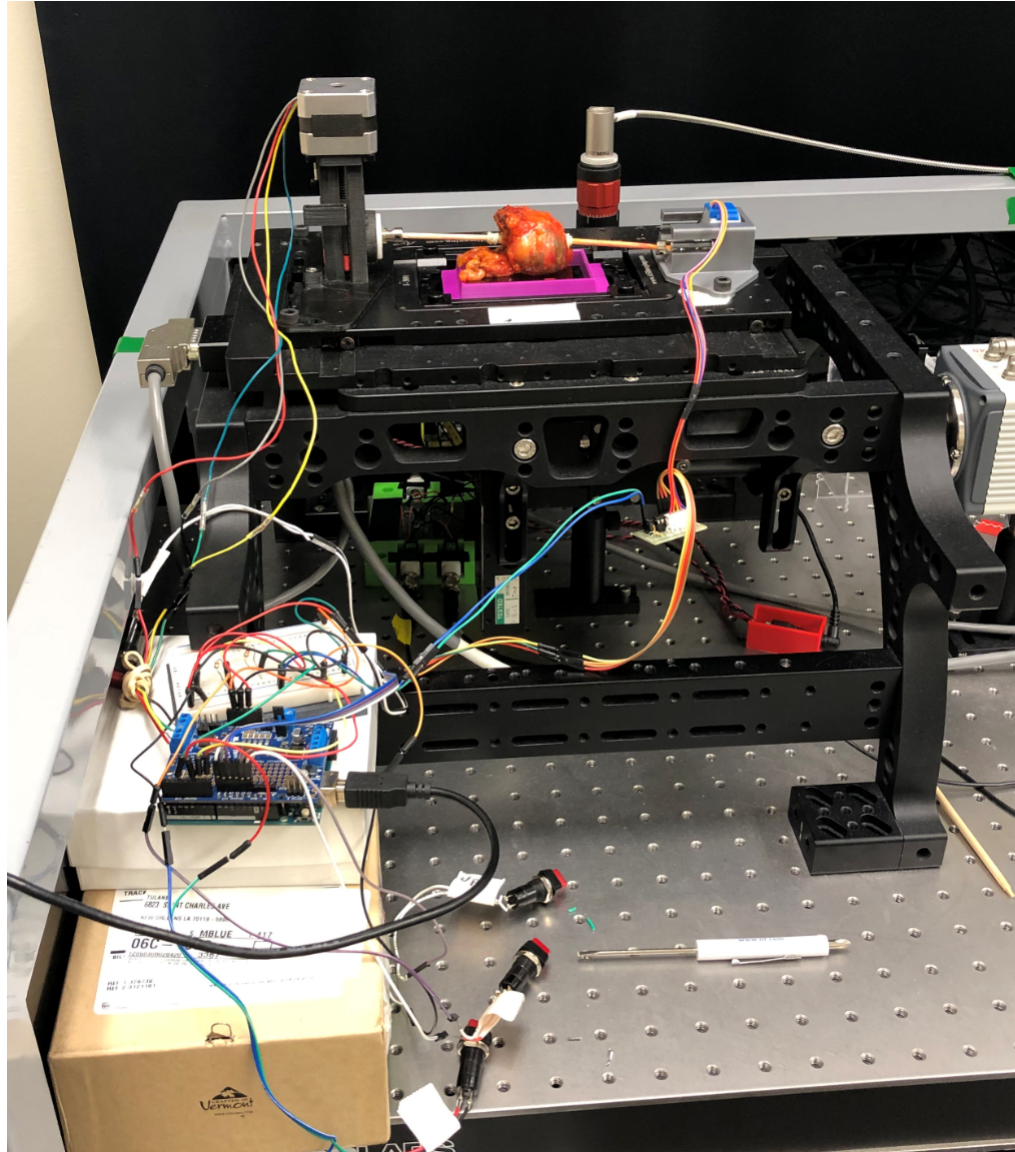


Figure 3.2: A full image of the prostate mounted on the APPS VR-SIM system.

3.2.3 Sample preparation

The staining system was set up prior to receiving the specimen. Once the specimen is received, it was removed from its container and immediately rinsed in deionized water to remove excess blood from the operation. After this, the specimen was placed in two

separate stains. The first stain is a nuclear stain which binds to the DNA of the cells of the specimen, which fluoresces to highlight the nuclei of each cell. The second stain is an acidophilic stain which stains the cytoplasm of each cell along with the stroma, which fluoresces to show the architectural and structural features of the surface of the specimen. The two nuclear stains which have been used for these experiments are DRAQ5 and TOPRO 3. The cytoplasmic stain used is Eosin 515. The specimen is placed in the nuclear stain for 3 minutes using a solution of PBS and 300 μM of the nuclear stain. After three minutes the specimen is rinsed in PBS and dried. Then, the specimen is placed in a solution of 1:4 eosin 515 to 200 proof ethanol for 40 seconds and rinsed in ethanol to remove excess moisture. The wooden dowel is then placed through the urethral lumen of the prostate. The prostate is then oriented such that the seminal vesicles are placed towards the tower and the apex of the prostate faced stepper motor 2. The process for semi-automated imaging of the specimen is detailed in figure 3.3.

3.2.4 Operation of the APPS System

The system was designed in order to be operated by a single operator throughout the process of imaging. In order to perform programmed functions of the APPS, three buttons must be used. The buttons used in this system were electronic grill ignitors which were purchased at home depot. The first button is the raise button, which must be depressed continuously until the user deems the specimen to be fully cleared of the glass slide. Once the user removes pressure from the button, the digital pin of the arduino it is connected to reads a low state and signals the National Electrical Manufacturer Association (NEMA) stepper motor (stepper motor 1) to stop turning steps. At this point, the user would then depress the second button, the rotate this button. As this button is depressed

instantaneously, the digital pin it is connected to reads high and signals stepper motor 2 to step 200 steps in order to rotate the specimen 36 degrees. After this has concluded, the user then must depress the third button continuously, the lower button. The NEMA motor will then once again be signaled by the state change of a digital pin to begin rotating in the opposite direction in order to lower the specimen. The user knows that the specimen has lowered to the desired level when they can view the 3D printed housing of the hex nut lower away from the 3D printed bearing housing.

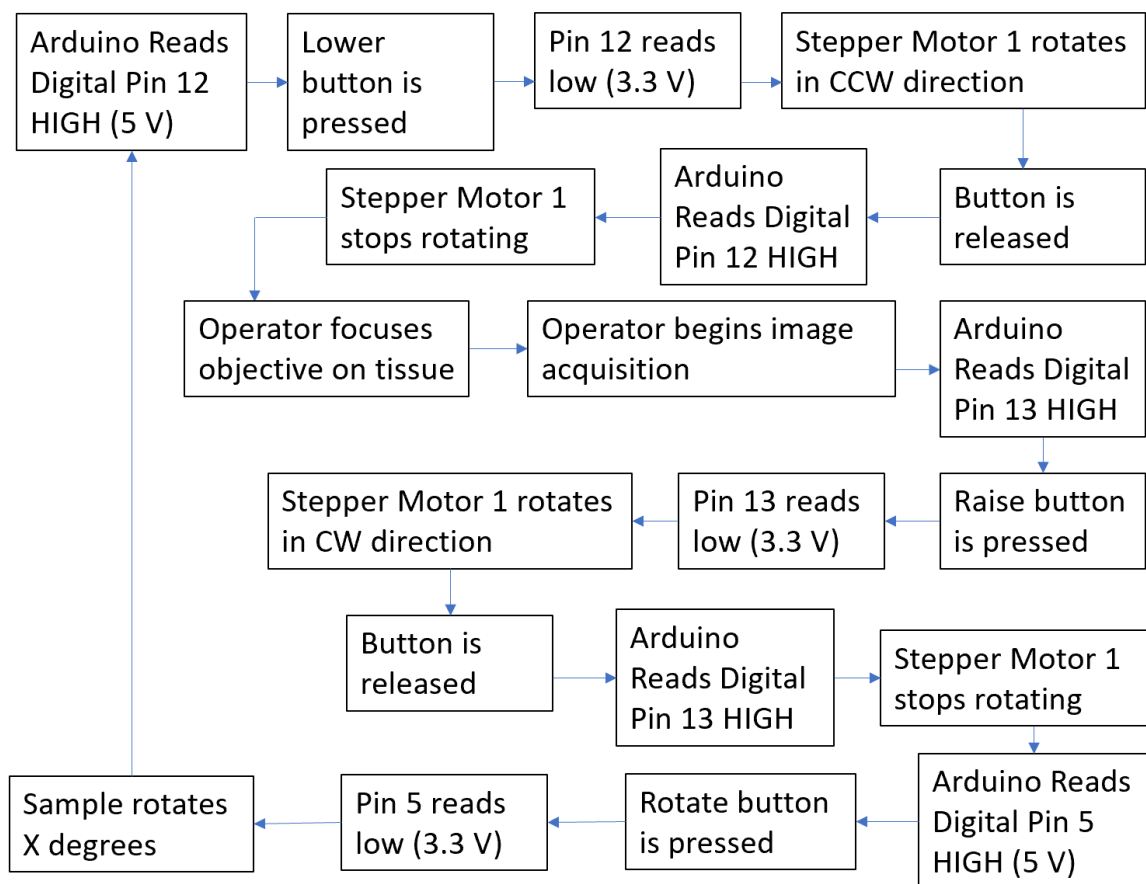


Figure 3.3: A flow chart of the order of operations of image acquisition using the manual APPS Generation 1.

The images which are acquired during this process are the aggregate of the 3 phase shifted patterned photos in order to achieve the SIM image as described in Chapter 1. However, in order to achieve the panels shown in Figure A,B, several operations of image processing must occur. The first is a custom MATLAB code which manipulates the raw images taken in order to create uniform and sectioned images from the manipulated data. Uniform images are the collection of the evaluated pixels from each raw image added together from a single panel, then rescaled from 0 to 1. Sectioned images are the square root of the sum of each evaluated pixel from the raw images squared. This is shown by equation 2 described by Neil et al [35].

$$I_{sim} = \sqrt{(x_1 - x_2)^2 + (x_2 - x_3)^2 + (x_1 - x_3)^2}$$

Equation 2: I_{sim} is the optically sectioned SIM image and x_1, x_2, x_3 are the raw images taken sequentially during image acquisition.

Sectioned images are then used as the presented frame of each panel which leads to the second set of image processing. The sectioned and uniform images are then numbered from 01 up to the total number of images which were required to cover the panel (a 12x12 panel would yield 144 sectioned and 144 uniform images). These numbers are then read into ImageJ, a common application used for image analysis, and stitched together using a grid collection system. The grid collection system stitches images together in the same manner in which they were acquired which is by stitching columns from top to bottom row-by-row then proceeding to stitch on another column moving from left to right, shown in figure . Two panels processed and stitched (one of each stain) can be seen below.

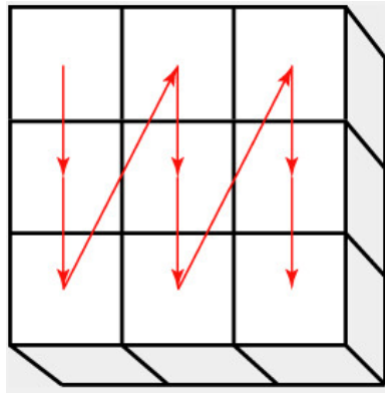


Figure 3.4: The method of column-by-column collection of images for stitching. Figure adapted from Grid/Collection Stitching Plugin.

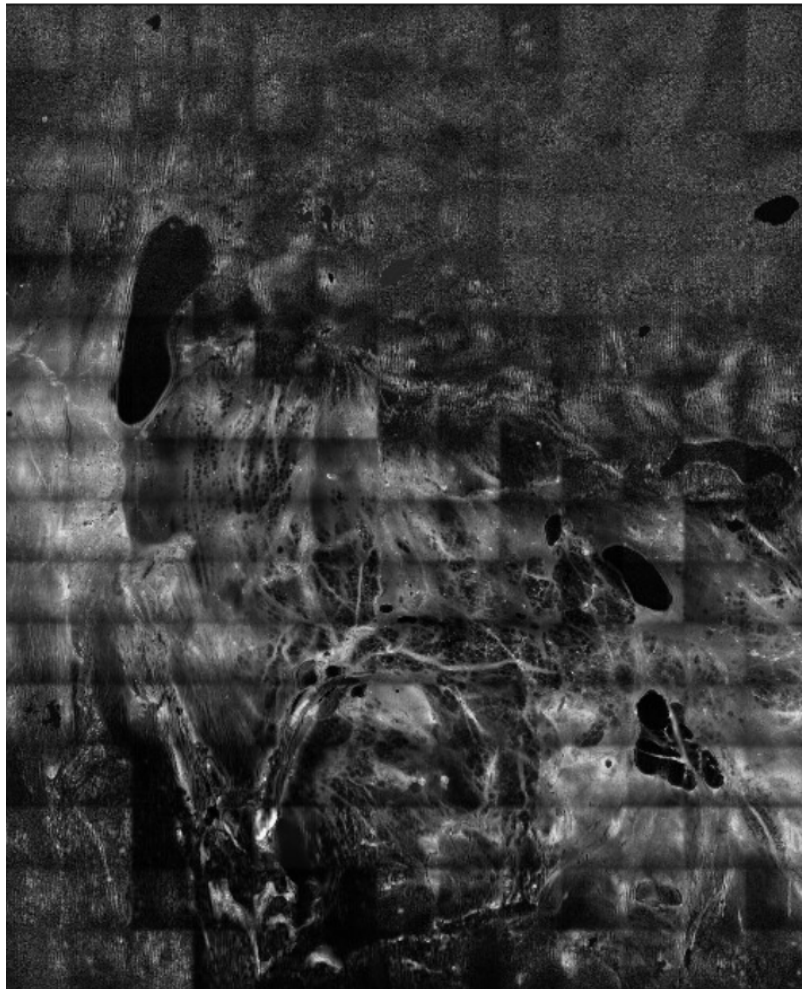


Figure 3.5: A representative panel of a removed prostate specimen, imaging stained Eosin excited with a 528 nm laser. From Case1071, Panel 1.



Figure 3.6: The accompanying image of the cell nuclei marked by the fluorescent TOPRO3 excited at 640 nm from case 1071, Panel 1.

3.3 Results and Discussion

Figures 3.5 and 3.6 show example imaging results from the use of the Generation 1 APPS system on radical prostatectomy specimens. The image results above are of decent quality however they are lacking in several aspects. One of these aspects is the focus of the images. Each image is mostly in focus, however the areas which appear “spotted” (consisting mainly of noise) are the result of loss of focus and rejection by the SIM algorithm. This is caused by the inability to focus on part of the prostate which are not

firmly placed onto the microscope slide. The use of autofocus mitigates this problem somewhat, however there are issues with this method which are discussed in chapter 5.

This set of operations works well within the research environment. Clinical research experiments are typically handled with two to three lab members at a time therefore one person can operate the APPS while the others monitor the data being collected. However, in eventual clinical practice, it would be difficult to have a nurse or other technician takes precious time away from their duties to operate the APPS for the entire course of the image process in a point-of-care environment. The original APPS design incorporated a method for handling this issue in order to automate the system. A microswitch was employed as shown by figure 3.4. An initial button press of a fourth button, labeled the 'Go' button, would cause stepper motor 1 to lower the specimen. Once a desired height was reached, the microswitch would depress when coming into contact with an adjustable thumb-screw placed below it. The depressing of the microswitch would signal stepper motor 1 to stop rotating and the specimen would be flush against the microscope slide. The VR-SIM system would then begin the imaging process.

This method solved the initial fundamental problem of finding a sensor which would be able to signal a stopping function as the specimen reaches the desired level. However, in order for this system to work, measurements of the diameter of the specimen would be required in order to adjust the height of the screw. These extra steps typically require several attempts of manual lowering in order to find the appropriate height. Also, the prostates are not spherical, and typically have variable radii both longitudinally and circumferentially. Therefore, a thumbscrew that may be appropriate for one rotation of the specimen may be completely inaccurate for a different rotation due to the variable shape

of the specimen. This would require that the thumbscrew be re-set for every rotation, reducing the value of automation of the system. The time necessary to perform these operations are critical during an intra-operative attempt to correct surgical margins. This challenge required the need for a sensor which is able to regulate itself, regardless of the size of the sample.

The use of an external trigger such as a physical button or switch are typically useful in terms of ease of use for the user. Simply pressing a button or flipping a switch is how nearly every electronic appliance or device is used today. However, external triggers lead to more wiring (i.e. greater complexity) and possible modes of failure. A common issue with the current APPS is that often a button will operate without being physically pressed by the user. This proves to be a problem when a panel (the mosaic imaging of the side of the specimen which is in contact with the slide) is in the process of imaging and stepper motor 1 begins lifting the specimen. This ruins the panel and the panel must be restarted, costing valuable time.

Due to the nature of human anatomical variance, as well as differing types and stages of cancer, the prostates which are received are variable in size. It is easier to envision the variability in size from a golf ball to a large walnut. This large variation in size is difficult to account for when trying to produce exact dimensions for optimization. The most notable challenge is the height. In order for the dowel system to work, the dowel must be long enough such that it will not remove itself from either of the gimbal joints when being raised or lowered. If the tower portion is too tall, stepper motor 2 would be pulled off of its track. However, if the tower is too short, the prostate may not be raised off of the glass and therefore unable to actually rotate and image by itself. In order to solve this problem, the

height of the tower would need to be increased without exceeding the limits of the slider. When changing the height of the tower, the user must also consider that the height of the bore must change. The current bore is a custom tapped polyurethane plastic bore which has a custom fitted adapter for the stepper motor 2. In order to make the system more widely adaptable, it is not feasible to continue using a bore which is created through a custom tapping process.

Taking these challenges into consideration, a new device will be designed taking the previous functional requirements into account as well as adding a new set. The goal of this new device will be reducing the need for more than one singular user input with the intention of full surface specimen imaging being completed by one person.

4. Experimental Testing and Results of the Device Design of the Generation 2 APPS

4.1. Introduction and Functional Requirements for Generation 2

After the functional requirements presented in chapter 3 were proven by the previous standing iteration, new functional requirements were set in place for the second-generation configuration of the automated system. The new requirements were as follows:

1. The device must be fully automatic, defined by inputting a “Start” signal and completing the full ten panel rotational process necessary for image acquisition before coming to a stop, with only one user step required after mounting the tissue on the system.
2. The device must be able to accurately image the full circumference of the prostate.
3. The must be able to complete the image process accurately and automatically in a repeated fashion consistently.

As stated, automation was defined as a single user input (i.e. click “Start”) which would then output the full circumferential images required for proper margin analysis. At the most fundamental level, the process of successful automation is controlled by one critical subfunction: the ability for the system to automatically recognize when the prostate has reached its optimal placement on the surface of the microscope slide. The manual operations required to use the prior iteration of automation do not pass the single input test. To address the fundamental problem of the device recognizing the placement of the prostate on its own, several different sensor methods were tried.

4.2 Experimental Approach to Design

The major task for redesign of the Gen 1 APPS system was to define a suitable method of automatic detection of when the tissue is properly interfaced with the imaging slide, regardless of shape or orientation.

4.2.1. Infrared Sensor

The first method which was attempted was using infrared light (IR) as a method of sensing when the prostate was flush with the microscope slide. An Gikfun HX1838 Infrared Remote Control Module was selected as the IR transmitter/receiver combination. This control module uses an SFH 4550 IR emitter at a wavelength of 850 nm. The initial method of testing involved placing an IR LED on one side of the prostate mounted on the stage while placing its receiving photodiode on the opposite side of the receiver. In theory, once the prostate was lowered into the path of the IR transmission of light and broke the connection, the APPS would stop, and imaging would be able to commence. The problem with this method was that the transmission was never broken. The IR light was able to be successfully received by the photodiode through the samples which was being used to test (specifically, fresh bovine muscle obtained from the supermarket). The key problem here is that the IR emitter used was transmitting at a wavelength of 850 nm. 850 nm falls into the near infrared spectrum which coincides with the near-infrared optical window for biological tissue (650-1350 nm). Since 850 nm is within this range, the IR light which was transmitted will always pass through the tissue. This method ended up being the wrong application of an IR transmitter receiver combination, as it also required input from its remote control device rather than commands from the Arduino device. Therefore, this

method did not meet any of the intended requirements as it was not automatic, not accurate, and not repeatable.

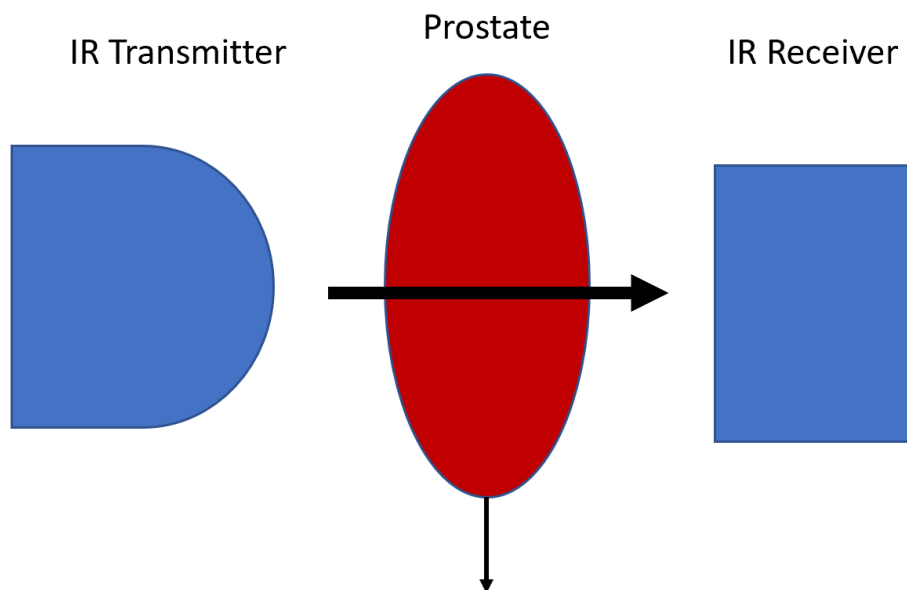


Figure 4.1: A conceptual design of the Infrared Transmitter/Receiver sensor. The black arrow represents the infrared beam passing through the prostate.

Learning from the shortcomings of the IR transmitter, a photo-interrupter (PI) was chosen as a suitable replacement for the IR transmitter. The use of a PI came in the form of an idea when considering how a garage door functions. As an automatic garage door slowly lowers, there is a photo-interrupter approximately ankle height above the ground which sits at either end of the door. If the IR beam is delayed or blocked in any fashion, the door stops lowering. Much like the first IR transmitter/receiver, this was an IR receiver with the purpose of being blocked rather than passing through whatever obstruction was presented.

A similar experimental format was used now that the proper sensor had been selected. The transmitting end of the PI was placed on the tower side of the APPS just off of the microscope slide with the receiver opposite to it. As the dowel placed through was lowered into the plane of the transmitter's beam, the prostate stopped lowering. This would have been considered a success, however the sample had stopped short of the microscope slide. This meant that in order to use the PI as a sensor, there would need to be a measurement of the prostate gland once it was removed and an input necessary to cause a time delay that would allow for the prostate to rest on the slide. The measurement would be required in order to properly calibrate the distance of passing through or time delay that the Arduino would need to account for in order to allow the sample to reach the microscope slide. This meant that the PI would not be a viable option as it did not fulfill the requirement for automation.

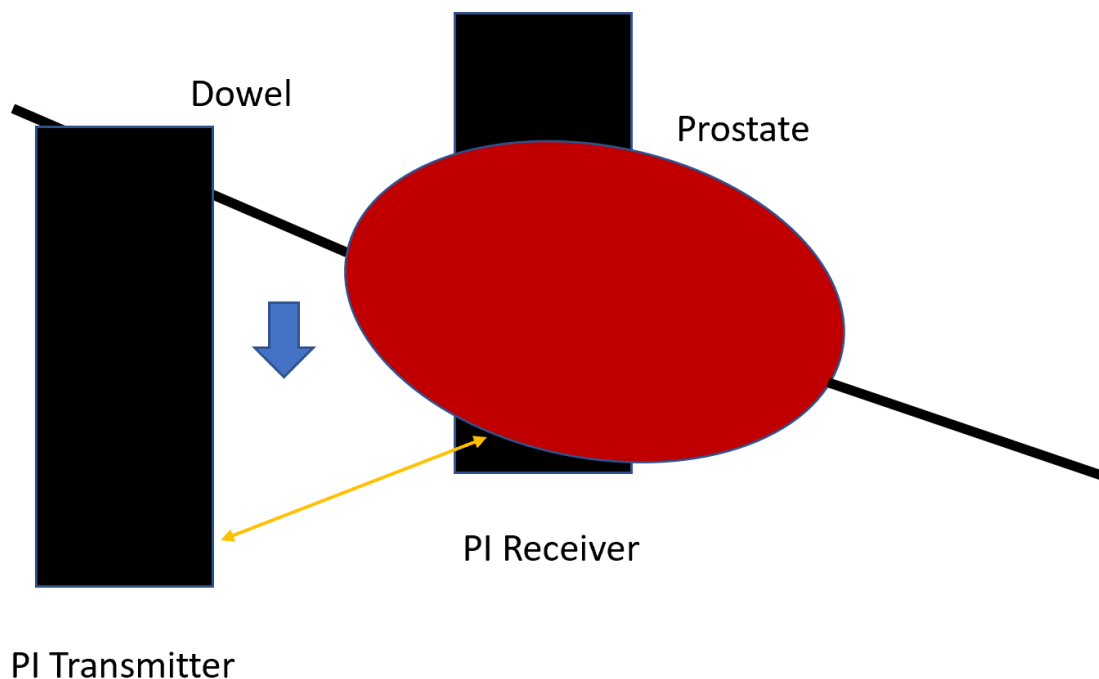


Figure 4.2: A conceptual design of the Photo-Interrupter sensor. The yellow arrow represents the infrared beam which is transmitted from the transmitter to the receiver. As the dowel placed through the prostate lowers into the beam, the connection is interrupted, and the APPS stops.

4.2.2. Evaluation of other sensing mechanisms

After consideration of the challenges faced by the sensors used prior, a pivot was required in order to overcome the problems at hand. Two other sensors were considered theoretically, although they were never tested. An accelerometer was considered as a method for sensing the change in velocity of the tissue as it was lowered onto the microscope slide. However, it was thought that the change in velocity would be minimal and therefore difficult to quantify using an accelerometer. The other option was to use a flexible pressure sensor and/or strain gauge attached to the microscope slide. In theory, the sensor would adhere to the bottom of the microscope slide but it was not selected as the sensor would interfere with either the surface coverage of the prostate on the slide or obstruct the view of the microscope objective below.

4.3 The Servo Motor

After considering these sensor schemes and determining that they would not provide a viable solution, it was decided to change the overall structure of the APPS. In order to change one of its fundamental movements, a Servo motor was used to replace Stepper Motor 1. Servo motors are direct current (DC) motors which provide positional (angular) feedback. They are typically able to rotate between 0 and 180 degrees and are used to make precise movements in everything from industrial milling machine position to gripper control on hobby robot projects. Servo motors are given an external command which causes an encoder to read the position directed by the external command as compared to the current position of the motor. If these two positions are not the same, the

encoder will generate an error code causing the servo motor to rotate in a certain direction until the motor's current position matches the target position at which point the error signal will go to zero.

The ability for the servo motor to create this “error” code offered a promising method of feedback for the APPS. Servo motors move efficiently, therefore while the motor is “out” of position (the external command position does not match current position), the motor will draw more power from the voltage source and increase the torque in the motor. By increasing the torque, if the motor position is considered far from the desired end position, the motor will increase its rotations per minute (RPM) and spin faster until it reaches the desired position. During this time of increased rotational speed, it is possible to monitor the signal created by the uptake of voltage by the motor. The extra voltage which is used by the motor must be funneled through the circuit powering the motor and into the ground. If the ground is also connected to an analog pin on a microcontroller, the residual voltage may be read as an analog signal which spikes whenever extra torque is applied to the motor by itself. It was then realized that the pressure of the prostate being pushed onto the glass would then provide resistance to the servo motor reaching its desired position, in turn causing the servo to draw more current from the power source and provide the residual signal caused by the increased voltage. By creating an Arduino script which recorded the analog voltage readings, the script could detect a threshold of voltage which meant that the prostate was pressed against the microscope slide.

The first servo which was tested was a small Adafruit 2941 9g servo. It is very small and produces only 9 grams*cm of torque. This motor was used to attempt to prove the concept that the residual voltage signal could be read and cause the motor stop after it

had been manually stalled. In order to manually stall the motor, we would physically hold the “propeller” of the servo as it attempted to rotate to its desired position. As we experimented with the rotations of the micro servo, we realized quickly that the 180 degree rotation limit of the micro servo would not serve the purpose of raising and lowering the prostate. The 360 servos function differently from their 180 degree (non-continuous servo) counterparts. When a non-continuous servo is given a command to move, it is given an angular input. Depending on the current position of the servo, it will then either rotate to the desired angle or stay in place. A continuous servo motor can offer the same angular control, but are not typically used for that function. The continuous servos are given an “angular input” but instead of turning to the angle which was given, the servo simply rotates continuously in the direction which the angle implies. This is controlled by the feedback mechanism within the continuous servo motors. An angle below a certain threshold between 0 and 180, typically around 90 degrees, will correspond to counter-clockwise rotation while an angle above the threshold will correspond to clockwise rotations. With this in mind, a Tower MG995 continuous rotation servo was then purchased and tested in the same manner. Whether it was due to manufacturer or user error, we were unable to command the MG995 to rotate continuously at any voltage input. Finally, the Parallax 360 Feedback servo was purchased and chosen as the final servo. This servo offers 2.2 kg per cm of torque and is therefore a much more powerful servo than the motors which were tried before.

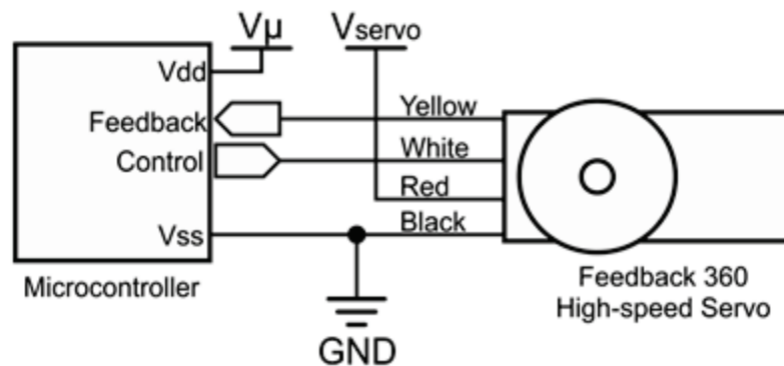


Figure 4.3: A wiring schematic of the Parallax 360 Feedback Continuous Servo [31]. V_{servo} is between 6 and 9 V and must be obtained from an outside source as the Arduino is not capable of providing more than 5 V. The white control wire is attached to digital pin 9 on the Arduino.

The Parallax 360 was programmed to rotate for a certain period of time and was confirmed to stop once the desired amount of time expired. Next, the motor was placed in a small circuit with the Arduino as shown in Figure 4.3. The experimental setup was the same, connect the motor to a power source and have a wire which led through two 10 ohm resistors in parallel, providing 5 ohms total, and into analog pin 0 (A0) on the Arduino. The residual voltage values would be read in through the serial monitor on the Arduino and then the script would run a while loop as the servo turned. While the loop was running, the script would continually check the values as compared to an experimentally determined voltage threshold of 0.07 volts. If the voltage draw by the motor exceeded 0.07 volts due to stalling, the motor would stop rotating. Through the manual stalling method, we were able to consistently stop the motor based on reading the feedback of the voltage draw. This meant that a viable solution had been found to solve the fundamental problem of automation for the APPS, the ability for the system to regulate the lowering and raising of a resected prostate, independent of size with no measurements required.

4.4. Integration of the servo motor into the APPS

After this goal was achieved, the next step was to begin integrating the servo motor and orchestrating the other necessary functions of the APPS. The three governing movements which would need to be achieved were raising the prostate clear of the microscope slide, rotating the prostate by a predetermined number of degrees, then lowering the prostate until it made flush contact with the microscope slide. It was quickly realized that the same mechanism for stopping the APPS once it reached the microscope slide, could be applied to detect when the system reached the top of the tower. This meant that we could simply break the raising and lowering script in half, separated by the rotational period. In order to do this, the Arduino had to be triggered by some form of signal to understand that raising had been completed and rotation of the specimen could begin. Digital triggers were used to serve this purpose.

The digital trigger used was a hard-coded signal which once the raising of the specimen had completed, the Arduino would read a one second delay function. Next, the `digitalwrite()` function would cause a digital pin to read “high” (5 volts in the pin) manually. The script would then ask the Arduino to digitally read the signal of the pin and determine whether it was high or low. Since it was hard-coded to be high, a conditional statement would then allow the Arduino to command stepper motor 2 to rotate the dowel if the pin read high. The pin would then be turned back to low by the hardcoded digital trigger (3.3 volts in the pin). This process is shown in figure 4.4.

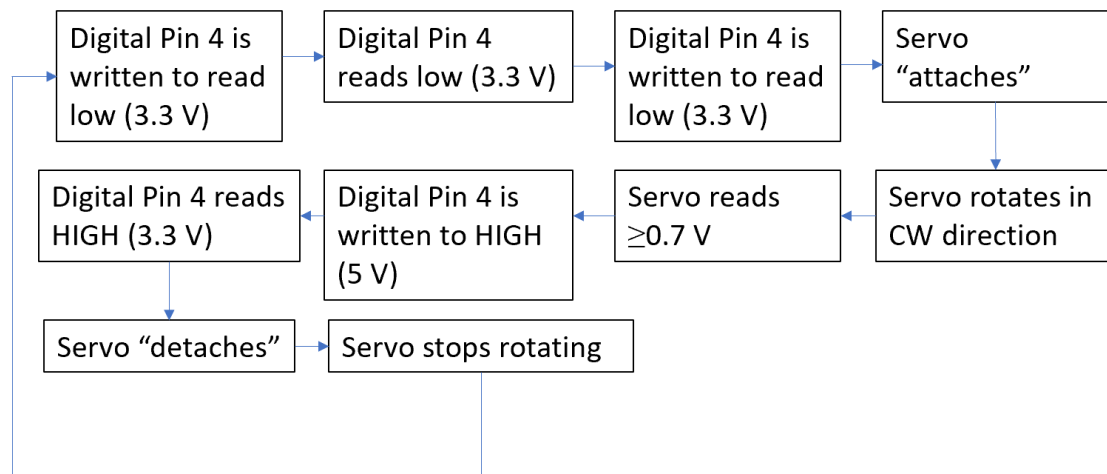


Figure 4.4: A flow chart of the order of operations of using the digital trigger for the raise function in Arduino.

Originally delays were used in between “attaching” and “detaching the servo.

This system of using manual digital triggers worked well initially, however the delays were causing the script to read out of sync. This meant that sometimes the stepper motor would rotate while the servo motor was still in rotation as well. While in theory this could practically save time, the behavior was unpredictable and was not completing the order of operations we were intending to execute. To combat this, we then began to use digital triggers to signal the ending of each operation and begin the next operation. At this point, the basic software commands running the APPS were prepared for automation but there were several hardware changes which needed to occur.

4.4 Second and Third Hardware Updates

The original APPS system utilized a custom-tapped bore made of plastic which, while cost-effective, was labor intensive to recreate. In order to make the hardware more uniform and reliable, 3/8” – 16 thread 4 inch long aluminum rods were purchased to serve as the bore. The downside of making the switch from the custom-tapped and threaded

plastic bores were that the old bores fit directly on to the rotating portion of stepper motor 1. In order to fit onto the Parallax 360, the bore would need to connect to the small toothed adapter which rotated on the outside of the servo. In order to achieve this, an adapter was designed. The servo comes with what are called propeller attachments, small plastic pieces which can fit into toothed portion of the servo and better show the rotation of the servo or allow for attachment to other devices. We used the circular propeller attachment and super glued it to a stack of custom laser cut acrylic pieces. These pieces had a hexagonal hole cut in the middle of them which was sized to exactly fit #16 machining hex nuts. A #16 hex nut was then screwed onto the top of one of the threaded aluminum rods and fixed in place using the adhering epoxy glue Thread Lock, which is used to adhere threaded metal machining parts together. The propeller attachment adapter was then bolted to the servo using a screw. This completed the second hardware update for the new APPS.

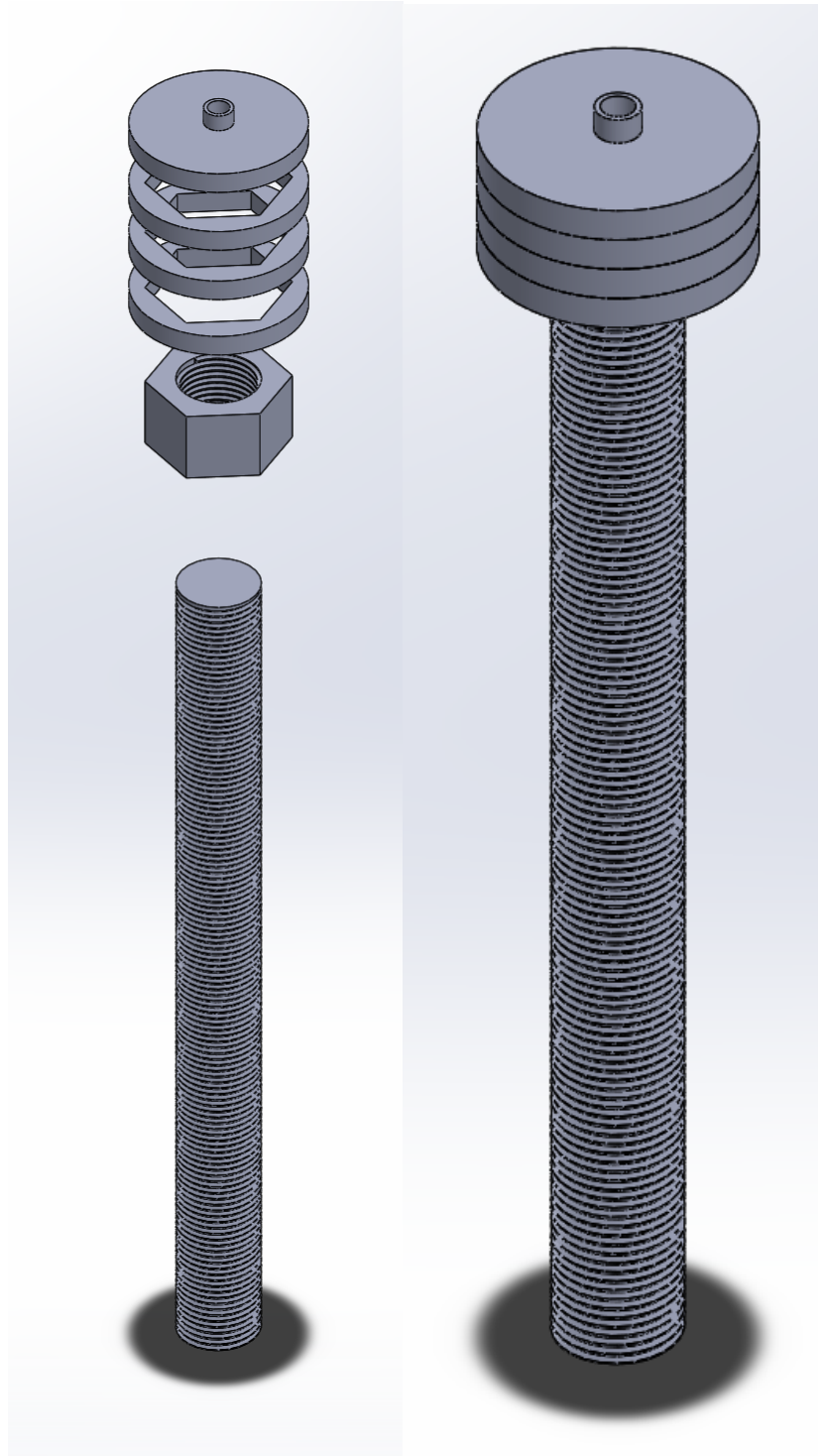


Figure 4.5: The image on the right shows the full assembly of the propeller adapter to turn the bore, the propeller being the top piece. The image on the left shows an exploded view of the assembly with the pieces not glued together.

The older method of manual manipulation of the prostate's position relied on user feedback and visually looking to see whether the desired amount of surface contact had been achieved. This meant that below a certain point, stepper motor 1 would continue to turn but the prostate would no longer be lowered, which was enabled by the 3D printed hex nut housing lowering below the bearing housing. This method would not be able to work for the new signaling method of the APPS since the motor required the stalling created by the pressure of the prostate against the microscope slide. In order to fix this problem, a second hex nut and 3D printed housing were added in series above the bearing housing and lower hex nut and nut housing as shown in figure 4.6 below. This system of dual hex nuts above and below the bearing housing would provide pressure on the specimen as it was lowered to the plate, ensuring flush contact as well as the necessary pressure to stall the servo motor. This sets a low voltage threshold on the motor stall signal to avoid applying too much pressure and damaging the surface of the prostate. This concluded the third hardware update for the APPS.

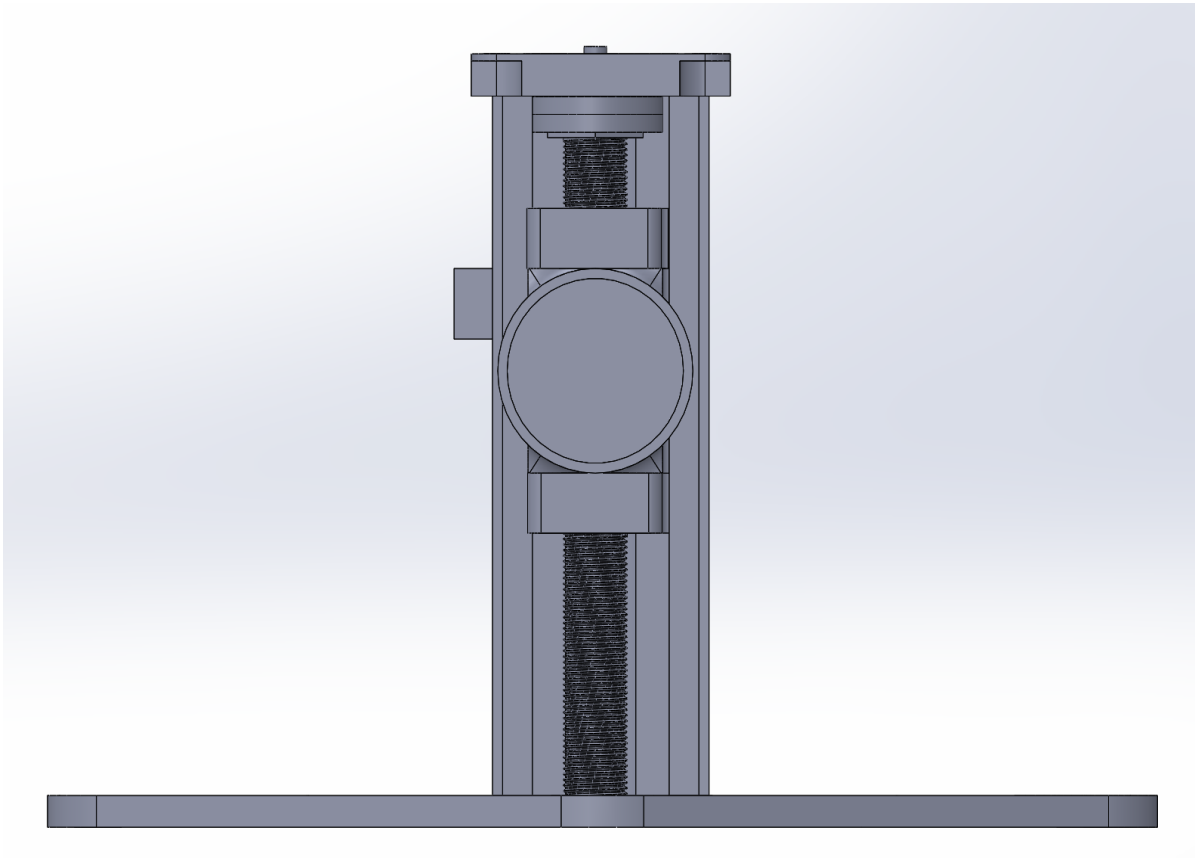


Figure 4.6: A SolidWorks rendering of the tower utilizing the two hex nut system.

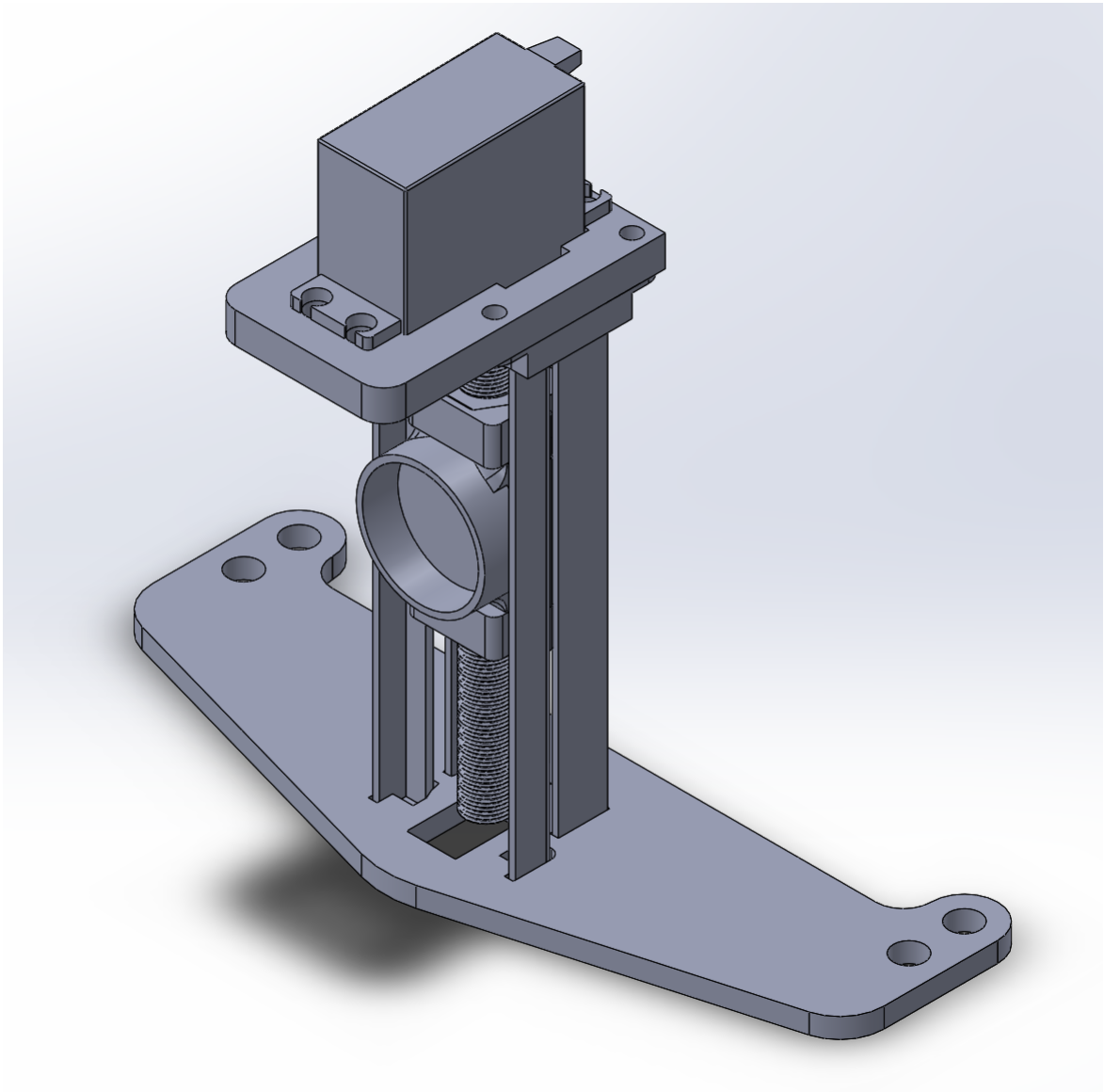


Figure 4.7: The updated tower of the APPS, with Servo adapter, dual hex nut system, tower height of 4 inches, and the Parallax Feedback 360 Continuous Servo at the top.

4.6 Integration into LabVIEW and Pivot to MATLAB

The VR SIM system is controlled by the National Instruments program LabVIEW 2014. LabVIEW is a graphical programming language which allows the user to perform tasks within a wide range of virtual instruments (VI) as well as interface with supported hardware. In our custom VR-SIM setup, LabVIEW currently controls the stage which the APPS is mounted on, the camera, the spatial light modulator (SLM), and the laser which

is used to illuminate the object which is being imaged. In order for the APPS to become fully automated, it would require the APPS to interface with LabVIEW in order to integrate it with imaging software. In order for the APPS to interface with LabVIEW, serial commands would need to be sent from LabVIEW to the Arduino. LabVIEW offers support software for the Arduino, however the supported software does not offer pulse width modulation. In order to precisely control the speed and direction the servo rotates, it is preferred to use the pulse width modulation `writeMicroseconds()` command rather than the `servo.Write()` command in Arduino. In order to solve this issue, the controlling software for the APPS system was changed to MATLAB. MATLAB also offers support software for the Arduino and has the ability to control several motors at the same time. In addition, it offers the ability to be incorporated inside of a LabVIEW Virtual Instrument (VI) using the “MATLAB Script Node” sub-VI. In order to interface with MATLAB, an Adafruit Motorshield V2 was mounted on to the Arduino circuit.

MATLAB uploads a command server to the Arduino board which gives it control over all the functions of the Arduino. Then, MATLAB asks the user to create an object for the kind of hardware they are controlling with the Arduino. In this case, MATLAB takes the minimum and maximum pulse width durations for the servo, 700 and 2300 microseconds respectively, and converts the limits of these durations to a 0 to 1 scale. 0 is the minimum “angle” which the servo may rotate to and 1 is the maximum “angle”, where 0.48 to 0.52 is considered the dead-bandwidth where the servo will not turn. Therefore, from 0 to ~ 0.48 , the servo will rotate counter-clockwise and from ~ 0.52 to 1 will rotate clockwise (approximations are used as these values may vary slightly based on the hardware used). To avoid the dead-bandwidth, the scripts use a for loop counting from 0

to 0.4 by the thousandth, and 0.6 to 1 by the thousandth in order to control the servo. One benefit of using MATLAB in order to control the APPS through the Arduino is that MATLAB has a built in function to read voltages from the analog pin of an Arduino, called `readVoltage()`. This method requires no arithmetic manipulation of serial values collected from the analog pin as was necessary for the Arduino script. The output of the `readVoltage` function can be printed to the command window and allow the user to monitor the fluctuations in voltage as the APPS is running. This allowed for a precise method of determining the thresholds that signal the APPS to stop.

Another benefit of changing from Arduino to MATLAB as the governing software is that LabVIEW and MATLAB are easier to integrate into one software control application. LabVIEW allows the user to create script nodes, which can either contain text-based coded programming instructions within LabVIEW or call on MATLAB to execute MATLAB programs. LabVIEW then becomes a virtual controller of MATLAB programs, which in turn are controlling the Arduino which controls the APPS. Another benefit of changing the software is that in Arduino scripts the entire sketch is looped, causing the timing of executing commands strictly to become difficult. In MATLAB, the script runs once and each command is completed before moving on to the next, making it simple to execute each of the time-sensitive commands to completion before moving on to the next.

Incorporation of the operating scripts for the APPS into LabVIEW was simple. LabVIEW's order of operations, since it is typically not text based, is controlled by "wires" which transfer data or instructions between individual codebases called sub-VI's, which compiles and checks for errors throughout the code which was written. In order to integrate the APPS, a script node was placed in front of the sub-VI which controls the collection of

images from the microscope. This script node would contain the “down” function, causing the servo to spin counter-clockwise until the voltage threshold was met, indicating that the prostate was in place for imaging. The imaging would then commence. Following the completion of the imaging script, a second script node was placed after the imaging sub-VI had completed and the X-Y microscope stage has reset to its initial position. The second script would contain the “raise” and “rotate” functions, causing the servo to rotate clockwise until the specimen has reached the max height of the tower, then stepper motor 2 is told to rotate 200 steps which corresponds to a true 36 degree rotation. These two sets of commands are nested within a 10-iteration loop. This 10-iteration loop allows LabVIEW to fully complete the task of imaging the full decagonal circumference of the prostate specimen. Therefore, in terms of user input, the user mounts the sample onto the APPS, provides input on the desired size of each image panel and the number of rotations to obtain, and with one software command, commences the entire process. After starting the acquisition in LabVIEW, no further user input is required, and the APPS combined with the VR-SIM system acquires and delivers images of the entire tissue circumference. This process is shown graphically in figure 4.8. With no dimensional measurement inputs required, the APPS has now passed the test of automation.

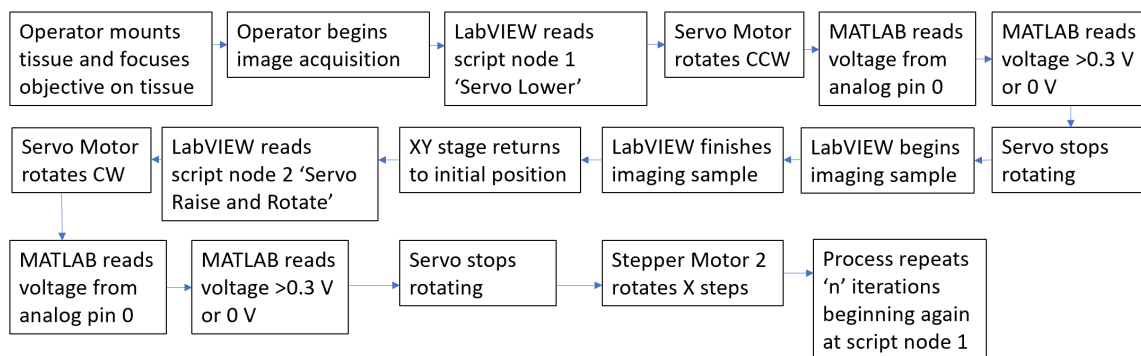


Figure 4.8: A flow chart of the order of operations for image acquisition using the automatic APPS Generation 2.

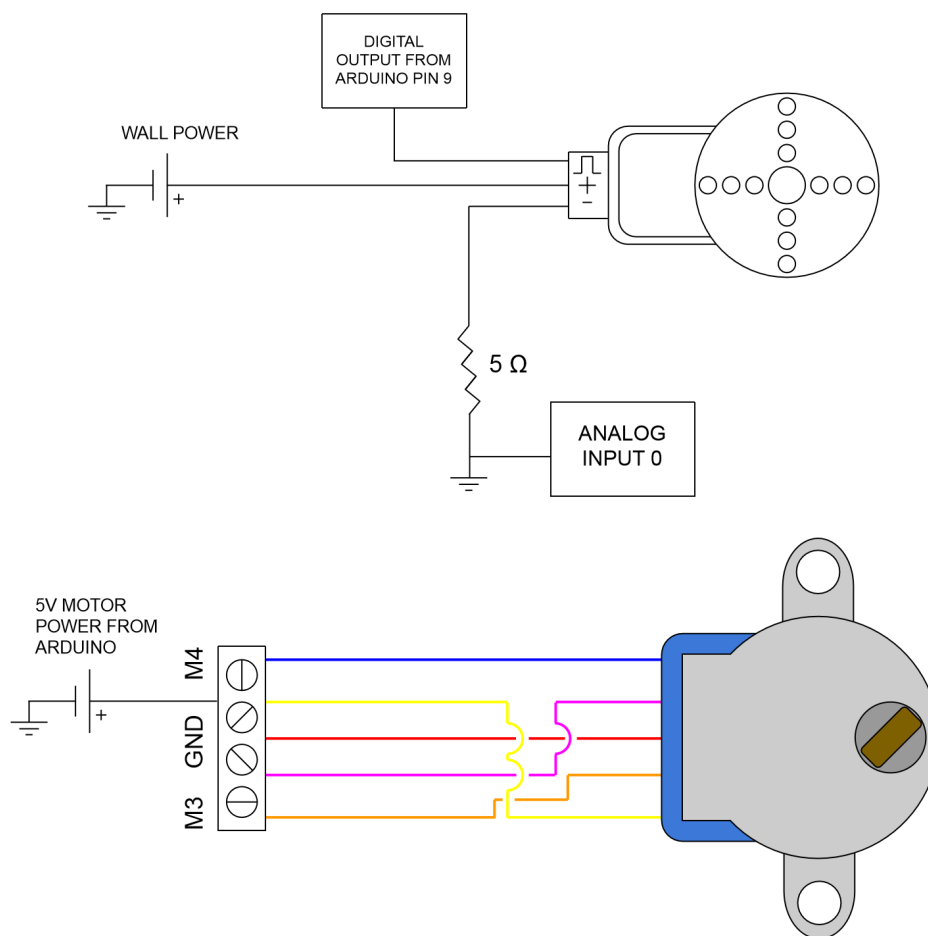


Figure 4.9: Final wiring schematic of APPS Generation 2. Wall Power varies from 6-9 V.

5. Bench Validation Experiments for the APPS Generation 2

The Automated Prostate Positioning System now lives up to its name i.e. it is fully automatic after the press of one button. However, now that the system is fully automatic, it must be proven to function in a manner which is similar or better than the previous configuration. In order to validate the new configuration several experiments were run. As stated in the introduction, the functional requirements of this system are that the system completes imaging automatically, accurately, and repeatedly. Automation has been proven through the completion of the LabVIEW code, the MATLAB code, and the implementation of the analog servo voltage feedback circuit.

5.1 Experiment 1 Speed Testing of the APPS Generation 2

In order to understand how fast the new design of the APPS is able to acquire images, including the manipulation of the sample, a small experiment was run aiming to complete a ten panel image acquisition of 2x2 panels. This would allow for easy calculations of the per frame imaging time, giving the operator a rough estimate of how long the entire imaging process will take.

5.1.1 Materials and Methods

A 3 cm x 3 cm cube of bovine muscle obtained from a local supermarket was cut from boneless eye of round chuck to mimic the shape of a small prostate. This tissue was then stained for 3 minutes in 100 mL of TOPRO 3 and phosphate buffered saline solution (PBS) mixture to stain for cell nuclei. The tissue was then removed and rinsed in PBS then dried. After this, the tissue was covered with 0.002% Acidic Acridine Orange and left to

sit for 30 seconds. The tissue was then rinsed again in PBS, dried, then the wooden dowel was placed through the center and subsequently mounted onto the APPS.

The tissue was then lowered to the glass microscope slide so that the system could be manually focused on the tissue specimen after it was lowered by the initial function of the LabVIEW script. The tissue was then raised and the required LabVIEW inputs were added. Several inputs are necessary to complete imaging currently, the first being the frequency of the pattern that the operator wants to use, which in this case was 36 pixel pitch with a 45 ms camera exposure time. Next, the laser power output must be adjusted for each wavelength, 30% was used for the 470 nm laser and 90% was used for the 640 nm laser. Then, the operator must create a folder in which the data is saved in the computer (data was written onto an internal solid-state drive for speed). The LabVIEW code names the panel by simply adding the iteration of the loop in which the panel is being taken, i.e. the first panel reads Panel_1, the second reads Panel_2 etc. Lastly, the operator must decide whether to use autofocus or not. For this experiment, one test was run with autofocus, the second was not to gain an understanding of the base speed of the system as well as a more realistic speed including autofocus. An external stopwatch was used to time the entire operation after the start button was pressed and ending when the imaging stage returned to its original position.

5.1.2 Results

The timed results of this experiment for using autofocus and not using autofocus were 6 minutes and 28.82 seconds and 5 minutes and 44.76 seconds, respectively. In order to understand the frame by frame acquisition time, the total time elapsed must be divided

by 10 to separate the time for each panel, then divided by 4 since a total of 4 images were taken per panel (2x2).

$$\frac{\text{Total Imaging Time (in seconds)} - \text{Automation Time}}{\text{Number of Panels} * \text{Number of Images per Panel}}$$

Calculating mean running times for each function of the APPS, automation time is approximately 19.305 seconds per panel. That gives an image acquisition time for a SIM frame of 4.89 seconds using autofocus and 3.79 seconds without. However, these figures incorporate the APPS automation time, which does not scale with the number of images collected for each panel (the automation time is constant for each rotation). The theoretical rate for frame acquisition based on 40 ms exposure of each laser is $6 * 40 \text{ ms} = 240 \text{ ms}$ imaging time per frame. (Including autofocus in this calculation this time would slow the imaging time by $n * 40 \text{ ms}$ for each frame, depending on the number of frames n needed to find focus). Considering a typical 20x20 image grid per panel for the image acquisition of prostatectomy specimen for margin analysis, the optimized APPS would be able to complete imaging in approximately 19 minutes, including APPS automation, without autofocus. This is faster than the previously reported imaging time of the APPS Generation 1, which was approximately 36 minutes [40], this would be the theoretical fastest imaging time possible for the APPS Generation 2. Including ~20% factor of safety for autofocus imaging time (1-2 autofocus frames per location), the APPS Generation 2 would complete a ten panel 20x20 image acquisition in 24.55 minutes, which is still faster than the previous version. However, in order to pseudo-color the images acquired by the VR-SIM APPS system to appear similar to gold standard H&E pathology, the dual stain method is used and requires two excitation wavelengths. The prior iteration of the APPS has been used for

clinical studies as shown in chapter 3 and the typical time taken for the full image acquisition of a prostatectomy study was approximately 2 hours. Therefore, the acquisition rate of the new APPS is nearly six times as fast as the prior iteration while implementing the dual laser exposure and manual control of the system.

5.2 Experiment 2 Ten Panel Rotation without imaging

To test the accuracy of the voltage feedback circuit the APPS was used for a small sample experiment using a simple “meat” tissue (boneless eye of round roast) with no staining. To prove success in accuracy, the goal is to complete a ten-panel manipulation of the specimen multiple times, running the APPS automatically so that is using the sensor to start and stop. This test was then run three times in order to judge the completion of the automatic sensing. The APPS must be able to accurately raise, lower, and rotate the prostate ten times in order to be considered an accurate method of sensing.

5.2.1. Materials and Methods

A 4 cm x 4 cm section of bovine muscle tissue was cut to act as a substitute for a prostate. For the first trial, the tissue was not mounted on the system and the servo tower was left to act freely. This was used as a control trial against the other two trials. The second and third trials were run with the specimen substitute mounted on the system using the wooden dowel rod. For all of these trials, the original MATLAB code was run instead of the LabVIEW to better analyze each functions operation.

5.2.2 Results

Trial 1

Panel Number	Function	Max (V)	Min (V)	Mean (V)	Std. Dev. (V)	Sample	Time (S)	Threshold or 0 V?
--------------	----------	---------	---------	----------	---------------	--------	----------	-------------------

1	Raise	0.14174	0	0.0827	0.013724	146	10.838	0
	Lower	0.25415	0	0.069343	0.022717	128	9.2652	0
2	Raise	0.32972	0.034213	0.072554	0.016976	148	10.07	Threshold
	Lower	0.343	0.028	0.1018	0.02245	165	9.54	Threshold
3	Raise	0.44174	0	0.069832	0.013326	146	10.813	Threshold
	Lower ^A	0.14174	0	0.07087	0.1	2	0.3016	0 (Fail)
4	Raise	0.3365	0.04506	0.0875	0.01649	152	10.43	Threshold
	Lower ^B	0.26393	0	0.033604	0.076469	401	27.316	0 (Fail)
5	Raise	0.15467	0	0.075648	0.01563	154	10.69	0
	Lower	0.276	0	0.09103	0.01254	149	9.354	0
6	Raise	0.3456	0.0308	0.07897	0.020037	151	9.987	Threshold
	Lower	0.28351	0	0.10023	0.01454	162	9.401	0
7	Raise	0.1562	0	0.0913	0.021465	147	9.87	0
	Lower	0.2689	0	0.08917	0.015643	162	10.31	0
8	Raise	0.1365	0	0.093462	0.019087	145	10.02	0
	Lower	0.3215	0.0256	0.1065	0.02543	158	9.476	Threshold
9	Raise	0.1946	0	0.0879	0.01756	154	10.34	0
	Lower	0.21354	0	0.07954	0.02043	149	10.11	0
10	Raise	0.3789	0.0314	0.1106	0.0205	158	10.89	Threshold
	Lower ^C	0.24438	0	0.089606	0.13459	3	1.139	0 (Fail)

Table 5.1: Table of descriptive statistics of each of the raising and lowering functions of Trial 1 detailing: Maximum Voltage (V), Minimum Voltage (V), Mean Operating Voltage (V), Standard Deviation of the operating voltages (V), the number of samples taken, and the Time taken for each function to complete (s).

Trial 2

Panel Number	Function	Max (V)	Min (V)	Mean (V)	Std. Dev. (V)	Time (S)	Samples Taken	Threshold or 0 V?
1	Raise	0.2297	0	0.09506	0.02049	10.47	136	0
	Lower	0.2786	0	0.09641	0.02583	10.06	138	0
2	Raise	0.179	0	0.108	0.0192	10.01	246	0
	Lower	0.3541	0.0394	0.1007	0.01744	9.467	242	Threshold
3	Raise	0.2397	0	0.1063	0.02001	9.91	270	0
	Lower	0.312	0.02933	0.1056	0.02935	9.341	251	Threshold
4	Raise	0.1978	0	0.1073	0.01824	9.997	255	0
	Lower	0.305	0.0197	0.1025	0.02327	9.204	248	Threshold
5	Raise	0.2645	0	0.1075	0.02172	9.861	254	0
	Lower	0.3444	0.01853	0.1102	0.01908	9.273	218	Threshold
6	Raise	0.183	0	0.1097	0.03006	9.901	239	0
	Lower	0.3079	0.04231	0.1101	0.0201	9.41	237	Threshold
7	Raise	0.312	0.043	0.1103	0.02412	9.869	254	Threshold
	Lower	0.347	0.02715	0.1038	0.03003	9.103	268	Threshold
8	Raise	0.1834	0	0.1116	0.03010	10.01	249	0

	Lower	0.3652	0.0205	0.10354	0.01998	9.321	231	Threshold
9	Raise	0.1757	0	0.1255	0.02192	10.08	270	0
	Lower	0.3376	0.01887	0.1103	0.02078	9.45	257	Threshold
10	Raise	0.2915	0	0.09087	0.02176	9.999	258	0
	Lower	0.3215	0.03056	0.1064	0.01909	9.307	234	Threshold

Table 5.2: Table of descriptive statistics of each of the raising and lowering functions of Trial 2 detailing: Maximum Voltage (V), Minimum Voltage (V), Mean Operating Voltage (V), Standard Deviation of the operating voltages (V), the number of samples taken, and the Time taken for each function to complete (s).

Trial 3

Panel Number	Function	Max (V)	Min (V)	Mean (V)	Std. Dev. (V)	Time (S)	Samples Taken	Threshold or 0 V?
1	Raise	0.1841	0	0.1063	0.01231	10.17	255	0
	Lower	0.3564	0.03111	0.1204	0.02639	9.562	241	Threshold
2	Raise	0.415	0.02405	0.1018	0.0152	9.978	259	Threshold
	Lower ^D	0.4594	0.08798	0.2737	0.2627	0.2067	2	Threshold (Fail)
3	Raise	0.2341	0	0.1105	0.02161	9.949	262	0
	Lower	0.341	0.03021	0.1204	0.01956	9.251	248	Threshold
4	Raise	0.2157	0	0.1301	0.01917	9.967	250	0
	Lower	0.3591	0.01872	0.1010	0.02122	9.349	251	Threshold
5	Raise	0.2997	0	0.1175	0.02394	10.02	238	0
	Lower	0.3113	0.01337	0.1046	0.02871	9.363	228	Threshold
6	Raise	0.2818	0	0.1008	0.02562	9.807	246	0
	Lower	0.3193	0.04576	0.1201	0.01971	9.195	229	Threshold
7	Raise	0.2837	0	0.1056	0.03009	9.992	259	0
	Lower	0.368	0.02827	0.1067	0.02501	9.478	241	Threshold
8	Raise	0.1765	0	0.0908	0.01077	9.895	245	0
	Lower	0.3413	0.06672	0.1164	0.02715	9.422	236	Threshold
9	Raise	0.2765	0	0.1004	0.01983	10.42	257	0
	Lower	0.2991	0	0.1003	0.0305	9.451	253	0
10	Raise	0.1873	0	0.1076	0.02504	9.989	258	0
	Lower	0.3247	0.04012	0.1109	0.03006	9.348	239	Threshold

Table 5.3: Table of descriptive statistics of each of the raising and lowering functions of Trial 3 detailing: Maximum Voltage (V), Minimum Voltage (V), Mean Operating Voltage (V), Standard Deviation of the operating voltages (V), the number of samples taken, and the Time taken for each function to complete (s).

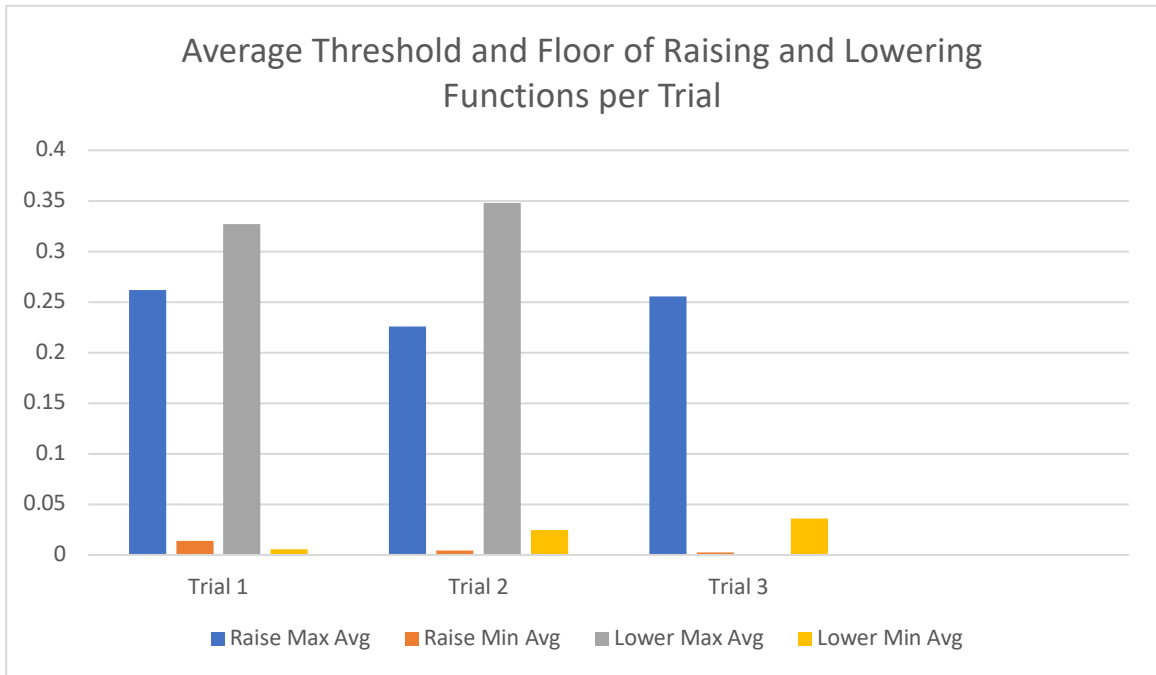


Figure 5.1: Graphical representation of the average voltage threshold and floor for each function per trial.

5.2.3 Discussion

Each trial has a total of 20 functions run, 10 raises and 10 lowers. Therefore, 60 total functions were included in this experiment. The data of each function marking the maximum voltage drawn, the minimum voltage drawn, the mean operating voltage draw, the standard deviation, the time it took to complete, the number of samples taken, and whether the sensor stopped by reaching the threshold of voltage draw or stalled to 0 volts are displayed for each trial above.

In this experiment testing for the accuracy of the APPS voltage feedback circuit as a sensor, 56/60 functions were completed in full giving it a 93.33% success rate. There were 4 instances in which the APPS was unable to properly complete a function and each of them come from the same problem. The function is marked for each occurrence with a

superscript of A-D, but they come from Trial 1 Panel 3 Lower, Panel 4 Lower, and Panel 10 Lower, as well as Trial 3 Panel 2 Lower. Notice what each of these operations have in common: they are all lower functions. This led to the finding of a small design flaw in the dual hex nut system. It is possible to see that the Raise function which occurred before each of the Lower failures all ended by reaching the voltage threshold, which is atypical considering the majority of raising functions ended by stalling to 0 V (88.3%). The flaw in the dual hex nut system is that the hex nut which is housed above the bearing housing can sometimes get stuck in the thread lock and become too tightly wound with the hex nut which is immobilized at the top of the bore. This causes one of several things to occur, each showcased by the Voltage vs. Sample graphs below. In Figure A, the servo motor stalls after 0.3 seconds causing it to read a voltage of 0 and shut off. In figure B, the two hex nuts are too tight for the servo to move and therefore cause the servo to pulse through its entire angular cycle as shown by the collection of 400 samples (0:0.001:0.4 gives 400 samples). In figure C, a similar process to A occurs where the motor stalls to zero before it can attempt to draw more power again. Lastly, figure D shows the servo attempting a very high voltage-draw to push its way out of its immobilization and therefore breaching the threshold limit and shutting itself off.

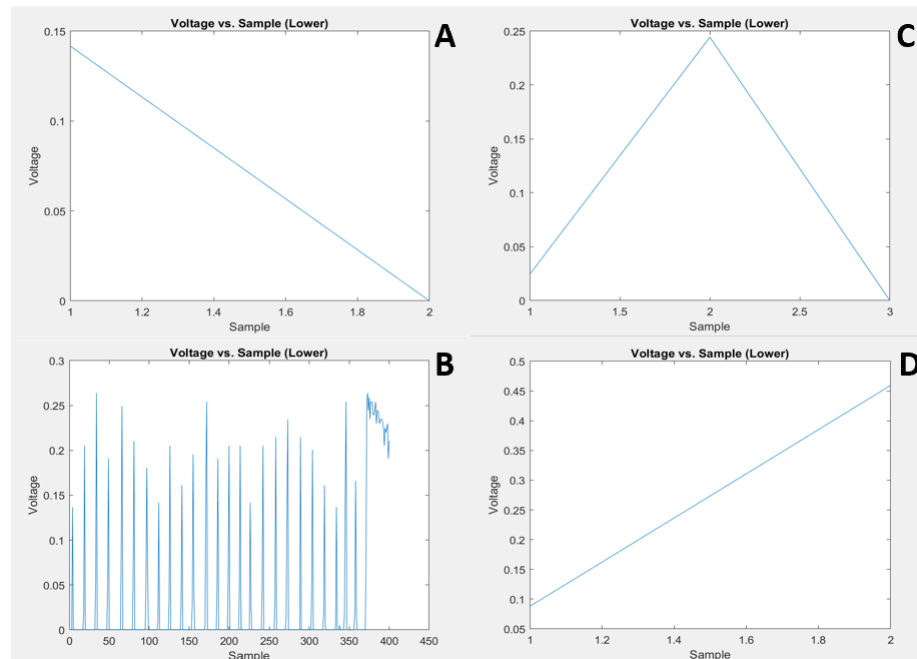


Figure 5.2: A collection of the four outlier functions in which the APPS failed. Figure A depicts the servo motor stalling after only two samples were taken and reaching one of the two trigger values (0V). Figure B shows the servo attempting to work its way out of the locked position but not managing to in the allotted 400 sample time. Figure C shows a similar attempt to figure A and B however after the initial 0.25 V voltage draw the servo “zeroed out.” The term “zeroed out” refers to when the Servo motor has reached its stalling current and can turn no longer, causing it to pulse and wait, giving a zero voltage reading. Figure D shows a large initial voltage draw which resulted in the triggering of the other stopping value, the voltage threshold of 0.3 V.

This problem is considered a small design flaw as it does not totally render the Raise function inadequate. On three separate occasions the system was stopped by the Raise function reaching the threshold voltage limit and the servo was able to successfully lower after. Several hardware or software solutions could be implemented in order to solve this problem. One hardware solution for this issue could be the implementation of a spring which is placed with the bore and hex nut in the center of the coils that extends down towards the dual hex nut system. This would provide added resistance prior to the dual hex nut system reaching the top of the bore and likely would trigger the threshold stopping limit without the hex nuts locking together. A software solution for this problem would be to

rewrite the for loop which collects the sample and take the average of the array of voltageRead values. By doing this, large outliers like 0 V or 0.45 V readings would not trigger the servo to stop rotating and rely more on the motors high torque to successfully unscrew the hex nuts loose.

5.3 Experiment 3 Test of Repeatability with Imaging

The last experiment run was a test of repetition. For the APPS to be successful, it must keep the prostate precisely oriented each time it raises and lowers. To test this ability, the APPS was run through a 10 panel image acquisition, with no rotations. Being able to analyze the APPS's ability to image the same panel 10 times should show the precision of the raising and lowering function by ensuring that the same artifacts can be seen in approximately the same place between panels. It is expected that the APPS will be able to successfully sense and stop to collect the same images each time it makes contact with the slide. In order to ensure that it would be possible to find a structure in each of the ten panels which was the same, braided Nylon string was tied around the center of the tissue subject.

5.3.1 Materials and Methods

For this experiment, a 4 cm x 4 cm portion of chuck boneless rump roast was placed in 100 mL of 200 μ M TOPRO 3 solution mixed with "normal" Phosphate Buffered Saline (PBS pH 7.4). The tissue was left for 3 minutes to soak. The tissue was then removed from the solution and rinsed in normal PBS then dried on a Kim Wipe. The tissue was then sprayed over the entire surface with 0.02% Acidic Acridine Orange solution and allowed to sit for 30 seconds. The tissue was then once again rinsed in PBS briefly and dried with a Kim Wipe. After staining, Nylon string was wrapped around the center of the tissue to serve as an artificial marker.

For imaging, 1 cm x 1 cm images were taken 10 times. The exposure time of the camera was 45 ms using a 36 Hz frequency for the SIM pattern. The 1 cm x 1 cm image allows for 64 images to be taken per panel. The fluorescent stains used were exposed to 640 nm (Topro 3) and 470 nm (AO) at 90% and 35% respectively. The APPS begins in the raised state, which is the same state it ends after the image acquisition process. Therefore, the objective was focused with the tissue lying on the slide and once it was in focus it was placed into the gimbal joint in the bearing housing. 470 nm autofocus was used every 2 steps (every second image) with a step size of 10 microns.

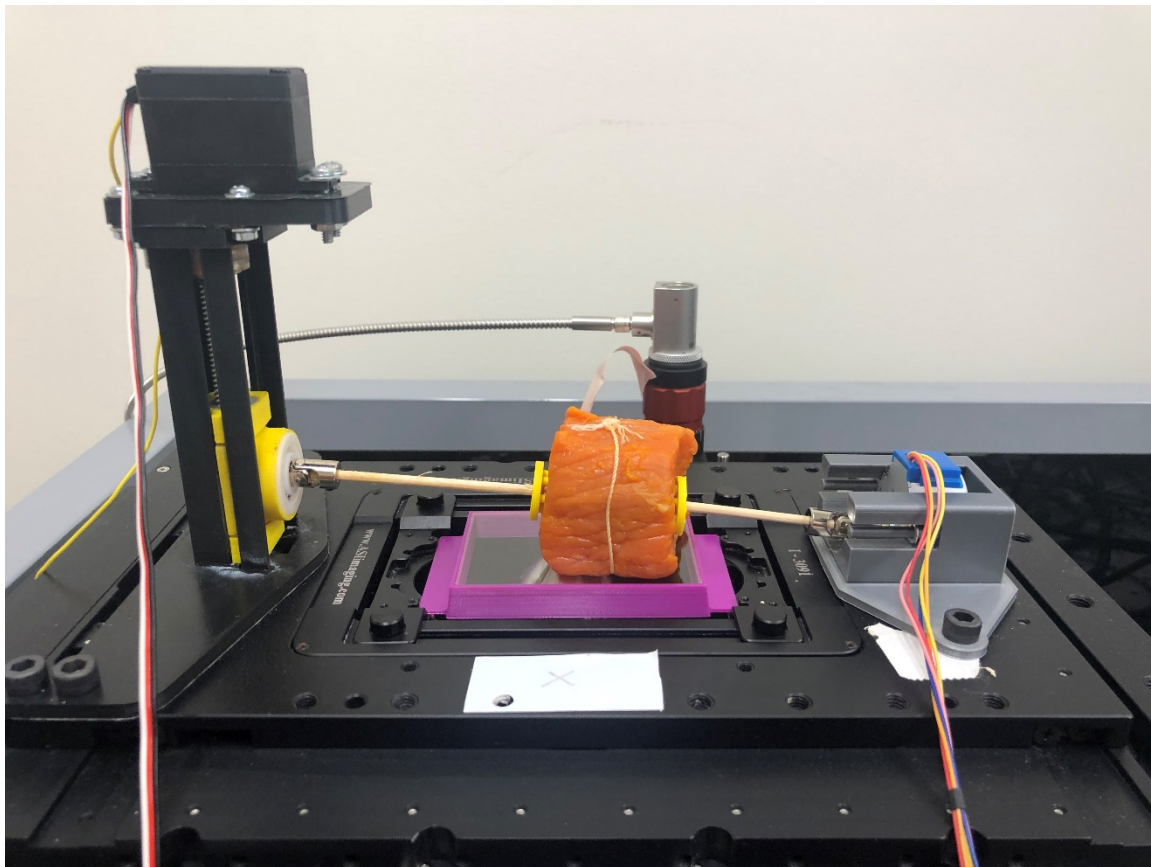


Figure 5.3: The experiment setup of the repetition experiment, Experiment 3. The stained tissue is wrapped in nylon string and raised and lowered ten times, acquiring an 8x8 panel of images in order to test the precision and accuracy of the raising and lowering functions.

5.3.2 Results

The total imaging time of the experiment was 26 minutes and 48 seconds. The timing of this experiment is not completely indicative of full imaging times for a clinical prostate case which will be discussed in chapter 6. The APPS was able to successfully perform 10 raising and lowering functions with no faulters in turns.

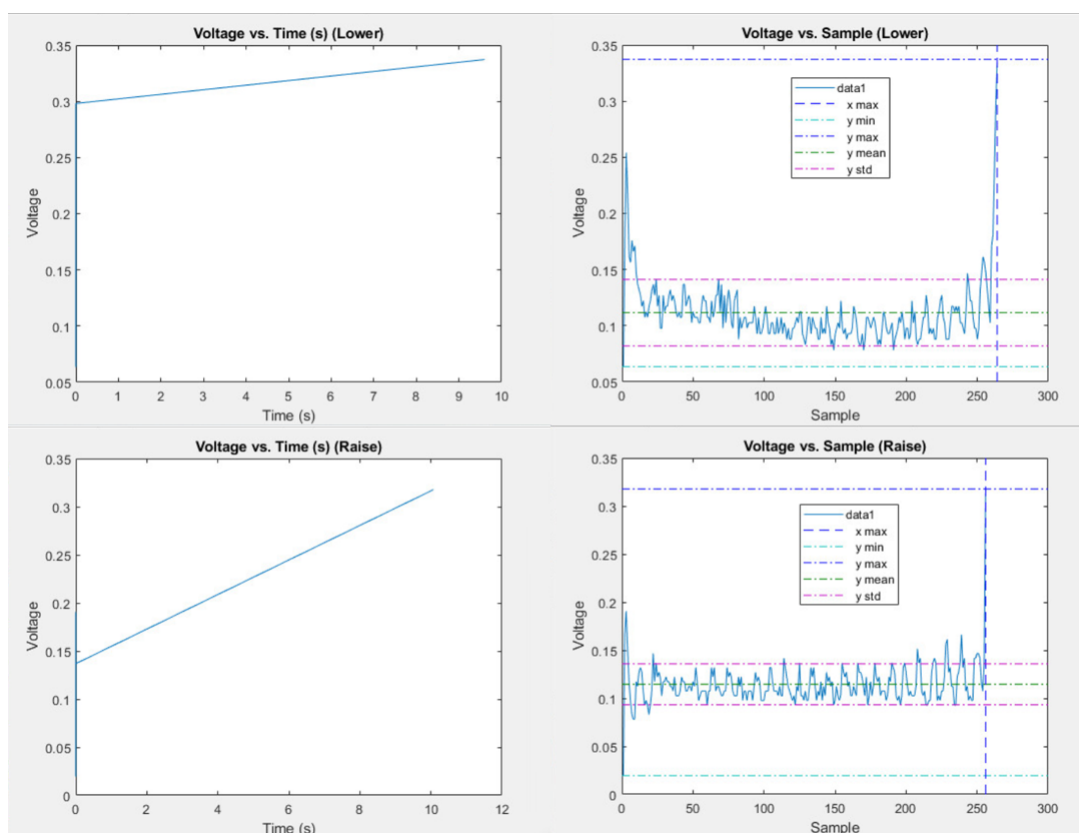


Figure 5.4: Numerical Data collected from Panel 1. There was an average voltage during the raise function of 0.1146 V with a minimum voltage of 0.01955 and a maximum voltage of 0.3177 V. As soon as the voltage peaked above 0.3 volts, the servo motor stops rotating and imaging began. There was an average voltage of 0.1156 V for the lowering function with a maximum voltage draw of 0.3372 V and a minimum voltage draw of 0.06354 V.

Table 2: Full Statistical Data of the 10 Panel Repetition Experiment

Panel Number	Function	Max V	Min V	Mean	Std. Dev.	Time (S)	Samples Taken	Threshold or 0 V?
1	Raise	0.3096	0.01955	0.1146	0.02131	10.07	246	Threshold
	Lower	0.3372	0.06354	0.1156	0.02959	9.604	256	Threshold
2	Raise	0.176	0	0.118	0.01982	10.07	264	0
	Lower	0.3324	0.02933	0.1016	0.02743	9.365	236	Threshold
3	Raise	0.2297	0	0.1075	0.02001	9.887	254	0
	Lower	0.3324	0.02933	0.1026	0.02935	9.353	239	Threshold
4	Raise	0.1955	0	0.1096	0.01904	9.826	246	0
	Lower	0.3079	0.01955	0.1008	0.02492	9.151	230	Threshold
5	Raise	0.2668	0	0.1075	0.02229	9.827	240	0
	Lower	0.3324	0.02933	0.1004	0.03008	9.315	229	Threshold
6	Raise	0.3519	0.02933	0.1105	0.02426	9.796	251	Threshold
	Lower	0.3079	0.03241	0.1011	0.0271	9.369	230	Threshold
7	Raise	0.2933	0	0.1107	0.02379	9.885	254	0
	Lower	0.347	0.03421	0.1015	0.02995	9.469	238	Threshold
8	Raise	0.2933	0	0.1107	0.02379	9.849	258	0
	Lower	0.3324	0.05865	0.1023	0.02715	9.422	236	Threshold
9	Raise	0.2737	0	0.1125	0.02455	9.942	263	0
	Lower	0.347	0.01466	0.1003	0.03	9.309	240	Threshold
10	Raise	0.4008	0.02444	0.1151	0.02925	9.994	262	Threshold
	Lower	0.3177	0.02444	0.105	0.02786	9.547	240	Threshold

Table 5.4: Table of descriptive statistics of each of the raising and lowering functions of Experiment 3 detailing: Maximum Voltage (V), Minimum Voltage (V), Mean Operating Voltage (V), Standard Deviation of the operating voltages (V), the number of samples taken, and the Time taken for each function to complete (s).

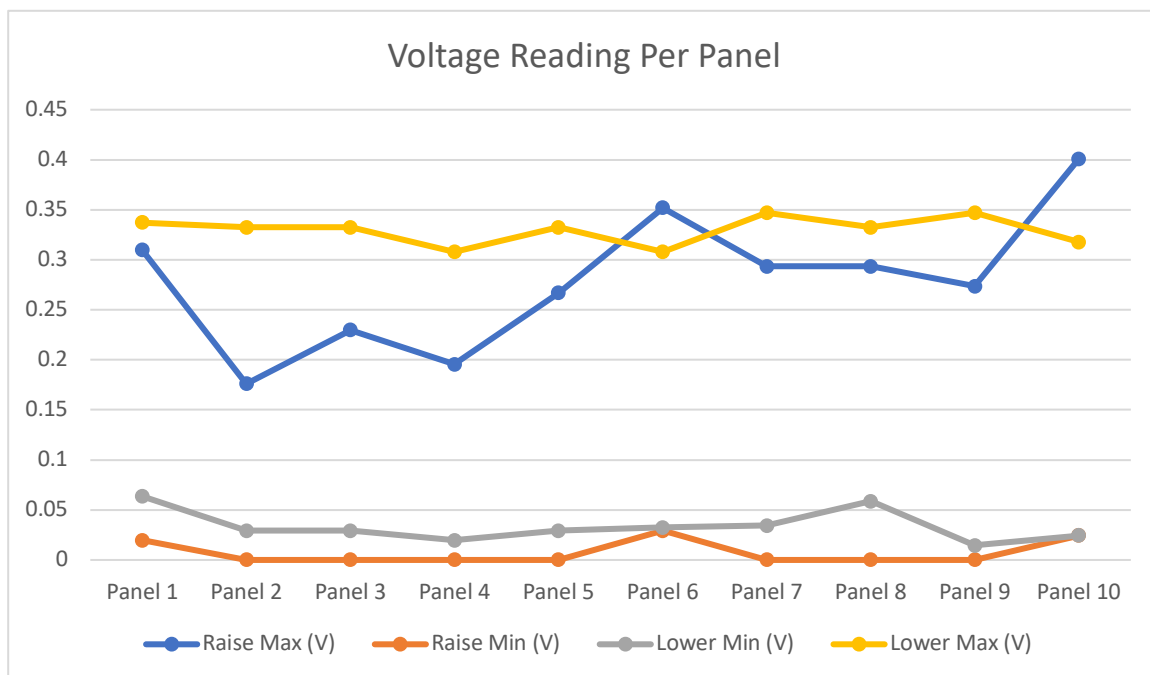


Figure 5.5: Line graph representing the maximum voltage and minimum voltage collected for each panel.

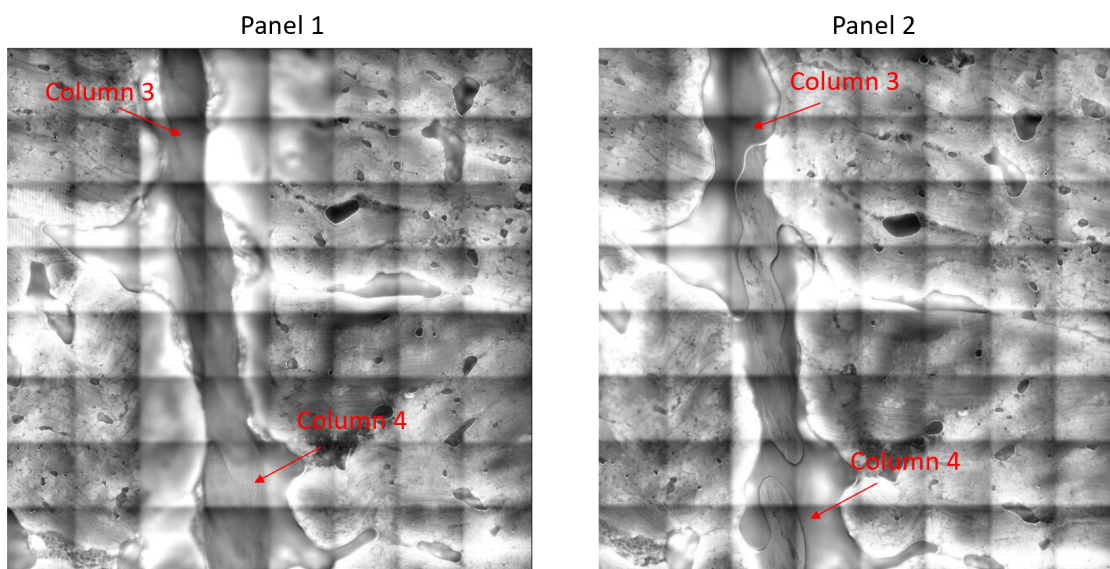


Figure 5.6: Panel 1 and Panel 2 processed for the uniform image of the SIM frame. Panel 1 is pictured on the left and the nylon string can be clearly seen crossing through the third

and fourth column of images taken. Panel 2 is pictured on the right, the nylon string is more in focus and can be seen traversing columns 3 and 4.

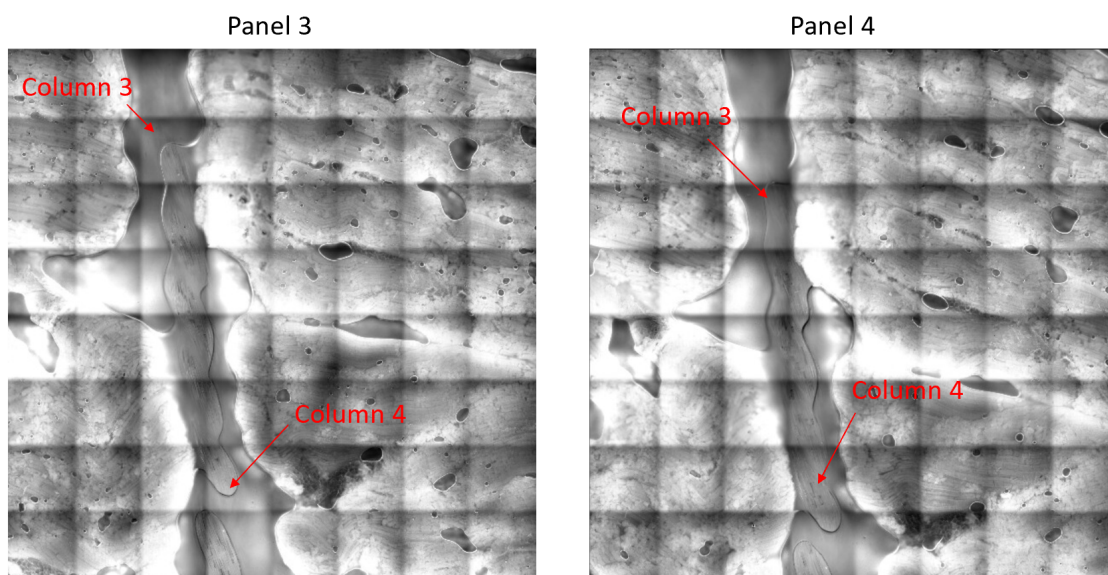


Figure 5.7: Panel 3 and Panel 4 excited at 470 nm processed for the uniform image of the SIM frame.

5.3.3 Discussion

The graphs shown in figure 5.4 represent two sets of data for each function. The first set of data is the voltage draw as a function of the time it takes to complete the raising or lowering function. On average, it takes the raising function 9.912 seconds to complete, and the lowering function takes 9.39 seconds. The second set of data shows the number of “samples” taken. Here, “sample” refers to the method that the APPS using to understand its relative voltage draw. The system functions using a “for” loop where from an increasing angle as explained in chapter 4, the MATLAB code which controls the APPS pauses every 0.01 seconds in order to take a voltage reading using the voltageRead function. The sample is the individual reading making the x axis of these graphs the collection of all the readings. The number of samples taken is dependent on how long it takes for each function to reach either the threshold limit of 0.3 V or to “zero out”. In the majority of cases (>50%) the raise

function tends to “zero out.” This is the result which would be expected considering that the hex nut which is placed over the bearing housing will eventually reach the hex nut which is immobilized at the top of the bore. This will cause the servo to no longer be able to rotate and not allow for voltage to be drawn. Conversely, the lowering function nearly never “zeros out.” This is also the expected result as there will be variable pressure as the specimen is lowered and should not run into anything which would cause the motor to stop rotating.

The images in figures 5.6 and 5.7 show 4 consecutive panels in which the nylon string is clearly visible crossing through the 2nd, 3rd, and 4th column of images. This shows a feasibility of concept that the APPS is able to successfully raise and lower a tissue sample accurately and precisely into the same spot. The resulting precision is important to ensure that the area chosen by the user remains in the frame of image acquisition. However, the experiment began with the objective of completing a full ten paneled imaging session. A full ten panel image acquisition was completed successfully, however the resulting image quality was not optimal. The lack of optimal images was not because of the APPS necessarily, but the integration between the APPS and the ability of the system to focus on the tissue. The imaging system uses a LabVIEW VI to complete autofocused imaging. The autofocus functions capturing and resolving an initial image, considered the figure-of-merit. The microscope objective is then raised and lowered a certain distance in the z axis set by the user and takes an image at each height. An algorithm then compares the two images taken after the initial image to see which one has the better figure-of-merit. The algorithm will then decide on an image and either raise in the z direction to get closer to optimal focus or determine that the focus is satisfactory, and the imaging process begins.

It is possible that this method is causing issues of focus as panels slowly become increasingly out of focus as the imaging process continues. An explanation of this phenomenon is that when the imaging process begins, the specimen which is being imaged is focused manually by the operator. Once the process begins, the operator does not touch the system again and the system focuses itself between panels. The problem likely occurs in between panels, when the autofocus algorithm is comparing a part of the tissue which was originally in focus when it was adjusted manually to a different distance to the last z position of the objective. If the last position of the objective is very far away, the algorithm may not be able to correctly focus and will begin functioning outside the working distance of the objective, the distance which the objective is able to resolve an object. This process is shown in figure 5.8. To fix this problem would just mean that an optimization of the Autofocus feature in conjunction with the APPS needs to be done since each system “works” independently.

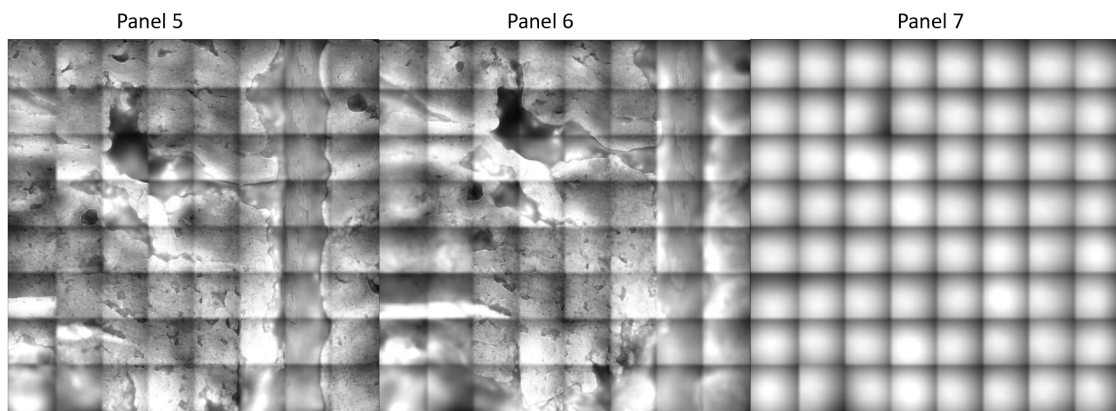


Figure 5.8: The process by which the autofocus causes the microscope objective to travel outside of its working distance.

6. Conclusion

There are 191,930 estimated cases of prostate cancer expected in 2020, 33,330 of which are expected to be fatal boasting a mortality rate of 17.36% [1]. To put it more simply, 1 in 41 men will die of prostate cancer. 33,330 deaths this year means that prostate cancer is the second leading cause of death for men in the US only behind lung cancer. It is estimated that 1 in 9 men will develop prostate cancer in their lifetime, with 66 being the average age of diagnosis and 6 in ten men above the age of 65 are diagnosed with prostate cancer. There are a vast number of treatment and therapy options for patients diagnosed with prostate cancer, but a common procedure for patients with prostate cancer that is believed to not have metastasized is the radical prostatectomy [5]. A radical prostatectomy involves the surgical removal of the full prostate as well as possible adjacent tissue in order to contain the tumors within the gland, typically completed through robotic assistance for laparoscopic surgeries [5]. The method for determining the success of this procedure is an analysis of the margin of the excised tissue, known as a surgical margin analysis. These analyses have a qualifying value which determines them either positive or negative. A positive margin means there are tumor cells present at the surface of the surgical margin. A negative margin means that tumor cells are not present at the surface of the surgical margin implying that the tumor cells are contained within the excised tissue and the surgical procedure was a success.

A positive surgical margin (PSM) is considered an adverse prognostic factor regardless of the stage and is associated with an increased risk of biochemical recurrence as well as local disease recurrence. It is estimated that 11-38% of radical prostatectomies

report a PSM. The current gold standard of margin analysis is formalin fixed paraffin embedded (FFPE) histology. The resected specimen is sectioned into 4 μm thick slices and stained with Hematoxylin and Eosin for analysis under a microscope objective. This process works well, however it requires several days of post-operative analysis and can still report false negative margins. The need for a secondary procedure should the FFPE analysis come back positive is expensive for hospitals as well as patients and can lead to further reduced quality of life for patients. The solution for solving this problem would be an intraoperative method that can analyze surgical margins before the procedure is finished so the surgeon can continue to remove tissue as needed.

The only current intra-operative method of surgical margin analysis is known as Frozen Section Analysis (FSA). The current procedure used for targeted FSA is known as neurovascular structure-adjacent frozen-section examination (NeuroSAFE), which aims to spare nervous structures around the prostate to improve post-operative quality-of-life [9]. After the tissue is resected, the margin nearest to the tumor of the tissue is inked to maintain anatomical orientation of the tissue and then a large section removes the entire margin. This section is serially sectioned further into 3-4 mm slices and then frozen with liquid CO_2 . After freezing, the smaller sections are once again cut into smaller sections with 3-4 micron thickness and are stained with hematoxylin and eosin for pathological review [10]. The limitations of targeted FSA are caused by the necessary time and labor involved in the process which makes it difficult to analyze a large portion of the prostate. Other limitations include poor sampling and difficulty cutting the frozen tissue, tissue damage from frozen artifacts, and a lack of sufficient comparable data to compare suspicious findings with due to the relatively new nature of frozen section analysis [10,11].

A new approach to surgical margin analysis changes the focus of histological image acquisitions from a microscope slide to the resected tissue itself, either in whole or a larger section, known as *Ex Vivo* microscopy. *Ex Vivo* microscopy uses advanced cutting techniques in order to eliminate the time and labor intensive cutting steps required for FSA. The current techniques used for intraoperative margin analysis and PSM correction include depth-sensitive techniques known as optical coherence tomography and photoacoustic tomography, and optical sectioning techniques such as reflectance and fluorescence scanning confocal microscopy and label-free nonlinear microscopies [13-23].

Each of these techniques are promising for the imaging of small specimens, ranging from skin cancer resections, core needle biopsies, and gross pathology sections of larger resected specimens. Despite this, research has not yet been able to provide sub-cellular resolution images of fully intact tumor resection surfaces.

Our group has developed a microscope which is capable of video-rate (33 frames per second) SIM, VR SIM, at 2048x2048 pixels per frame, corresponding to an image pixel sampling rate of 134.8 million pixels per second. Our group has previously completed a validation study of VR-SIM using large core prostate biopsies compared to gold-standard H&E, where the diagnostic accuracy on pathologist review resulted in an area under the ROC curve of 0.82-0.88, even in the presence of limited prostate adenocarcinoma content (average 13.7% tumor content per malignant biopsy) [39]. This method was taken further by Wang et al., 2016, implementing the VR-SIM system in order to complete full gigapixel surface imaging of radical prostatectomy specimens to analyze surgical margins for the presence of tumors. The process of this involved placing a wooden dowel through the urethral lumen from apex to base and rotating the prostate manually about the urethra. This

allowed for the full surface imaging of the anterior, posterior, right lateral, and left lateral margins of the resected specimens as shown by figure [32]. Luethy et al. developed a semi-automated device which took the whole-organ *ex vivo* imaging process further by treating the prostate specimen as a deforming sphere [40]. By calculating the deformation using an equation (equation 1) for the surface area of a compressed sphere, it was found that it was most optimal to treat the surface of the prostate as a decagon to achieve maximum surface coverage. This semi-automated machine, named the Automated Prostate Positioning System (APPS) utilized two stepper motors in order to manipulate the excised prostate specimen, rotating the specimen 36° degrees about its urethral axis in order to increase surface coverage for gigapixel surface imaging.

The APPS Generation 1 worked well in the research environment; however, its end goal of point-of-care clinical use was not attainable in its current configuration. This work found the challenges posed by the past design which were limiting its ability to be used in a clinical setting. These challenges were then used to inspire a new set of functional requirements for the design of the APPS, one which boasted full automation to complete the objective of single-operator automation, could complete these actions accurately, and could complete these actions repeatedly. Several sensors were experimentally tested in order to find a method in which the APPS would be able to control its own motion without requiring more than a single user input. Eventually, a servo motor was used in order to monitor the changing draw of voltage which the servo motor requires in order to operate.

The APPS Generation 2 was then validated through bench experiments. The three bench experiments run provided information about how the new configuration of the APPS compared to its predecessor. The comparison of these two devices was somewhat difficult

considering the change in the imaging protocol of the lab, however when comparing the speed of the two devices the fully automated APPS is theoretically shown to be twice as fast. The second experiment was able to show the new APPS is capable of completing its operations accurately and repeatedly, barring a minor design flaw. The third experiment served to provide proof of concept that the APPS would be capable of producing accurate ten panel image acquisitions.

The emergence of the global pandemic of COVID19 influenced the progression of this work and required a large amount of flexibility. Several aspects of this work were unable to be completed due to issues with timing, social distancing, and public safety. The new configuration of the APPS was not able to be tested using a true prostatectomy specimen. This is because it was no longer possible to consent patients for the use of the excised tissue from their procedure. Thus, it was not possible for our group to continue this clinical study during this time.

Future work of the APPS would include several design changes. The first being a design change which aims to solve the issue detailed in experiment 2. A second design change would be a change to the dowel rod system currently employed within our protocol. As of now, wooden dowel rods are cut separately in order to fit within the system. A new wooden dowel is required each time the system is used which is neither practical nor sustainable. A possible solution for this issue would be to use a 3D printed or metal dowel, however there are drawbacks to both ideas. Finally, in order for the APPS to take further steps towards becoming a clinically viable method of point-of-care intraoperative margin analysis, it must be more centrally contained. As of now, the APPS has 4 separate pieces: the servo tower, the housing for stepper motor 2, the Arduino which it is connected to, and

the breadboard which contains the voltage feedback circuit. The consolidation of these pieces to just the tower, stepper motor 2 housing, and a central microcontroller voltage feedback setup would greatly increase the mobility and versatility of the APPS. In conclusion, the problems posed by the previous design for a possible method of intra-operative margin analysis were addressed in order to innovate and improve upon this design.

7. Bibliography

1. Siegel, R. L., Miller, K. D., & Jemal, A. (2020, January 8). Cancer statistics, 2020. Retrieved from <https://acsjournals.onlinelibrary.wiley.com/doi/full/10.3322/caac.21590>
2. Mortality in the United States, 2018. (n.d.). Retrieved from <https://www.cdc.gov/nchs/data/databriefs/db355-h.pdf>
3. NCI Dictionary of Cancer Terms. (n.d.). Retrieved from <https://www.cancer.gov/publications/dictionaries/cancer-terms/def/cancer>
4. Key Statistics for Prostate Cancer: Prostate Cancer Facts. (n.d.). Retrieved from <https://www.cancer.org/cancer/prostate-cancer/about/key-statistics.html>
5. Surgery for Prostate Cancer. (n.d.). Retrieved from <https://www.cancer.org/cancer/prostate-cancer/treating/surgery.html>
6. Surgical Margins. (2018, September 19). Retrieved from <https://www.breastcancer.org/symptoms/diagnosis/margins>
7. Kynaston, H., Parker, C. C., & Sydes, M. R. (2009). Re: Ofer Yossepowitch, Anders Bjartell, James A. Eastham, et al. Positive Surgical Margins in Radical Prostatectomy: Outlining the Problem and Its Long-Term Consequences. *Eur Urol* 2009;55:87–99. *European Urology*, 55(6). doi: 10.1016/j.eururo.2009.03.022
8. Wieder, J. A., & Soloway, M. S. (1998). Incidence, Etiology, Location, Prevention And Treatment Of Positive Surgical Margins After Radical Prostatectomy For Prostate Cancer. *The Journal of Urology*, 299–315. doi: 10.1097/00005392-199808000-00003
9. Mirmilstein, G., Rai, B. P., Gbolahan, O., Srirangam, V., Narula, A., Agarwal, S., ... Adshead, J. (2017). The neurovascular structure-adjacent frozen-section examination (NeuroSAFE) approach to nerve sparing in robot-assisted laparoscopic radical prostatectomy in a British setting - a prospective observational comparative study. *BJU International*, 121(6), 854–862. doi: 10.1111/bju.14078
10. Vasdev, N., Agarwal, S., Rai, B. P., Soosainathan, A., Shaw, G., Chang, S., ... Adshead, J. M. (2015). Intraoperative Frozen Section of the Prostate Reduces the Risk of Positive Margin Whilst Ensuring Nerve Sparing in Patients with Intermediate and High-Risk Prostate Cancer Undergoing Robotic Radical Prostatectomy: First Reported UK Series. *Current Urology*, 9(2), 93–103. doi: 10.1159/000442860
11. Jaafar H. Intra-operative frozen section consultation: concepts, applications and limitations. *Malays J Med Sci*. 2006;13(1):4–12.
12. Tsuboi, T., Ohori, M., Kuroiwa, K., Reuter, V. E., Kattan, M. W., Eastham, J. A., & Scardino, P. T. (2005). Is intraoperative frozen section analysis an efficient way to reduce positive surgical margins? *Urology*, 66(6), 1287–1291. doi: 10.1016/j.urology.2005.06.073

13. Dobbs, J. L., Ding, H., Benveniste, A. P., Kuerer, H. M., Krishnamurthy, S., Yang, W., & Richards-Kortum, R. (2013). Feasibility of confocal fluorescence microscopy for real-time evaluation of neoplasia in fresh human breast tissue. *Journal of Biomedical Optics*, 18(10), 106016. doi: 10.1117/1.jbo.18.10.106016
14. Saldua MA, Olsovsky CA, Callaway ES, Chapkin RS, Maitland KC. Imaging inflammation in mouse colon using a rapid stage-scanning confocal fluorescence microscope. *J Biomed Opt*. 2012;17(1):016006. doi:10.1117/1.JBO.17.1.016006
15. Tao YK, Shen D, Sheikine Y, et al. Assessment of breast pathologies using nonlinear microscopy. *Proc Natl Acad Sci U S A*. 2014;111(43):15304–15309. doi:10.1073/pnas.1416955111
16. Tewari AK, Shevchuk MM, Sterling J, et al. Multiphoton microscopy for structure identification in human prostate and periprostatic tissue: implications in prostate cancer surgery. *BJU Int*. 2011;108(9):1421–1429. doi:10.1111/j.1464-410X.2011.10169.x
17. Chen, C.-S., Elias, M., Busam, K., Rajadhyaksha, M., & Marghoob, A. (2005). Multimodal in vivo optical imaging, including confocal microscopy, facilitates presurgical margin mapping for clinically complex lentigo maligna melanoma. *British Journal of Dermatology*, 153(5), 1031–1036. doi: 10.1111/j.1365-2133.2005.06831.x
18. Abeytunge S, Li Y, Larson B, Toledo-Crow R, Rajadhyaksha M. Rapid confocal imaging of large areas of excised tissue with strip mosaicing. *J Biomed Opt*. 2011;16(5):050504. doi:10.1117/1.3582335
19. Bini J, Spain J, Nehal K, Hazelwood V, DiMarzio C, Rajadhyaksha M. Confocal mosaicing microscopy of human skin ex vivo: spectral analysis for digital staining to simulate histology-like appearance. *J Biomed Opt*. 2011;16(7):076008. doi:10.1117/1.3596742
20. Abeytunge S, Li Y, Larson B, Toledo-Crow R, Rajadhyaksha M. Rapid confocal imaging of large areas of excised tissue with strip mosaicing. *J Biomed Opt*. 2011;16(5):050504. doi:10.1117/1.3582335
21. Karen JK, Gareau DS, Dusza SW, Tudisco M, Rajadhyaksha M, Nehal KS. Detection of basal cell carcinomas in Mohs excisions with fluorescence confocal mosaicing microscopy. *Br J Dermatol*. 2009;160(6):1242–1250. doi:10.1111/j.1365-2133.2009.09141.x
22. Gareau DS, Li Y, Huang B, Eastman Z, Nehal KS, Rajadhyaksha M. Confocal mosaicing microscopy in Mohs skin excisions: feasibility of rapid surgical pathology. *J Biomed Opt*. 2008;13(5):054001. doi:10.1117/1.2981828
23. Scope A, Mahmood U, Gareau DS, et al. In vivo reflectance confocal microscopy of shave biopsy wounds: feasibility of intraoperative mapping of cancer margins. *Br J Dermatol*. 2010;163(6):1218–1228. doi:10.1111/j.1365-2133.2010.10063.x
24. Handbook of Biomedical Optics

25. Auksorius, E. et al. Dual-modality fluorescence and full-field optical coherence microscopy for biomedical imaging applications. *Biomed Opt Express* 3, 661–666 (2012).
26. Dangle, P. P., Shah, K. K., Kaffenberger, B. & Patel, V. R. The use of high resolution optical coherence tomography to evaluate robotic radical prostatectomy specimens. *International braz j urol:official journal of the Brazilian Society of Urology* 35, 344–353 (2009).
27. Nguyen, F. T. et al. Intraoperative evaluation of breast tumor margins with optical coherence tomography. *Cancer Res* 69, 8790–8796 (2009).
28. Kut, C. et al. Detection of human brain cancer infiltration ex vivo and in vivo using quantitative optical coherence tomography. *Science translational medicine* 7, 292ra100 (2015).
29. Introduction to OCT. (n.d.). Retrieved from <http://obel.ee.uwa.edu.au/research/fundamentals/introduction-oct/>
30. Parallax Feedback 360 Servo User Guide
31. Wang, Mei, Tulman, David B., Sholl, Andrew B., Kimbrell, Hillary Z., Mandava, Sree H., Elfer, Katherine N., Luethy, Samuel, Maddox, Michael M., Lai, Weil, Lee, Benjamin R., Brown, J. Quincy. Gigapixel surface imaging of radical prostatectomy specimens for comprehensive detection of cancer-positive surgical margins using structured illumination microscopy. *Scientific Reports*. (2016).
32. Gareau D, Bar A, Snavely N, Lee K, Chen N, Swanson N, et al. Tri-modal confocal mosaics detect residual invasive squamous cell carcinoma in Mohs surgical excisions. *J Biomed Opt.* 2012;17(6):066018.
33. Ragazzi, M., Piana, S., Longo, C., Castagnetti, F., Foroni, M., Ferrari, G., ... Pellacani, G. (2013). Fluorescence confocal microscopy for pathologists. *Modern Pathology*, 27(3), 460–471. doi: 10.1038/modpathol.2013.158
34. Thomas, B., Momany, M., & Kner, P. (2013). Optical sectioning structured illumination microscopy with enhanced sensitivity. *Journal of Optics*, 15(9), 094004. doi: 10.1088/2040-8978/15/9/094004
35. Neil, M. A. A., Juškaitis, R., & Wilson, T. (1997). Method of obtaining optical sectioning by using structured light in a conventional microscope. *Optics Letters*, 22(24), 1905. doi: 10.1364/ol.22.001905
36. Schlichenmeyer, T. C., Wang, M., Elfer, K. N. & Brown, J. Q. Video-rate structured illumination microscopy for high-throughput imaging of large tissue areas. *Biomed Optics Express* 5, 366–377 (2014).
37. Wang, M. et al.. *Cancer Res* 75, 4032–4041 (2015)
38. Luethy, S. J. (2018). Automated Handling Device for Circumferential Gigapixel Microscopy of Whole Prostate Resections. *Biophotonics Congress: Biomedical Optics Congress 2018 (Microscopy/Translational/Brain/OTS)*. doi: 10.1364/translational.2018.jw3a.3

39. Luethy, S. J. (2018). New Methods of Whole-Organ Ex Vivo Surface Imaging of the Prostate (Master's Thesis). Available from ProQuest Dissertations & Theses Global database. (No. 10791655)
40. Thomas, G., Nguyen, T., Pence, I.J. *et al.* Evaluating feasibility of an automated 3-dimensional scanner using Raman spectroscopy for intraoperative breast margin assessment. *Sci Rep* **7**, 13548 (2017). <https://doi.org/10.1038/s41598-017-13237-y>
41. Glaser, A. K., Reder, N. P., Chen, Y., McCarty, E. F., Yin, C., Wei, L., Wang, Y., True, L. D., & Liu, J. (2017). Light-sheet microscopy for slide-free non-destructive pathology of large clinical specimens. *Nature biomedical engineering*, *1*(7), 0084. <https://doi.org/10.1038/s41551-017-0084>

8. Appendix

Arduino Code

APPS Generation 1 Operating Code:

```
#include <Stepper.h>
#define StepsPerRev 32
#define LEVER_SWITCH_PIN 6

int ledPIN = 2;

Stepper StepMotor_Spin(StepsPerRev, 8, 10, 9, 11);

//int num_steps_Spin; // declares variables
int num_steps_Lift;
int num_steps_Down;
int num_steps_Spin;

int button_Go = 7;
int button_Up = 12;
int button_Down = 13;
int button_Spin = 5;
const int wakeUpPinGo = 7;
int pressSwitch;
int press_Up;
int press_Down;
int press_Spin;

//includes libraries
#include <Wire.h>
```

```
#include <Adafruit_MotorShield.h>
#include "utility/Adafruit_MS_PWMServoDriver.h"

// Create the motor shield object with the default I2C address
Adafruit_MotorShield AFMS = Adafruit_MotorShield();
// Or, create it with a different I2C address (say for stacking)
// Adafruit_MotorShield AFMS = Adafruit_MotorShield(0x61);

// Connect a stepper motor with 200 steps per revolution (1.8 degree)
// to motor port #2 (M3 and M4)
Adafruit_StepperMotor *myMotor = AFMS.getStepper(200, 2); //steps per rev, port
number

//-----

void setup(){
  pinMode(ledPIN, OUTPUT);
  pinMode (button_Go, INPUT_PULLUP);
  pinMode (button_Up, INPUT_PULLUP);
  pinMode (button_Down, INPUT_PULLUP);
  pinMode (button_Spin, INPUT_PULLUP);
  pinMode (wakeUpPinGo, INPUT_PULLUP);
  pinMode(LEVER_SWITCH_PIN,INPUT_PULLUP);

  //AFMS.begin(); // create with the default frequency 1.6KHz
  AFMS.begin(2000); // OR with a different frequency, say 1KHz

  myMotor->setSpeed(200);
```

```
}

//-----

void loop(){
  int button_Go_State = digitalRead(button_Go);
  int button_Up_State = digitalRead(button_Up);
  int button_Down_State = digitalRead(button_Down);
  int button_Spin_State = digitalRead(button_Spin);

  if (button_Go_State == 0){
    for(int s=0; s<5; s++){ //10 spins * 36 degrees per spin = 360 degrees
      Go();
    }
  }

  if (button_Up_State == 0){
    Up();
  }

  if (button_Down_State == 0){
    Down();
  }

  if (button_Spin_State == 0){
    Spin();
  }
}
```

```
//-----  
void wakeUp(){  
}  
  
void Go(){  
  while (pressSwitch == LOW){  
    myMotor->step(1, FORWARD, DOUBLE);  
    int pressSwitch = digitalRead(LEVER_SWITCH_PIN);  
    if (pressSwitch == HIGH){  
      break;  
    }  
  }  
}  
  
digitalWrite(2, HIGH);  
delay(5000); // time required to image  
digitalWrite(2, LOW);  
  
myMotor->step(1000, BACKWARD, DOUBLE);  
  
num_steps_Spin = 102; //18 degrees or 204 steps for 36 degrees  
StepMotor_Spin.setSpeed(600);  
StepMotor_Spin.step(num_steps_Spin);  
}  
  
void Up(){  
  while (press_Up == LOW){  
    myMotor->step(1, BACKWARD, DOUBLE);
```

```
int press_Up = digitalRead(button_Up);
if (press_Up == HIGH){
    break;
}
}
}

void Down(){
    while (press_Down == LOW){
        myMotor->step(1, FORWARD, DOUBLE);
        int press_Down = digitalRead(button_Down);
        if (press_Down == HIGH){
            break;
        }
    }
}

void Spin(){
    num_steps_Spin = 204; //36 degrees
    StepMotor_Spin.setSpeed(600);
    StepMotor_Spin.step(num_steps_Spin);

}
```

Version 1:

```
myServo.attach(9); // attaches Servo to pin 9
```

```

digitalWrite(4,LOW); // Pin 4 reads 3.3 V
while (myServo.attached()){
  int val = {analogRead(batteryPin)}; //reading from analog 0
  float volts = (val / 1023.0)*referenceVolts; // Translates serial information into voltages
  Serial.println(volts); // Serial monitor reads in values produced by ground wire of servo
  if (volts == 0){
    myServo.writeMicroseconds(1600); // Servo rotates clockwise "raising" the dowel
    Serial.println(volts);
  }
  else if(volts>=0.07){
    Serial.println(volts);
    myServo.detach(); // Servo detaches and stops moving
    digitalWrite(4,HIGH); // Pin 4 outputs 5V signal
    int finish = digitalRead(4); // Arduino reads Pin 4
    if (finish == HIGH) {
      Serial.println("Rotate!");
    }
  }
}

delay(1000);

int pause = digitalRead(7); // initializes pause function
if (pause == HIGH) { //
  digitalWrite(6,HIGH); // Turn PIN HIGH as logical signal
  int turn = digitalRead(6); // Reads PIN HIGH completing IF statement
  if (turn == HIGH) {
    StepMotor_Spin.setSpeed(600);
    StepMotor_Spin.step(num_steps_Spin); // Turn 204 steps for 36 degrees
  }
}

```

```
    digitalWrite(6,LOW); // Set PIN 6 back to LOW for loop
  }
  digitalWrite(7,LOW);
}

myServo.attach(9);
digitalWrite(5,LOW);
while (myServo.attached()){
  int val = {analogRead(batteryPin)}; //reading from analog 0
  float volts = (val / 1023.0)*referenceVolts;
  Serial.println(volts);
  if ((volts == 0) || (volts > 0.12)){ // If volts are equal to 0 or volts are greater than 0.12
    myServo.writeMicroseconds(1400); // turns counterclockwise
    Serial.println(volts);
  }
  else if((volts >= 0.08) && (volts <= 0.12)){
    Serial.println(volts);
    myServo.detach();
    digitalWrite(5,HIGH);
    int finish = digitalRead(5);
    if (finish == HIGH) {
      Serial.println("Image!");
    }
  }
}
delay(5000);
}
```

Version 2:

```
#include <Stepper.h>
#include <Servo.h>
#define StepsPerRev 32
Servo myServo;
Stepper StepMotor_Spin(StepsPerRev, 8, 10, 9, 11);
int num_steps_Spin = 204; //36 degrees
const int batteryPin=0; // initialize A0
const float referenceVolts=6; //starting reference volts
void setup() {
    // put your setup code here, to run once:
    myServo.attach(9);
    Serial.begin(9600);
    pinMode(6,OUTPUT);
    pinMode(7,OUTPUT);
    pinMode(5,OUTPUT);
    pinMode(4,OUTPUT);
}

void loop() {
    // put your main code here, to run repeatedly:
    delay(1000);

    myServo.attach(9);

    digitalWrite(4,LOW);
    while (myServo.attached()){
```

```
int val = {analogRead(batteryPin)}; //reading from analog 0
float volts = (val / 1023.0)*referenceVolts;
Serial.println(volts);
if (volts == 0){
  myServo.writeMicroseconds(1600);
  Serial.println(volts);
}
else if(volts>=0.07){
  Serial.println(volts);
  myServo.detach();
  digitalWrite(4,HIGH);
  int finish = digitalRead(4);
  if (finish == HIGH) {
    Serial.println("Rotate!");
  }
}
}

delay(1000);
int pause = digitalRead(7);
if (pause == HIGH) { //
  digitalWrite(6,HIGH); // Turn PIN HIGH as logical signal
  int turn = digitalRead(6); // Reads PIN HIGH completing IF statement
  if (turn == HIGH) {
    StepMotor_Spin.setSpeed(600);
    StepMotor_Spin.step(num_steps_Spin); // Turn 204 steps for 36 degrees
    digitalWrite(6,LOW); // Set PIN 6 back to LOW for loop
  }
}
```

```
digitalWrite(7,LOW);
}

myServo.attach(9);
digitalWrite(5,LOW);
while (myServo.attached()){
  int val = {analogRead(batteryPin)}; //reading from analog 0
  float volts = (val / 1023.0)*referenceVolts;
  Serial.println(volts);
  if ((volts == 0) || (volts > 0.12)){
    myServo.writeMicroseconds(1400);
    Serial.println(volts);
  }
  else if((volts>=0.08) && (volts <= 0.12)){
    Serial.println(volts);
    myServo.detach();
    digitalWrite(5,HIGH);
    int finish = digitalRead(5);
    if (finish == HIGH) {
      Serial.println("Image!");
    }
  }
}
delay(5000);
}
```

MATLAB Code:

Version 1:

```

clear all;
a = arduino();      % Establishes connection and libraries to arduino, this is done during
                    % setup initially
shield = addon(a, 'Adafruit\MotorShieldV2');    % Creates shield object
clear s;           % Ensures Nothing is left in S variable during repetitive imaging cycles
% for i = 1:10
    s = servo(a, 'D9', 'MinPulseDuration', 700*10^-6, 'MaxPulseDuration', 2300*10^-6);
    % established servo obj (arduino, pin#, min max pulse width)
    for angle = 0.6:0.01:1      % controls "angle" above 0.5 is CW rotation, under 0.5 is
                                % CCW rotation
        writePosition(s, angle); % Rotates servo through angle counter above
        spin_speed = readPosition(s);
        fprintf('Current motor position is %d degrees\n', spin_speed);
        pause(2);
        voltage = readVoltage(a, 'A0'); % Reads trace electricity caused by stalling of servo
        % at pin A0
        fprintf('Voltage is %d Volts\n', voltage); % Tells voltage reading
        if voltage < 1e02      % This is the threshold for stopping motion
            break
        end
    end
clear s;
clear angle;

sm = stepper(shield, 2, 200); % creates stepper object
sm.RPM = 100;                % sets stepper rotation speed (rotations per minute)
move(sm, 204);               % tells stepper to turn 204 steps (36 degrees)

clear sm shield;
                                % process repeats from here but in the
                                % opposite direction
s = servo(a, 'D9', 'MinPulseDuration', 700*10^-6, 'MaxPulseDuration', 2300*10^-6);
for angle = 0:0.01:0.4
    writePosition(s, angle);
    spin_speed = readPosition(s);
    fprintf('Current motor position is %d degrees\n', spin_speed);
    pause(2);
    voltage = readVoltage(a, 'A0');
    fprintf('Voltage is %d Volts\n', voltage);
    if voltage < 1e-02
        break
    end
end
clear s;
clear angle;
% end

```

```
clear a s sm shield;
```

Version 2:

Servo Raise Rotate:

```
clear all;
a = arduino();
shield = addon(a, 'Adafruit\MotorShieldV2'); % Establishes connection and libraries
to arduino, this is done during setup initially
clear s; % clears servo object when restarting

count = 0; % empty variable to begin sample counts
v=[]; % Empty array to store voltage readings
s = servo(a, 'D9', 'MinPulseDuration', 700*10^-6, 'MaxPulseDuration', 2300*10^-6); %
Controls servo Pulse Width Modulation, attaches servo object
tic %Begins internal timer for measuring time of execution of for loop
for angle = 0.6:0.001:1 % Controls the direction turning >0.5 is CW
    writePosition(s, angle); % Turns Servo motor through desired for loop
    pause(0.01); % 0.01 s pause to take voltage readings
    voltage = readVoltage(a,'A0'); % Reads voltage from Analog Pin 0 on arduino
    fprintf('Voltage is %d Volts\n', voltage); % Prints voltages
    count = count + 1; % Sample counter
    v(count) = mean(voltage);
    sample = (1:1:count); % Creates array of total counts

    if voltage >= 3e-01 || voltage==0 % Threshold condition for exceeding 0.3 V or
reading 0V
        break
    end
end
time(count) = toc; % Stops timer after threshold condition is met

sm = stepper(shield, 2, 200); % Initializes stepper motor (hardware, port, total number
of steps for rotation)
sm.RPM = 100; % Speed in RPM
move(sm, 204); % Rotates stepper 36 degrees

figure
plot(time,v)
title('Voltage vs. Time (s) (Raise)'); % plot title
xlabel = 'Time (s)'; % x-axis label
ylabel = 'Voltage'; % y-axis label
xlabel(xLabel);
ylabel(yLabel);
```

```

figure
plot(sample,v)
title('Voltage vs. Sample (Raise)'); % plot title
xlabel = 'Sample'; % x-axis label
ylabel = 'Voltage'; % y-axis label
xlabel(xLabel);
ylabel(yLabel);

```

```

rmeanv = mean(v);
rmaxv = max(v);
rminv = min(v);
rstdv = std(v);
rsampv = sample;
rtimev = toc;

```

```

datatab = table(rmeanv, rmaxv, rminv, rstdv, rsampv, rtimev) % gives data in table
form

```

```

clear s;
clear angle;
clear sm shield;

```

Servo Lower:

```

clear all;
a = arduino(); % Creates Arduino Object in MATLAB Command Server
shield = addon(a, 'Adafruit\MotorShieldV2'); % Establishes connection and libraries
to arduino, this is done during setup initially
clear s;
s = servo(a, 'D9', 'MinPulseDuration', 700*10^-6, 'MaxPulseDuration', 2300*10^-6); %
Controls servo Pulse Width Modulation, attaches servo object
count = 0; % empty variable to begin sample counts
v=[]; % Empty array to store voltage readings
tic % Begins internal timer for measuring time of execution of for loop
for angle = 0:0.001:0.4 % Controls the direction turning, <0.5 is CCW
    writePosition(s, angle); % Turns Servo motor through desired for loop
    pause(0.01); % 0.01 s pause to take voltage readings
    voltage = readVoltage(a,'A0'); % Reads voltage from Analog Pin 0 on arduino
    fprintf('Voltage is %d Volts\n', voltage); % Prints voltages
    count = count + 1; % Sample counter
    v(count) = mean(voltage);
    sample = (1:1:count); % Creates array of total counts
end

```

```
    if voltage > 3e-01 || voltage == 0 % Threshold condition for exceeding 0.3 V or
reading 0V
        break
    end
end
```

```
end
time(count) = toc; % Stops timer after threshold condition is met, for loop ends
figure
plot(time,v)
title('Voltage vs. Time (s) (Lower)'); % plot title
xlabel = 'Time (s)'; % x-axis label
ylabel = 'Voltage'; % y-axis label
xlabel(xLabel);
ylabel(yLabel);
```

```
figure
plot(sample,v)
title('Voltage vs. Sample (Lower)'); % plot title
xlabel = 'Sample'; % x-axis label
ylabel = 'Voltage'; % y-axis label
xlabel(xLabel);
ylabel(yLabel);
lmeanv = mean(v);
lmaxv = max(v);
lminv = min(v);
lstdv = std(v);
lsampv = sample;
ltimev = toc;
```

```
datatab = table(lmeanv, lmaxv, lminv, lstdv, lsampv, ltimev) % gives data in table form
```

```
clear s a;
clear angle;
```

Biography

Max Cooper was born and raised in Washington, DC. He grew up attending bilingual schools learning Spanish and French, graduating from Woodrow Wilson Senior Highschool before attending Tulane University. Max was an active member of the Tulane Student body serving as a Senator in the Undergraduate Student Government from 2017-2019. Max also served as the Vice President of the Beta Tau chapter of the Zeta Psi Fraternity.